

SOLUTE-DRIVEN MELTING KINETICS IN THE SN-BI SYSTEM

By

DAVID YASENSKY

A THESIS PRESENTED TO THE GRADUATE SCHOOL
OF THE UNIVERSITY OF FLORIDA IN PARTIAL FULFILLMENT
OF THE REQUIREMENTS FOR THE DEGREE OF
MASTER OF SCIENCE

UNIVERSITY OF FLORIDA

2006

Copyright © 2006

By

David Yasensky

ACKNOWLEDGEMENTS

First of all, The NSF is acknowledged for providing the funding for this project. Personally, I would like to thank my family, friends, and colleagues for their continued support during the pursuit of my Masters Degree at UF. To my advisor, Dr. Abbaschian, I extend deep regards for his encouragement and insight. Without his efforts this work would not have been completed. To my co-advisor and committee member Dr. Fuchs I also offer thanks for his technical insight as well as helpful advice concerning the engineering career field. Finally, to my lab partner Joo Ro Kim I offer sincere thanks for constant encouragement, many helpful conversations, and useful advice during the bulk of my experience in graduate school.

TABLE OF CONTENTS

ACKNOWLEDGEMENTS	3
LIST OF TABLES	6
LIST OF FIGURES	7
ABSTRACT	13
CHAPTERS	
1 INTRODUCTION	15
2 LITERATURE REVIEW	17
Introduction.....	17
Diffusion into a Capillary	19
The Diffusion Melting Solution.....	21
Diffusion Melting Without Convection	21
Diffusion Melting with Convection	25
Experimental Analysis	26
Diffusion Coefficients.....	27
Thermodynamics.....	27
Solidification of an Initially 100% Liquid Alloy	31
Melting of an Initially 100% Solid Alloy	34
Reaction between Two Initially Present Phases	35
Solidification as a Reaction between 2 Phases	37
Melting as a Reaction between 2 Phases	38
Melting as a Reaction Between Two Initially Present Phases when Two Opposing Driving39	39
Loss of Equilibrium at the Melting Interface and C_L^{\min}	40
Kinetics	43
The Sn-Bi System	44
3 EXPERIMENTAL APPROACH.....	76
Equipment.....	77
Furnace.....	77
Temperature Monitors	77
Power Source and Controller	78
Data Acquisition	78
Crucible and Sn-Bi Charge Preparation.....	79
Sn Capillary Ingot Preparation.....	80
Procedure	81
Analysis.....	84
Metallography	84

Microscopy	85
SEM	86
EPMA	86
4 RESULTS	93
Sample Labeling Conventions	93
Micrographs	94
SEM Images	95
EPMA	96
Melting Distance vs. Time Data	97
Model Calculations	97
C195-T210	100
C429-T210	101
C429-T175	102
Kinetic Relationships	102
Change in A with Driving Force	103
Change in A with Temperature	105
Error	105
Temperature Fluctuations	106
Change in Melt Composition	106
Latent Heat of Melting	107
5 DISCUSSION	145
Micrographs and SEM Analysis	145
Diffusion Control	145
EPMA Data	147
Deviations from Equilibrium	148
Combined Statement for the Effects of Temperature and Supersaturation	150
Future Work	151
6 CONCLUSIONS	154
REFERENCES	156
BIOGRAPHICAL SKETCH	158

LIST OF TABLES

<u>Table</u>		<u>Page</u>
1	Properties of Sn, Bi, and the Sn-Bi System	75
2	Melting Distances at 210°C and 19.5 at% Bi (C195-T210).....	130
3	Melting Distances at 210°C and 42.9 at% Bi (C429-T210).....	131
4	Melting Distances at 175°C and 42.9 at% Bi (C429-T175).....	132
5	Empirical Kinetic Values for Melting in the Sn-Bi System	139

LIST OF FIGURES

<u>Figure</u>	<u>Page</u>
1	Different paths to melting on the T-X phase diagram. In (a), the phase change is facilitated by a rise in temperature. In (b), the phase change is facilitated by a change in concentration.45
2	Simple 1-D diffusion schematic. The solute flows from high concentration areas to low concentration areas.46
3	Schematic of the experimental concept. The metal-filled capillary is dipped into the solute-rich reservoir. The solute then diffuses into the solid metal via the opening in the tip of the capillary. Since the capillaries are vertical in the lab reference frame, the capillary axis is labeled the z-axis.47
4	1-D diffusion into a capillary with no convection in the reservoir. Position represents the distance from the opening of the capillary; hence, the position $z = 0$ represents the opening of the capillary. Material properties were taken from the Sn-Bi system at 210C.....48
5	1-D diffusion into a capillary with convection in the reservoir. Position represents the distance from the opening of the capillary; hence, the position $z = 0$ represents the opening of the capillary. Material properties were taken from the Sn-Bi system.49
6	1-D diffusion into a capillary with a melting interface and no convection in the reservoir. The left side of the graphs represents the liquid and the right side represents the solid. The vertical line in each profile represents the solid/liquid interface. Material properties were taken from the Sn-Bi system at 210°C. The diffusion constant in the solid was multiplied by 1000 to make the profile visible. The position $z = 0$ represents the opening of the capillary50
7	The predicted values of position and velocity against time for the conditions used to calculate the concentration profiles in Figure 6.....51
8	1-D diffusion into a capillary with a melting interface and convection in the reservoir. The left side of the graphs represents the liquid and the right side represents the solid. The vertical line in each profile represents the solid/liquid interface. Material properties were taken from the Sn-Bi system at 210°C. The diffusion constant in the solid was multiplied by 1000 to make the profile visible. The position $z = 0$ represents the opening of the capillary52
9	The predicted values of position and velocity against time for the conditions used to calculate the concentration profiles in Figure 8.....53

10	G-X diagram exhibiting the two driving forces that arise for the interface values marked.....	54
11	Phase diagram showing the conditions during solidification. At any given temperature during the cooling through the S + L phase field, the concentration at the interface equals the solidus value.....	55
12	Concentration profile during solidification. Solute is rejected from the solid into the liquid causing the build-up at the interface. The initial transient occurs as the alloy passes through the S + L phase field.....	56
13	Concentration profile of the solidified ingot from Figure 12. The depletion in the initial transient equals the enrichment in the final transient.	57
14	G-X diagram showing the determination of equilibrium concentrations by drawing the common tangent. Also, the maximum and minimum concentrations of solid that can be formed from the marked liquid interface concentration are marked. Solid can only form if the tangent to the liquid curve is above the solid curve denoting a negative free energy change upon changing phases. Also, the diagram shows the solid concentration for the largest free energy change.	58
15	Phase diagram showing the initial and final conditions during melting of an alloy.....	59
16	Concentration profile during the melting of an alloy. There is a depletion of solute near the solid interface.	60
17	G-X diagram showing the driving force for melting of an alloy. This can be thought of as the "mirror image" of a G-X diagram showing the driving force for solidification. The driving force for melting is the distance between the tangent to the solid concentration and the liquid curve at the liquid concentration.	61
18	Concentration profile showing the convention for positive and negative flux. Flux is positive when pointing towards the interface.....	62
19	G-X curve showing the graphical representations of chemical potentials and X_1 . The driving forces are determined graphically at X_1 instead of the concentration of the product phase.	63
20	Phase diagram showing the conditions of the initial alloys and the resulting alloy when brought together. The two alloys are the same size and held at a constant temperature.	64
21	Initial concentration profiles for the alloys in Figure 20. The small diffusion barrier in the solid eliminates the driving force for melting (Figure 10). However, the initial concentration of the solid is still assumed to be close to zero.	65

22	G-X diagram showing the driving force for solidification for the conditions presented in Figure 20. More solute passes across the interface than if the initial solid was not present because the depleted solid is a solute sink, and therefore X_I is greater than X_S^* .	66
23	Concentration profile of solidification as a reaction between two phases. The grey regions underneath the profile line equal the grey regions above it at all times.	67
24	Phase diagram showing the initial conditions of two alloys and the final equilibrium conditions when they are placed in contact. The alloys are kept at a constant temperature.	68
25	G-X diagram showing the origin of the driving force for melting with the initial conditions shown in Figure 24. Some solute needed for making the phase change from liquid to solid is supplied by the initially present liquid and therefore not as much solute needs to cross the phase boundary and X_I is less than X_L^* .	69
26	Concentration profile of melting as a reaction between two phases. The grey regions underneath the profile line equal the grey regions above it at all times.	70
27	Phase diagram showing the initial conditions of two alloys and the final equilibrium conditions when they are placed in contact. Both of the initially present alloys are in their respective single phase fields. The alloys are kept at a constant temperature.	71
28	Concentration profile of melting as a reaction between two alloys in their single phase fields. The grey regions underneath the profile line equal the grey regions above it at all times. 1) shows the direction of solute flux due to the concentration gradient in the liquid and 2) shows the direction of solute flux due to the concentration gradient in the solid.	72
29	G-X diagram showing the origin of driving force when two alloys in the single phase fields of liquid and solid are brought together. If diffusion is slow enough in the solid, the interface concentration may be close to its initial value. If this occurs and there is a negligible amount of driving force needed for propagation of the interface, then C_L^{\min} may be recognized in the liquid.	73
30	Sn-Bi T-X phase diagram [24].	74
31	General experimental setup. The crucible sits on a refractory-brick pedestal and is held at a constant temperature by the furnace. The copper sheath helps to spread the heat more evenly across the heated zone. The capillaries enter the crucible vertically via holes drilled in the graphite cap.	88

32	Close-up diagram of the crucible. The Teflon wrapped around the shafts above the cap supports the capillaries. Also, Teflon insulated the Sn in the capillary from the melt until it is removed by the ceramic rod. The thermocouples record the temperature gradient that the melting interface incurs as it moves up the capillary.....	89
33	Crucible and capillary dimensions.....	90
34	Schematic of the tapered capillary tip.....	91
35	Graphite cap schematic and hole layout.	92
36	Sn-Bi phase diagram conditions explored in this study. The concentrations refer to the concentrations of the melt in the reservoir. The concentration of the solid was always pure Sn.....	108
37	C195-T210-10 at 100X. The Sn matrix and the Sn-Bi eutectic are marked. The interface is planer along with most of the other samples.....	109
38	C195-T210-20 at 100X.....	110
39	C195-T210-30 at 100X.....	111
40	C195-T210-40 at 100X.....	112
41	C195-T210-50 at 100X.....	113
42	C429-T175-10 at 100X.....	114
43	C429-T175-20 at 100X.....	115
44	C429-T175-30 at 100X.....	116
45	C429-T175-40 at 100X.....	117
46	C429-T175-50 at 100X.....	118
47	C429-T210-10 at 100X.....	119
48	C429-T210-20 at 100X.....	120
49	C429-T210-50 at 100X.....	121
50	SE image of the melted interface at 200X. Sample was run at 210°C with a reservoir composition of 19.5at% Bi for 40 minutes.....	122

51	BSE image of the melted interface at 200X. Sample was run at 210°C with a reservoir composition of 19.5at% Bi for 40 minutes. The approximate location of the interface is shown with a black dotted line. The red dotted line shows the size and orientation of the line scan taken by the electron probe micro-analyzer. The results of the line scan are shown in Figure 57.	123
52	SE image of the melted interface at 1000X. The image is of the same sample shown in Figure 50.	124
53	BSE image of the melted interface at 1000X. The image is of the same sample shown in Figure 50. The red circles indicate the areas that were chosen for EDX analysis. The spectrum obtained from EDX 1 is shown in Figure 54, and from EDX 2, in Figure 55.	125
54	EDX 1 spectrum (see Figure 53).	126
55	EDX 2 spectrum (see Figure 53).	127
56	EDX analysis of black impurity particle.	128
57	EPMA results from the samples run at 210°C with a reservoir composition of 19.5at% Bi. The y-axis is positioned in the approximate location of the interface. On the chart, “Solid” signifies the area of the sample that had not melted, while “Liquid” signifies the area of the sample that had been liquid during the experiment.	129
58	C195-T210 data and trend-line.	133
59	C429-T210 data and trend-line.	134
60	C429-T175 data and trend-line.	135
61	C195-T210 mean values and error bars.	136
62	C429-T210 mean values and error bars.	137
63	C429-T175 mean values and error bars.	138
64	Linear trend-line for Supersaturation vs. A.	140
65	Non-linear trend-line for supersaturation vs. A.	141
66	Logarithmic plot of A against the reciprocal of absolute temperature for the determination of activation energy.	142

67	"Low Melt" temperature profiles during experiments displaying the temperature near the openings of the capillaries.....	143
68	"High Melt" temperature profiles during experiments displaying the temperature 1cm above the openings of the capillaries.	144
69	Schematic of an experimental setup that uses resistance signals to monitor the location of the melting interface. The setup resembles the one used in this study (Figure 31) with the exception that a current is sent through the sample. The change in resistance as the interface moves can be used to monitor the location and velocity of the interface.....	153

Abstract of Thesis Presented to the Graduate School
of the University of Florida in Partial Fulfillment of the
Requirements for the Degree of Master of Science

SOLUTE-DRIVEN MELTING KINETICS IN THE SN-BI SYSTEM

By

David Yasensky

August, 2006

Chairman: Reza Abbaschian
Major Department: Materials Science and Engineering

The goal of the present study was to gain insight into the mechanisms and behavior of solute driven melting processes. Solute-driven melting refers to melting whose driving force originates from a change in composition, i.e., solute content, rather than a change in temperature. This kind of melting has been known to cause casting defects in superalloys and other metals.

An experimental apparatus was designed and a series of experiments were carried out on Sn-Bi alloys. The apparatus involved diffusing Bi into solid Sn cast inside a glass capillary to cause it to melt. The Bi source was an enriched liquid Sn-Bi alloy contained in a reservoir. The capillary was kept at a constant temperature below its melting point so that the melting was caused by the increasing Bi composition. The progression of the interface was monitored by quenching the process at various times for the same conditions.

The apparatus was successful in delivering data for the displacement of the interface against time. It was found that interface position was approximately proportional to the square root of time, and so the process may be diffusion controlled as conjectured in previous literature. Rough calculations are made relating the temperature and supersaturation to the displacement coefficient A in the equation $z = At^{0.5}$ where z is displacement and t is time. By comparing data at different temperatures with the same supersaturation, an activation energy Q of 60,000J/mol is

calculated. This value is between the activations energies for diffusion of Bi through the liquid and the solid. Suggestions for modification of the apparatus to include *in-situ* interface monitoring are made.

CHAPTER 1 INTRODUCTION

Melting, defined in this paper as a phase change from solid to liquid, is a ubiquitous phenomenon and part of many natural and synthetic processes. From a metallurgical perspective, solidification garners more attention than melting. This is because the microstructure that determines many of the alloy's mechanical and electrical properties forms during solidification. However, recently there have been studies that expose the need for a more fundamental understanding of melting kinetics and mechanisms. For example, it has been shown that melting is the main cause of fragmentation of dendrite arms in alloy castings [1]. Melting also plays an important role in freckle formation in directionally solidified Ni-based superalloys and exudation in continuous castings [2, 3]. Outside of metallurgy, melting is a fundamental part of many geophysical processes. Melting of surrounding rock by magma in underground chambers may affect the composition of deposits from volcanic eruptions [4]. The contamination of the magma presents complications for geophysicists. Large scale melting of ice under the ocean affected by composition and depth (pressure) may affect the global climate [5]. These practical applications along with the desire to further understand this common physical phenomenon have lead to recent interest on melting.

Melting is usually thought of as a thermal process, but it can also be driven by changes in composition or pressure. This paper focuses on melting due to compositional changes, a process termed solutal melting. The thermodynamics have been qualitatively studied by several authors [6-8], and the kinetics have been briefly investigated [9, 10]. However, a complete description of the kinetics of melting is lacking from literature [8].

In the present investigation, a non-intrusive ex-situ technique is used to monitor the progress of a melting interface in the Sn-Bi system. The temperature and pressure are held

virtually constant, so the process is entirely solutally driven (driven by solute). The effects of temperature and composition on the melting velocity are investigated and quantified. Also, the results of the experiments are compared to the prevailing theories on melting kinetics.

CHAPTER 2 LITERATURE REVIEW

Introduction

Melting is the common phenomenon of changing from a solid phase to a liquid phase. As for any change in nature to occur, the Gibbs energy must be lowered for this change to occur spontaneously. Consider the phase diagram in Figure 1. An alloy of composition C at the initial temperature of T_i is heated until the temperature reaches the final temperature T_f . If the temperature is raised slowly and equilibrium prevails, the alloy begins melting when it crosses the solidus line and becomes 100% liquid when it crosses the liquidus line. Similarly, solutal melting is the melting of a substance by changing its composition. The process can be illustrated in on the phase diagram in a way similar to thermal melting. Consider an alloy at temperature T and initial composition C_i . Let us slowly and isothermally add solute to this alloy until the composition reaches its final value, C_f . If the addition of solute is slow enough to allow diffusion to distribute the solute uniformly as it is added, the X marking the equilibrium conditions on the phase diagram will slowly move to the right. As the alloy moves through the solidus line, it begins to melt. After it crosses the liquidus line, all of the solid will have disappeared into liquid. Hence, the solid will have melted not by changing the temperature of the alloy, but by changing its composition.

Now that we have established that changing the composition of an alloy alone can cause melting, let us consider the mechanism for changing the composition of a solid. There are several ways to do this; however in this study the solute is introduced via diffusion or, in cases when a liquid is present, diffusion and convection. These are the most common mechanisms for solutal melting encountered in nature and therefore the most useful to understand. Consider the system in Figure 2. Two solid pieces of metal, M , are brought into contact. One metal has a

concentration C_0 of solute element E. The other is a pure material, with a concentration of zero. When the two touch each other, the difference in concentration forces E atoms to diffuse to the right, and M atoms diffuse to the left. Thus, the concentration of both metals change via diffusion. If the pure alloy is a solid and the saturated alloy has a composition in the liquid region of the phase diagram (thus would thus in almost any case be a liquid), then solutal melting may occur. Also, in this case, convective currents may arise in the liquid and aid mass transfer.

The reaction at the solid/liquid interface must also be considered in this process. Because the properties of this interface are important to many processes, many sophisticated technique for characterizing this interface exist, including deeply penetrating X-rays that deliver structural data [11], *in-situ* TEM [12], and molecular dynamics simulations [13, 14]. However, due to the simple nature of the experimental technique used in this study, the kinetics are more appropriately modeled with the Arrhenius relationship, as Dutta and Rettenmayr [9] and Kang [15] have done using similar techniques.

In the following sections, the thermodynamics of the melting process and the characteristics of the solid-liquid interface will be reviewed, the kinetics of the melting process will be considered, and the results of past investigators of melting will be presented. There will also be a brief summery of the Sn-Bi system, the system used in the present work.

Diffusion

Diffusion is a highly complicated subject about which many volumes have been written. However, for the scope of this project, we will focus on the specific case of diffusion that can be described by Fick's Laws. Other investigators have found that the Sn-Bi system exhibits Fickian diffusion and obeys Darken's Law [16, 17]. The mechanisms for the change in composition that create the driving forces for solutal melting in this study involve diffusion and convection. The

phenomena, as they apply to the present situation, are described below. The diffusion melting solution without convection was first presented by Wan et al. [10], but the modifications due to convection were made by the present author.

Diffusion into a Capillary

For the moment, the effects of gravity and convection are ignored in order to isolate the behavior of the atoms due to diffusion. Consider the simple situation of a capillary and a large reservoir, both filled with liquid metal A. The metal in the capillary is pure, while the metal in the reservoir has a concentration C_{bulk} of solute B. When the capillary is dipped vertically into the reservoir, a concentration gradient arises between the pure metal and the liquid solution.

This creates a driving force for diffusion and solute begins to diffuse upwards into a capillary. If one assumes that mass is transported in one direction (up the capillary), then the concentration profile changes in only one direction. Since this direction is vertical in the laboratory reference frame, it will be dubbed the z -axis. See Figure 3 for a schematic of this situation. The situation can be quantified using Fick's 2nd law [18].

$$\frac{\partial C}{\partial t} = \frac{\partial}{\partial z} \left(D_L \frac{\partial C}{\partial z} \right), \quad (1)$$

where C is the concentration of solute B in A, t is time, D_L is the diffusion coefficient of B in liquid A, and z is the distance. We will use the convention that $z = 0$ at the capillary entrance. Distance into the capillary will be marked with increasing positive numbers and distance into the reservoir will be marked with increasing negative numbers. Since the size of the reservoir and the capillary are both much larger than the size of the zone affected by diffusion, we know that concentration values far from the interface in either part will be unaffected. Therefore, we can define the boundary conditions as

$$C(-\infty, t) = C_{bulk}, \quad (2)$$

and

$$C(\infty, t) = 0. \quad (3)$$

The solution to this equation for the ideal situation is

$$C(z, t) = \left(\frac{C_{bulk}}{2} \right) \left(1 + erf \left(\frac{z}{2\sqrt{D_L t}} \right) \right) \quad (4)$$

Figure 4 shows the concentration profile expected at certain time intervals. The diffusion coefficient for Bi in liquid Sn at 210°C was used for the example calculations. As time progresses, more and more solute diffuses out of the reservoir and into the capillary. Although the reservoir is semi-infinite, the concentration near the capillary opening becomes depleted. Since all mass transfer is assumed to be diffusion-controlled, the solute in the bulk cannot reach the capillary opening fast enough to replace the atoms lost to the metal in the capillary.

Now, simple convection is introduced to the situation. If we assume that the volume of the experimental reservoir is large, convection currents within it will be and unsuppressed. Convection within the capillary is still assumed to be negligible. If we currents in the reservoir are assumed to eliminate concentration gradients more quickly than diffusion, then the concentration near the opening of the capillary will be held at the reservoir's bulk composition. That is, the opening of the capillary will be supplied with enough solute to keep the concentration at approximately the bulk value; however, the capillary is assumed to be small enough to suppress convection currents within it. To model this situation, the boundary condition, (2) is replaced with the equation

$$C(0, t) = C_{bulk}. \quad (5)$$

Solving (1) for the above boundary equations yields the following:

$$C(z,t) = (C_{bulk}) \left(1 + erf \left(\frac{z}{2\sqrt{D_L t}} \right) \right). \quad (6)$$

Figure 4 displays the concentration profiles in the capillary at specified time intervals taking into account equation (5). $C / C_{bulk} = 1$ in the reservoir (negative values on the x-axis). Diffusion into the capillary is faster under these conditions since convection eliminates the depleted area near the capillary entrance. The shapes of the curves are similar to the bottom halves of the curves Figure 5. That is, without convection, the entrance to the capillary is maintained at $0.5C_{bulk}$, but with convection, equation (5) is followed.

The Diffusion Melting Solution

Next, we will attempt to add the solid/liquid interface and change the situation to a melting process. Considering the solid/liquid interface makes the process much more complicated because each phase has its own properties, i.e. density and diffusivity. Partitioning, flux of solute through the interface, and interface concentrations over time must be considered. At this time, the kinetics of the melting process will be ignored; In other words, the interface values for the solid and the liquid will be taken from the phase diagram.

The temperature profile is held constant during melting. Heat is consumed at the interface as the solid melts, however, is it assumed that heat consumed is small compared to the amount of heat in the bulk phases. This is a valid assumption for the present situation in which the area being melted is small. Also, the rate of heat consumption is considered to be slow compared to the thermal diffusivity of the bulk phases.

Diffusion Melting Without Convection

The concentration profiles of the solute in each phase are described by the diffusion equation using the proper diffusivity. The equations for the liquid and solid phases, respectively, are

$$\left. \frac{\partial C}{\partial t} \right|_L = \frac{\partial}{\partial z} \left(D_L \frac{\partial C}{\partial z} \right), \quad (7)$$

and

$$\left. \frac{\partial C}{\partial t} \right|_S = \frac{\partial}{\partial z} \left(D_S \frac{\partial C}{\partial z} \right). \quad (8)$$

D_L and D_S are the diffusivities of solute in the liquid and solid phases. Since solute is conserved, the interface flux equation, (9), applies.

$$(C_L - C_S)v = D_S \left. \frac{\partial C}{\partial z} \right|_S - D_L \left. \frac{\partial C}{\partial z} \right|_L. \quad (9)$$

C_L and C_S are the solid and liquid interface *equilibrium* concentrations, and v the interface velocity. Equations (7) and (8) can be solved when boundary conditions are determined.

We begin with a solute-rich liquid reservoir of concentration C_{bulk} coming into contact with a pure solid. The initial interface between the solid and the liquid will be marked as 0 on the z -axis with the solute-rich liquid reservoir below (negative values) and the pure metal in the capillary above (positive values). At first, convection is ignored and the boundary conditions reflect diffusion controlled mass transfer. In the reservoir, the boundary condition is

$$C(-\infty, t) = C_{bulk}. \quad (10)$$

In the solid, it is

$$C(\infty, t) = C_0. \quad (11)$$

In (11), C_0 is the initial composition of the solid. In this analysis, C_0 is equal to 0 at% solute (100% pure solvent). During the phase change, the migration of the interface affects the

concentration profiles in both phases. Therefore, the concentration profile of each phase depends, to some degree, on the rate of mass transfer on the other. This dependence can be quantified by realizing that *the calculated solid and the liquid concentrations must reach their equilibrium values at the same position z at all times t* . That is,

$$z_{L-I} = z_{S-I} . \quad (12)$$

The subscript “I” denotes “interface”. Since the concentrations reach equilibrium at the interface, the two conditions are interchangeable. A dimensionless term d can be defined as

$$d = \frac{z}{2\sqrt{Dt}} . \quad (13)$$

At the interface position, then, the following assertion can be made about the d values for the different phases:

$$\frac{z_I}{2\sqrt{t}} = d_{L-I}\sqrt{D_L} = d_{S-I}\sqrt{D_S} . \quad (14)$$

d_{L-I} denotes the value of d at the interface for the liquid phase, and so forth. In (14), z_I can be referenced as either the solid or the liquid since $z_{L-I} = z_{S-I}$. The following relationship can be determined from (9) or by taking the derivative of (14) with respect to time:

$$v = \frac{dz_I}{dt} = d_{L-I}\sqrt{\frac{D_L}{t}} = d_{S-I}\sqrt{\frac{D_S}{t}} . \quad (15)$$

Solving for C in the liquid, we obtain

$$C(z,t)|_L = C_{bulk} + (C_L - C_{bulk})\frac{1 + erf(d_L)}{1 + erf(d_{L-I})} . \quad (16)$$

Solving for the solid we obtain a similar result,

$$C(z,t)|_S = C_0 + (C_S - C_0)\frac{1 - erf(d_S)}{1 - erf(d_{S-I})} . \quad (17)$$

It is clarified that in (14) and (15), d_{L-I} and d_{S-I} are constants. They are specific values of d_L and d_S , which are variables that change with z and t in accordance with (13). In order to determine the values of d_{L-I} and d_{S-I} , we can plug (16) and (17) into the interface equation, (9). The result is equation (18). If both of the diffusion coefficients are known, we can use (14) to write the expression in terms of either d_{L-I} or d_{S-I} , and then determine the other from, again, (14). Due to the nature of the resulting expression, the interfacial d -values must be solved for analytically.

$$\sqrt{\pi} = \frac{C_{bulk} - C_L}{C_L - C_S} \frac{e^{-d_{L-I}^2}}{d_{L-I}(1 + erf(d_{L-I}))} + \frac{C_0 - C_S}{C_L - C_S} \frac{e^{-d_{S-I}^2}}{d_{S-I}(1 - erf(d_{S-I}))}. \quad (18)$$

When plotting (16) and (17), the z domain for each is limited to one side of z_I , which corresponds physically to the presence of either liquid or solid along z . The concentration profiles of the solid and liquid can be “attached” to one another at z_I . The values of the phases at z_I are their respective equilibrium values. Since (14) is incorporated in the formulation, the equilibrium values for the solid and the liquid should correspond to the same z value at all times t , which allows the interface to be easily identified graphically.

Figure 6 shows the results of this treatment using values from the present study. The physical values used to calculate the figure are samples from the present study except for the diffusion constant in the solid. The diffusion coefficient in the solid was taken from the study by Verhoeven [17]. The temperature of the process was placed at 210°C. The bulk concentration was taken as 0.195 mole fraction Bi, the liquid diffusion coefficient was taken as $1.765 \times 10^{-5} \text{ cm}^2\text{s}^{-1}$, and the equilibrium concentrations were taken from the phase diagram. The vertical dashed line represents the initial phase interface before remelting occurs. The diffusion constant in the solid was taken as 1,000 times the true diffusion coefficient so that the concentration profile in the solid would be visible.

Using equations (13) and (15), we can predict the progression of the interface and the change in velocity over time. The graph of position and velocity vs. time can be found in Figure 7. The position curve is proportional to $t^{1/2}$ and the velocity curve to $t^{-1/2}$, which is typical for diffusion controlled processes.

Diffusion Melting with Convection

Simple convection is incorporated into the model in this section. Convection currents are not modeled explicitly. The effect of convection in the reservoir on boundary conditions between the capillary and the reservoir is explored.

Convection in the reservoir is modeled in the same way as above in *Diffusion into a Capillary*. Convection currents in the liquid keep the entrance to the capillary supplied with solute such that it remains at the bulk value at all times. The boundary equation for this situation can be written as

$$C(0, t) = C_{bulk} . \quad (19)$$

Solving (7) and (8) for the boundary equations (11) and (19) gives, in the liquid,

$$C(z, t)|_L = C_{bulk} + (C_L - C_{bulk}) \frac{erf(d_L)}{erf(d_{L-I})} . \quad (20)$$

(17) still applies in the solid. The same equation for concentration in the solid without convection applies for the situation with convection. However, this does not mean that the same concentration profile will result in the solid, because d_{S-I} will be different under these conditions.

Equations (17) and (20) are plugged into (9) and the result is

$$\sqrt{\pi} = \frac{C_{bulk} - C_L}{C_L - C_S} \frac{e^{-z_{L-I}^2}}{z_{L-I} erf(z_{L-I})} + \frac{C_0 - C_S}{C_L - C_S} \frac{e^{-z_{S-I}^2}}{z_{S-I} (1 - erf(z_{S-I}))} . \quad (21)$$

Figure 8 displays the resulting concentration profiles from (21) and (17) and using (18) to calculate d_{L-I} and d_{S-I} . The physical values are the same that were used for Figure 6. The plot

starts from 0 cm instead of -1 cm because, for this situation, all of the negative values have a concentration of $C = C_{\text{bulk}}$ at all times. Figure 9 plots position and velocity of the remelting interface against time via equations (13) and (15). As expected, the pace of the reaction is higher when solute reaches the interface more quickly. At 3000s, the interface will have been displaced almost twice as far with convection than the case modeled without convection.

Experimental Analysis

The equations of the lines in Figures 7 and 9 come from equations (13) and (15). They are of the following forms:

$$z_I(t) = At^B, \quad (22)$$

for position and

$$v(t) = \frac{dz_I}{dt} = ABt^{B-1}. \quad (23)$$

for velocity. A and B are constants. When experiments are performed and position vs. time and velocity vs. time profiles are collected, the data can be fit with lines of least regression to mathematically describe the trend. If a power equation provides the best fit and B is close to 0.5, the models described above may be valid and there may be diffusion controlled melting in the capillary. If this is the case, then the following relationship originating from the combination of (14) and (22) holds:

$$A = 2d_{L-I}\sqrt{D_L} = 2d_{S-I}\sqrt{D_S}. \quad (24)$$

Using this relationship, the value of d_{L-I} can be extracted from experimental data. This value can yield information about the amount of convection present in the system and the degree of departure from equilibrium of the interface concentrations. This topic is described in more detail in the *Results* and *Discussion* sections.

Diffusion Coefficients

For the calculations, the diffusion coefficient was assumed to be constant throughout the path from the reservoir to the interface despite the fact that it changes slightly with composition (see Table 1). The change is small for C195-T210 (see *Results*), $< 3\%$, but is larger for the other conditions, C429-T210 and C429-T175. The change in diffusion coefficient with concentration makes Fick's Second Law, (1), a much more complicated differential equation that has never been solved, to the knowledge of this author, for the case of solute diffusion. Therefore it was chosen to take the diffusion coefficient as the average of the diffusion coefficients at the bulk and at the interface. This value is used as a constant in (1). The diffusion profiles are approximately linear, so this may suffice.

The resulting position profiles calculated from the data show a dependence on the square root of time (see *Results*), so this approximation appears to be valid. Had the diffusion coefficient's dependence on concentration affected the profile in a significant way, the profile may not have had this relationship with time.

Thermodynamics

Several authors have reported cases in which samples appeared to exhibit solid interface concentrations below the equilibrium values [19, 20]. The data comes mostly from EDX measurements of interfaces of remelted samples. Precise locations of the remelting interfaces were determined from using a novel technique. The grain boundaries of the solid were decorated with precipitates that the authors claimed would not affect the remelting rates. The interface could be found by polishing the surface and connecting the tips of the grain boundaries with a line. The conjecture of equilibrium not being reached at the interface was supported by

computer simulations [20]. The calculated velocities matched the experiments much more precisely when non-equilibrium interface concentrations were used as input parameters.

Hillert and Årgen initially opposed the idea that local equilibrium at the interface was lost during remelting [7]. They point out that the agreement between the simulation [20] and experimental data collected by Rettenmayr et al. [19] is due in part to curve-fitting and assumptions made by the authors. Furthermore, they call attention to a concentration “spike” (a sharp concentration gradient) that the authors found near the interfaces of their samples [19]. It was proposed that for this spike to occur at the observed melting velocities, local equilibrium at the remelting interface must have been reached. The authors of had offered no reason as to why this should not be true [20].

However, in a reply to Hillert and Årgen, Rettenmayr addressed their concerns [8]. First, he compared two empirical equations for determining the liquid interface composition as a function of melting velocity. The equation presented by Rettenmayr,

$$C_L^* = \frac{[C_L + C_0(av)]}{[1 + av]}, \quad (24)$$

and the one presented by Hillert and Årgen,

$$C_L^* = \frac{[C_L + C_L^{\min}(av)]}{[1 + av]}, \quad (25)$$

are both modeled after the equation developed by Aziz to describe deviations from equilibrium during rapid solidification [21]. The symbols have been changed from those of the original publication in order to fit the conventions of this paper. In (24) and (25), C_L^* is the liquid interface concentration, v is the interface velocity, and a is a fit parameter with units of time / distance. The other symbols have their usual meaning. It should be emphasized that neither

equation has a theoretical background. They simply deliver the desired curve shape and asymptotic behavior that the authors desired.

Both equations have qualitative merit. In the case of (24), at low velocities the interfacial composition approaches the equilibrium value. If the melting rate is low enough to allow diffusion in the liquid to transport solute to the depleted interface, then the interface should remain at the equilibrium value. Furthermore, the interface composition approaches the bulk solid composition as the melting velocity approaches infinity. At infinitely high velocities, there would be no time for solute from the liquid to diffuse to the interface. Therefore the composition of liquid produced at this velocity would be the composition of the solid that melted.

There is a stipulation attached to Equation (24), according to the authors. Since a driving force cannot be defined for liquid interface values lower than C_L^{\min} , they recommend plugging this value in for the liquid interface concentration when (24) predicts any value $C_L^* < C_L^{\min}$.

On the other hand, Hillert and Årgen proposed (25), a similar equation with one significantly different conclusion. At low velocities, the equation delivers the same conclusion as (24); the interface composition of the liquid should match the equilibrium value. However, at infinitely high velocities, (25) predicts that the interface composition will asymptotically approach C_L^{\min} , the lowest interface composition for which a driving force for melting can be defined.

When considering the stipulation attached to equation (24), it appears that the equations are very similar indeed. The only difference between them is the nature of either equation's approach to C_L^{\min} . While (24) predicts that C_L^* approaches it quickly and then matches it for all velocities higher than a certain value, (25) approaches the value in a smooth asymptotic fashion.

Finally, Rettenmayr [8] dismisses the differences between the equations and claims that such velocities at which the differences would be apparent cannot be obtained during solutal melting. This kind of melting constitutes unconstrained interface migration and will only proceed as quickly as the physical parameters allow it. The highest melting rate during the entire process will occur as soon as the solid and liquid come into contact, but will only prevail for less than one second. At the moment of contact, there will ideally be an infinite chemical potential gradient and the interface (because of the pure solid) and the composition of the liquid will be the bulk liquid value. After the first layer of solid is melted, the chemical potentials, and therefore the driving forces for diffusion and melting, will decrease sharply. As melting proceeds, the velocity only decreases.

In regards to the concentration spike mentioned by Hillert and Årgen [7], Rettenmayr [8] outlined a consistent qualitative theory for solutal melting. This theory relates to other phase changes and is examined further by Hillert and Rettenmayr [6]. It was emphasized by Rettenmayr that no consistent and detailed thermodynamic theory had yet been worked out in the literature, and thus, the actual values of the interface concentrations could not be predicted. The descriptions presented by Rettenmayr et al. [6, 8] were qualitative ones that show how deviations from equilibrium are possible, despite the presence of the concentration spike in the solid.

Rettenmayr explains that when describing the situation of bringing a solute enriched liquid in contact with a solute depleted solid via Gibbs free energy diagrams (G - X curves), one could define a driving force for melting as well as solidification by drawing the appropriate tangents Figure 10 [8]. Thus, the direction of the phase change from this point of view is ambiguous. However, when observing the situation experimentally, the phase change has to

proceed in one direction or the other. The phase change to be observed is determined by the kinetics.

Consider a situation that has small driving force for melting and a large driving force for solidification, i.e. a pure solid dipped into a liquid of the same temperature at a concentration just above the liquidus. It has been shown that the direction of the initial phase change is determined by the relative values of the diffusion coefficients in the liquid and the solid. In this case, since the diffusion coefficient in the liquid is relatively large, melting will occur first despite the larger driving force for solidification.

To understand why this occurs, one must consider the mechanisms of melting and solidification controlled by solute transfer. The roles of mass transfer and partitioning for both processes must be understood in order to determine which will prevail when driving forces for both exist.

Origins of driving forces for phase changes in binary systems are discussed here. Although equations for the calculation of these forces are presented, the scenarios examined here are qualitative. The analyses presented follow the sharp interface model [22] which has proven to be acceptable in this and other work [6, 9, 20].

Solidification of an Initially 100% Liquid Alloy

First, we will consider solute controlled solidification. During this discussion, it is assumed that the rate of diffusion in the liquid is limited; however, it is much higher than the rate in the solid. Consider the alloy of composition X_{alloy} at temperature T_i in Figure 11. As the temperature is lowered to T_f , the alloy solidifies. Flemings provides an in-depth account of the solidification of a binary alloy as the temperature drops [23]. Solidification initiates at the liquidus temperature T_L , and the composition of the first solid that forms will match the solidus

composition at T_L , denoted X_{S-min} in Figure 11. As the temperature of the interface drops, the liquidus composition increases and solidification continues. Assuming that local equilibrium at the interface prevails, the composition of the produced solid matches the solidus composition for any given temperature in the S + L region. Of course, since this is a eutectic system, the concentration of the produced solid is always lower than the parent liquid. As each layer solidifies, the excess solute that is not incorporated into the solid is rejected into the liquid. This rejection causes solute to build up in the region near the interface. Diffusion and convection work to eliminate the concentration gradient between the buildup at the interface and the bulk (see Figure 12), but in most cases the interface reaction is faster than mass transfer and the size of the solute buildup increases. If the ingot is sufficiently long, the interface temperature eventually reaches the solidus temperature, T_S , and the process reaches a steady state from which point the product solid has the composition X_{alloy} steady state solidification occurs at this composition. Steady state solidification continues until the layer of solute buildup approaches the edge of the ingot. Eventually, there is nowhere for the solute to be rejected to, and the composition of the solid being produced rises to X_E , the eutectic composition. After this point is reached, two phase eutectic solidification occurs. Since negligible diffusion in the solid was assumed, the final concentration profile would resemble Figure 13. The depletion in the initial transient region should equal the enrichment in the final transient.

Hillert and Rettenmayr describe the conditions required for solidification and the boundary conditions, in terms of interface concentrations, within which the process will continue [6]. The driving force for a phase change is defined as the change in the free energy as a substance changes phases. Theoretically, an alloy will change its phase whenever it can reduce its local free energy by doing so. With this in mind, we can define the interface compositions at

which a solid \rightarrow liquid transition is possible by inspecting the relevant G-X curves. For a given X_L^* , the possible solid interface concentrations are shown in Figure 14. The equilibrium liquid and solid concentrations, X_L and X_S respectively, are determined by drawing the common tangent between the liquid and solid free energy curves. This tangent is also shown in Figure 14, but in others the tangent is omitted while the equilibrium compositions are marked on the X_B axis. In order to construct these figures, the composition of the liquid in the region that the phase change occurs, i.e. the composition at the interface, must be determined. The true value of the liquid interface concentration will be denoted X_L^* , following the convention of Flemings. Similarly, the composition of the solid at the interface will be denoted X_S^* . The changes in free energy for a liquid changing into a solid can be viewed by drawing the tangent to the liquid curve at X_L^* . The change in Gibbs free energy, ΔG_{total} , for solidification of a liquid of composition X_L^* to a solid can be expressed as the free energy of the tangent to the liquid curve at X_L^* subtracted from the solid free energy curve at the solid composition. Quantitatively,

$$\Delta G_{total} = (1 - X_\alpha^*) (\mu_\beta^A - \mu_\alpha^A) + X_S^* (\mu_\beta^B - \mu_\alpha^B). \quad (26)$$

Above, μ is chemical potential, and superscripts A and B represent the two alloying elements. α is the product phase and β is the parent phase. Therefore in a solidification reaction, α would be the growing solid and β would be the shrinking liquid. μ_β^A would be the chemical potential of A in the beta phase. Therefore, the phase change is thermodynamically possible for any solid composition at which the solid free energy curve lies beneath the liquid tangent at X_L^* because the phase change yields a negative free energy change. The maximum and minimum possible concentrations for the growing solid are marked by the intersections of the tangent with the solid curve (Figure 14). It should be noted that near the extreme solid concentrations, there is only a negligible amount of driving force available to overcome obstacles such as migration resistance

and increases in surface energy [22]. The presence of these barriers would push the maximum and minimum solid concentrations closer to C_S^{Gmax} , the solid composition that corresponds to the largest reduction in free energy with respect to C_L^* during the phase change. This value is found at the point of tangency between the solid free energy curve and a line parallel to the liquid tangent at C_L^* (Figure 14).

During steady state solidification, the temperature at the interface remains constant. Solute is continuously rejected into the liquid. Since the solid has a composition of C_S , solidification can continue until C_L^* equals C_L . Subsequently, the driving force for solidification is effectively destroyed. If temperature remains constant, solidification cannot continue unless the concentration at the liquid interface again drops below the equilibrium value, C_L for that temperature T^* . Since the concentration of the bulk liquid is lower than that of the interface, solute diffuses continuously away from the interface. Thus, again C_L^* drops below C_L . Driving force is created, and more solidification can occur. However, solute rejection continuously raises C_L back up to C_L . This cycle continues. Therefore, when the temperature remains constant throughout the alloy, and under the sharp interface model's assumptions (i.e. ignoring the interface kinetics) mass transfer in the liquid controls the interface migration rate because it controls the rate at which driving force for the phase change is created. As the interface reaches the end of the ingot, it encounters the final transient regime described above.

Similar treatment of this kind can be applied to other solidification situations and melting situations as well. Next, we will explore a similar treatment that can be applied to the melting process

Melting of an Initially 100% Solid Alloy

Melting can be either thermally or solutally driven. Woods differentiates the two mechanisms by calling the solid \rightarrow liquid phase change via the former mechanism melting, and via the latter dissolution [4]. However both will be referred to as melting throughout the present work. The mechanism should be clear from the context.

The process of thermal melting for an alloy is easy to describe since the partitioning process is not as complicated as during solidification. For the present Figure 15 shows an alloy initially of composition C_0 at temperature T_i . The temperature is raised, and as the alloy reaches the solidus temperature it begins to melt. The first liquid to be produced has a concentration close to that of C_L for T^* . The solute content for the liquid is higher than C_0 , the solid it was formed from. The source of the solute for this enrichment is the bulk solid. The composition profile in Figure 16 shows that a concentration gradient arises in the material between C_S^* and C_0 as T . The gradient arises because the solid interface remains at the equilibrium composition, C_S , however C_S itself drops as the temperature increases. As a result, solute diffuses from the bulk to the interface and enables the formation of solute rich liquid. The shaded areas in the Figure 16 remain the same size throughout the process. As the interface temperature rises through the L + S region, the solidus temperature drops significantly below the initial composition. The size of the concentration gradient increases, more solute flows to the interface, and more liquid is formed. The G-X curves for the alloy as it passes through the S + L region are shown in Figure 17. Eventually, when the interface temperature reaches the liquidus temperature, the ingot becomes 100% liquid of the concentration C_0 . The ingot remains in that state as the temperature rises to T_f .

Reaction between Two Initially Present Phases

The concept of X_I must be introduced in order to calculate the Gibbs free energy when dealing with phase changes as a reaction between two existing phases. X_I can be defined as the ratio of A atoms to B atoms being swapped across the phase interface as it migrates. Due to conservation of mass, it can be calculated as

$$X_I = X_\alpha^* \frac{J_\beta}{J_\beta + J_\alpha} + X_\beta^* \frac{J_\alpha}{J_\alpha + J_\beta}. \quad (27)$$

Arranging, we get an expression that relates X_I to the parent interface concentration X_β^* .

$$X_\beta^* - X_I = \frac{(X_\beta^* - X_\alpha^*)}{\left(1 + \frac{J_\alpha}{J_\beta}\right)}. \quad (28)$$

The flux of B, J , in either phase is positive towards the interface (see Figure 18). If the phase change occurs as a change in a sample that is initially 100% parent phase β , then X_I equals the concentration of the product phase, X_α . That is to say, all of the solute used to form the product phase *must* come from the parent phase, and hence it must cross the phase boundary. If the phase change is a reaction between two phases, then some of the solute needed to form the product phase α can come from the pre-existing α . The more solute that can be supplied by the pre-existing phase, the less needs to be diffused across the interface. As shown in (27), the amount supplied by the amount diffused across the interface depends on the initial concentrations of both pre-existing phases and the value of the flux in each phase. The latter depends greatly on the relevant diffusion coefficients.

The equation for the change in free energy for a phase change from β to α , (26), becomes

$$\Delta G_{total} = (1 - X_I)(\mu_\beta^A - \mu_\alpha^A) + X_I(\mu_\beta^B - \mu_\alpha^B). \quad (29)$$

For a graphical explanation of the terms in (29), see Figure 19. For phase changes starting from a single phase, this equation becomes (26).

Solidification as a Reaction between 2 Phases

Now we will consider solidification as the result of a reaction between two phases at a fixed temperature. Consider the two hypothetical alloys of the same base in a binary eutectic system at temperature T shown in Figure 20. In order to scrutinize solidification, we must eliminate any theoretical driving force for melting. This is accomplished by giving the two alloys the concentration profiles shown in Figure 21. The initial boundary layer in the solid is necessary to eliminate the driving force for melting. The reason for this is clarified in the next section. The alloys have the same weight, and the length of each is much larger than the length of the solute boundary layers in either phase during solidification. It is assumed that the amount of solute needed to make this boundary layer is negligible compared to the composition of the solid alloy as a whole, and thus $X_0 \approx 0$. Finally, it is assumed that the rate of diffusion in the solid is much lower than in the liquid, and thus complete mixing in the liquid prevails at all times. The alloys are brought into contact as shown in Figure 21, with the saturated end of the solid against the liquid. The final equilibrium state of the resulting alloy can be shown on the phase diagram 20. Examining the G-X diagram 22 for the moment the alloys come into contact reveals that a driving force for solidification exists. The process is similar to that described for solidification from an initially 100% liquid system. The depletion in the liquid gives rise to a driving force for solidification. Since $k < 1$, solidification causes solute to be rejected when a layer solidifies. The only difference between this situation and the one described above is that the initial solid present in this situation may accept some solute from the liquid to help adjust its composition to C_S . Since diffusion in both the solid and the liquid is away from the interface, $J_S < 0$ and $J_L < 0$. Therefore, from (28) we can see that X_I is larger than X_S^* . Assuming that diffusion in the solid is much slower than in the liquid, we can assume that the conditions for this

scenario are similar to if the initial solid was not present at all. By plugging zero in for J_S , we see that if the solid was not present, then $X_I = X_S^*$. So, qualitatively, we know that X_I is larger than X_S but closer to X_S than X_L . See the G-X curve in Figure 22 for the relative positions of the concentrations and the graphical representation of the driving force ΔG . Throughout the process, the shaded regions in 23 remain the same size. This figure shows the concentration profile during solidification with two phases present initially. The diffusion in the solid is exaggerated to make the concentration profile in the solid visible.

Indeed, Rettenmayr described a similar reaction between a solid and a liquid in which the solid is solutally melted for the entire span of time during which a driving force for melting exists [8]. After the melting driving force disappears in Rettenmayr's description, the solidification is controlled by diffusion in the solid.

Melting as a Reaction between 2 Phases

Consider the case of melting as a reaction between two phases at a fixed temperature. The treatment for this case is the same that given by Rettenmayr and Hillert [6]. The simplest case occurs when one considers the reaction between the alloys shown in Figure 24, equal in amount and fixed at temperature T . The solid has a composition $C_0 > C_S$ and the liquid has a composition above the liquid equilibrium value. The equilibrium conditions of the system after the alloys are brought into contact are marked. The G-X curves for the initial contact can be used to show the driving forces (see Figure 25), and it is apparent that only a driving force for melting exists. The concentration of the melted solid is much lower than the bulk concentration of the liquid. The change in concentration of the solid as it melts must be accommodated by diffusing solute towards the interface. If there was only one phase present initially, then this concentration difference would have to have been accomplished by diffusion in the parent phase.

However, since solute rich liquid is in contact with the system, the change in composition can be accommodated by the pre-existing liquid as well. The concentration profile during the melting process is shown in Figure 26. Since the melting alloy is in contact with a liquid of concentration $C_{\text{bulk}} > C_L$, concentration gradients in both the liquid and the solid diffuse solute towards the interface in order to support the concentration change upon melting. If the liquid were not present, then X_I would equal X_S^* . Using equation (28), we find that X_I is greater than X_S^* . The presence of the liquid therefore facilitates more trans-interface diffusion of solute to accommodate the phase change. The G-X curves in Figure 25 show the relative positions of relevant values and the driving force for melting.

Melting as a Reaction Between Two Initially Present Phases when Two Opposing Driving Forces Exist

Finally, we consider the case that occurs in the present study. The situation concerns the outcome of a situation when a driving force for melting and solidification can be defined. Rettenmayr [8] and Rettenmayr and Hillert [6] explore this in detail. Figure 27 shows the initial compositions of two alloys at the same temperature; one is a pure solid, and the other a solute-rich liquid. Both alloys have homogeneous compositions, and they are equal in amount. The phase diagram shows the final equilibrium state of the alloy. However, the approach to equilibrium is not as straightforward as in the previous two examples; driving forces for solidification as well as melting exist when the alloys are first brought into contact. This can be seen in the G-X curves introduced before in Figure 10.

In terms of driving forces, the direction of interface migration is ambiguous. However, when the metals come into contact, the interface can only migrate in one direction. The outcome

will depend on the kinetics of the situation. From the discussions of the situations presented earlier, a prediction of the outcome can be made.

The answer lies in the concentration profile that develops in the system. Looking at the concentration profile at this point in Figure 28, it is apparent that gradients exist between 1) the bulk liquid and the liquid interface, and 2) the solid interface and the bulk solid. Diffusion to the liquid interface from the liquid bulk is, of course, controlled by D_L , and diffusion into the solid by D_S . Concentration gradient 1) will cause solute to flow towards the interface, thus raising C_L^* above the steady state value. This in turn creates a driving force for melting. On the other hand, gradient 2) diffuses solute away from the liquid interface and causes C_L^* to drop below the equilibrium value, which creates driving force for solidification. Therefore, in this situation, we can relate solidification kinetics to D_S and melting kinetics to D_L . Assuming the $D_L \gg D_S$, it is reasonable to assume that the melting will occur until the concentration gradient in the liquid disappears and can no longer supply the interface with solute. The driving force for melting must of course be calculated at X_I . According to (28), $X_I < C_S^*$, so less mass is transferred across the interface than if the solid were not initially present. Afterward complete mixing is recognized in the liquid, diffusion in the solid can take over and diffuse solute away from the liquid, consequently driving solidification. The process continues until the solid is saturated with solute.

Loss of Equilibrium at the Melting Interface and C_L^{\min}

Bringing the discussion of a reaction between two phases one step further, Rettenmayr [8] and Rettenmayr and Hillert [6] make another assumption based on the large difference between C_L and C_S . If diffusion in the solid is slow enough, one can assume that the interface composition for that phase is close to or equal to the initial composition. If this is the case, an

interesting phenomenon arises in the system. Referring to the G-X curves in Figure 29, we can see that *a driving force for melting can be defined for liquid compositions within the two-phase field*. The lowest theoretically possible concentration in the liquid occurs when there is negligible diffusion in the solid (hence from (28) $C_I \approx C_S^* \approx 0$) and the driving force needed for migration is negligible (hence $\Delta G \approx 0$). This value of C_L^* is dubbed C_L^{\min} by Rettenmayr [19] and is noted on Figure 29.

This loss of equilibrium at the interface of course predicts different migration rates than equilibrium melting. This is one of the ways that non-equilibrium melting can be detected. Rettenmayr, Warkentin, Rappaz, and Exner used this method to discover evidence that melting occurred at a liquid interface composition within the solid + liquid phase field [20]. At first, after giving the relevant physical constants to the program, the predicted velocities were much lower than what was observed in experiments. Lowering the liquid interface composition to a value near the theoretical minimum, C_L^{\min} , the simulation and the experimental results were in much better agreement.

One way to predict the effects of the interface compositions deviating from equilibrium is via the diffusion solution for solutal melting. The relevant equations are below.

$$\frac{z}{2} = d_{L-i} \sqrt{D_L} = d_{S-i} \sqrt{D_S} \quad (14)$$

$$v = d_{L-i} \sqrt{\frac{D_L}{t}} = d_{S-i} \sqrt{\frac{D_S}{t}} \quad (15)$$

$$\sqrt{\pi} = \frac{C_{bulk} - C_L}{C_L - C_S} \frac{e^{-d_{L-i}^2}}{d_{L-i} (1 + \text{erf}(d_{L-i}))} + \frac{C_0 - C_S}{C_L - C_S} \frac{e^{-d_{S-i}^2}}{d_{S-i} (1 - \text{erf}(d_{S-i}))} \quad (18)$$

The meanings of the symbols have been described above. (14) gives an expression for the position of the interface against time and (15) for velocity against time. (18) relates the

dimensionless position d to the concentration profile of the system. Although the equations cannot be derived algebraically, the position-time and velocity-time profiles depend on the values of the interface concentrations because of (18).

The migration rate of the interface is inversely proportional to the interface concentrations. Therefore, lower interface concentrations correspond to higher migration rates. The highest possible rate can be found by replacing zero for C_S and C_L^{\min} for C_L . Ignoring convection and interface reaction kinetics, the interface migration rate must fall somewhere at or between the migration rates predicted by equilibrium interface concentrations and the minimum interface concentrations.

Kinetics

Analysis of the kinetics of the reaction may give insight into the mechanisms of solutal melting as well as empirical relationships between temperature, driving force, and velocity. Several authors have investigated solutal melting kinetics in the past. Kang studied the effects of strain and formation of intermetallics on the solutal melting (called dissolution by Kang [15]) of Ni in liquid Sn [15]. Rettenmayr et al. studied the kinetics of melting aluminum by way of Mg rich Al-Mg liquid alloys [9]. Johnson ran simulations to explore the kinetics of phase changes in binary alloys [24]

The activation energy is indicative of the mechanism of a reaction. The authors mentioned used similar approaches to calculating the activation energies for melting. Both measured the dissolution rate at different temperatures and then used an Arrhenius relationship, (30), to calculate the activation energy Q and pre-exponential constant a_0 (often interpreted as the atomic jump rate).

$$rate(T) = a_0 \ln\left(\frac{Q}{RT}\right). \quad (30)$$

If the activation energy for melting matches activation energies for another process, say diffusion or formation of intermetallics, then one can regard the results as evidence that this process kinetically controls the rate.

Rettenmayr takes the kinetic analysis a step further by measuring the dependence of the rate on supersaturation, i.e. the driving force for solutal melting. Rettenmayr proposed that this dependence is part of the coefficient a_0 . He equated a_0 to the product of three terms: the supersaturation ΔC (equal to $C_{\text{bulk}} - C_L$), the slope of the line relating supersaturation to the reaction rate K_C , and a final term K_K that characterizes the contribution of interface kinetics. K_K is dimensionless. It characterizes the rate of atoms changing phases without the dependency on

temperature or driving force. Rettenmayr's approach for characterizing kinetics is used in this work.

The Sn-Bi System

Sn and Bi are both post-transition metals occurring in the periodic table between the transition metals and the metalloids. Both elements have notably lower melting points and hardness than transition metals. Sn has a wide variety of applications from plating steel food containers to prevent corrosion to an alloying element in organ pipes to superconductors. It has therefore been widely studied in the past. Bi applications are as varied as those of Sn; it is used in cosmetics, anti-diarrheal medicine (Pepto-Bismol®), brasses and iron alloys, thermocouples, and electronic applications. The two metals have been alloyed to create lead free solders.

Sn-Bi alloys have been studied in the past as model systems. Referring to the phase diagram in Figure 30 [25], the reasons for this are clear. Sn-Bi is a simple eutectic system with low melting/liquidus temperatures (allowing for more precise control over experimental parameters), and no intermetallics. Simplicity was one of the reasons it was chosen for this study. The other main reason that this system was appealing for this work was the ample amount of literature available on its properties. The thermodynamic properties have been assessed by many authors [26-29]. Table 1 details the alloy properties relevant to this study.

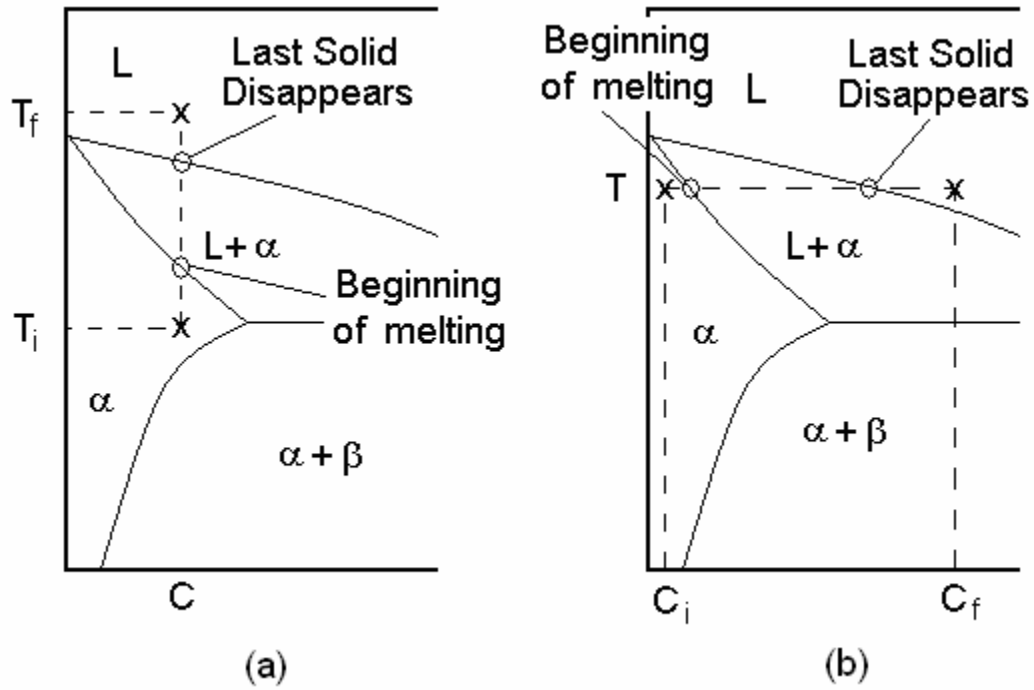


Figure 1 Different paths to melting on the T-X phase diagram. In (a), the phase change is facilitated by a rise in temperature. In (b), the phase change is facilitated by a change in concentration.

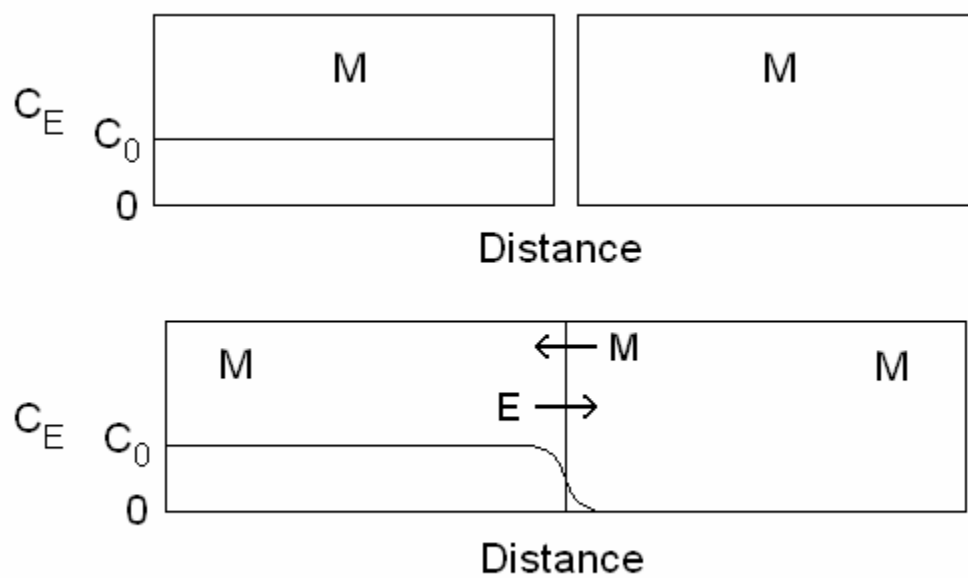


Figure 2 Simple 1-D diffusion schematic. The solute flows from high concentration areas to low concentration areas.

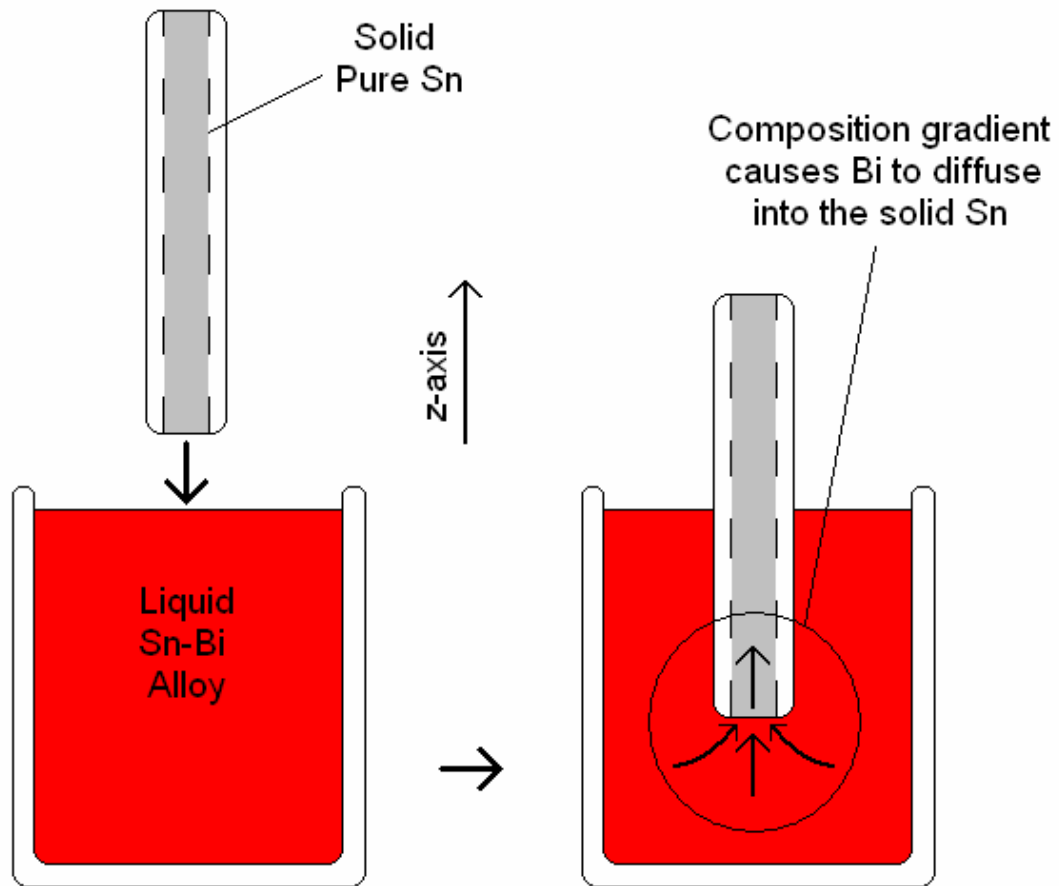


Figure 3 Schematic of the experimental concept. The metal-filled capillary is dipped into the solute-rich reservoir. The solute then diffuses into the solid metal via the opening in the tip of the capillary. Since the capillaries are vertical in the lab reference frame, the capillary axis is labeled the z-axis.

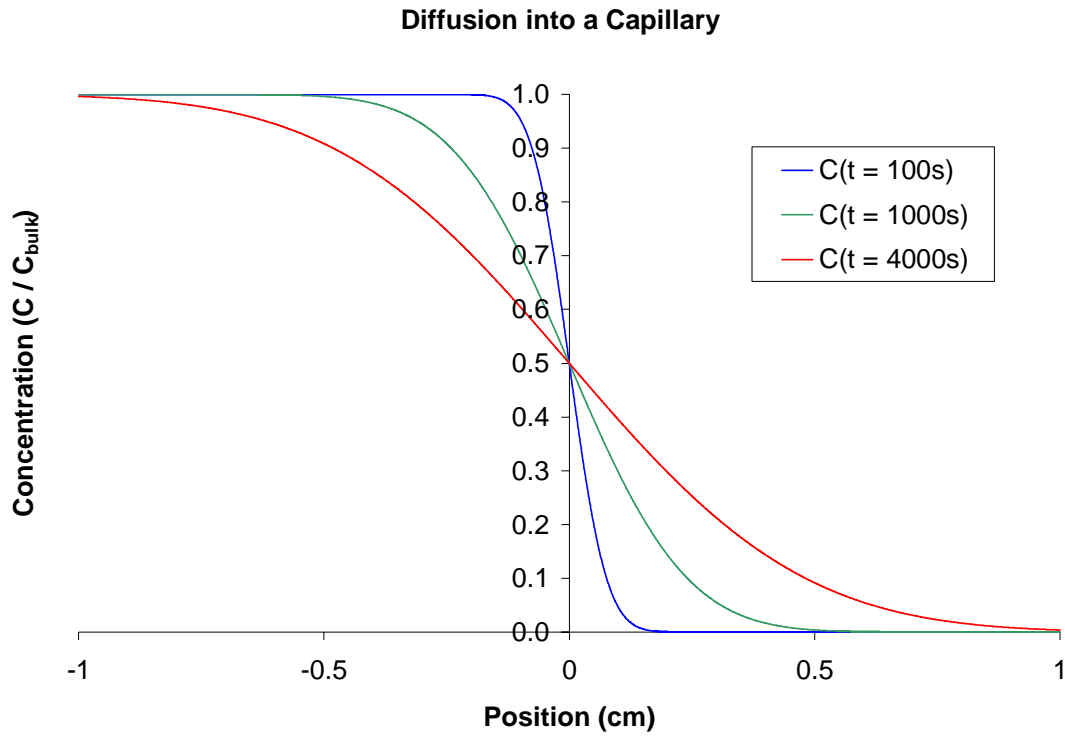


Figure 4 1-D diffusion into a capillary with no convection in the reservoir. Position represents the distance from the opening of the capillary; hence, the position $z = 0$ represents the opening of the capillary. Material properties were taken from the Sn-Bi system at 210C.

Diffusion into a Capillary with Convection in the Reservoir

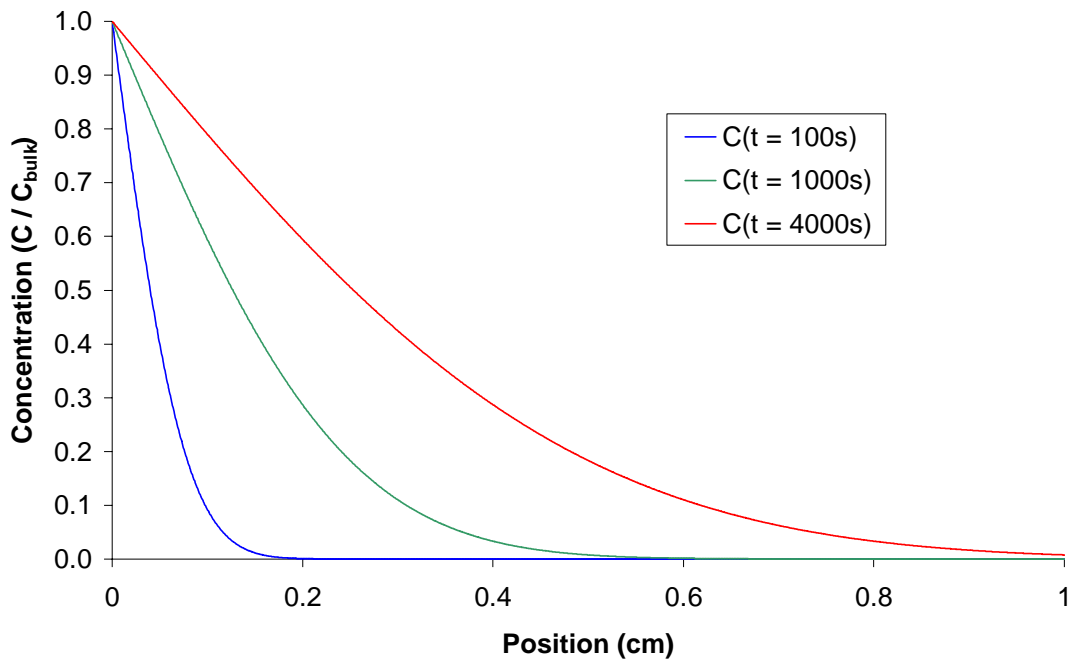


Figure 5 1-D diffusion into a capillary with convection in the reservoir. Position represents the distance from the opening of the capillary; hence, the position $z = 0$ represents the opening of the capillary. Material properties were taken from the Sn-Bi system.

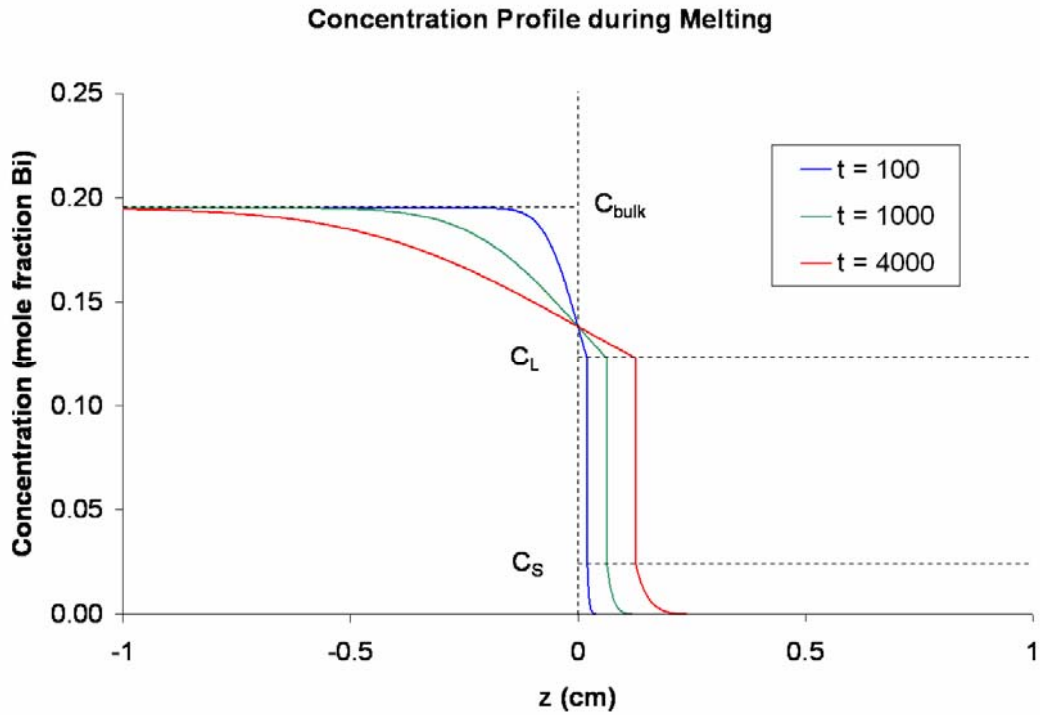


Figure 6 1-D diffusion into a capillary with a melting interface and no convection in the reservoir. The left side of the graphs represents the liquid and the right side represents the solid. The vertical line in each profile represents the solid/liquid interface. Material properties were taken from the Sn-Bi system at 210°C. The diffusion constant in the solid was multiplied by 1000 to make the profile visible. The position $z = 0$ represents the opening of the capillary.

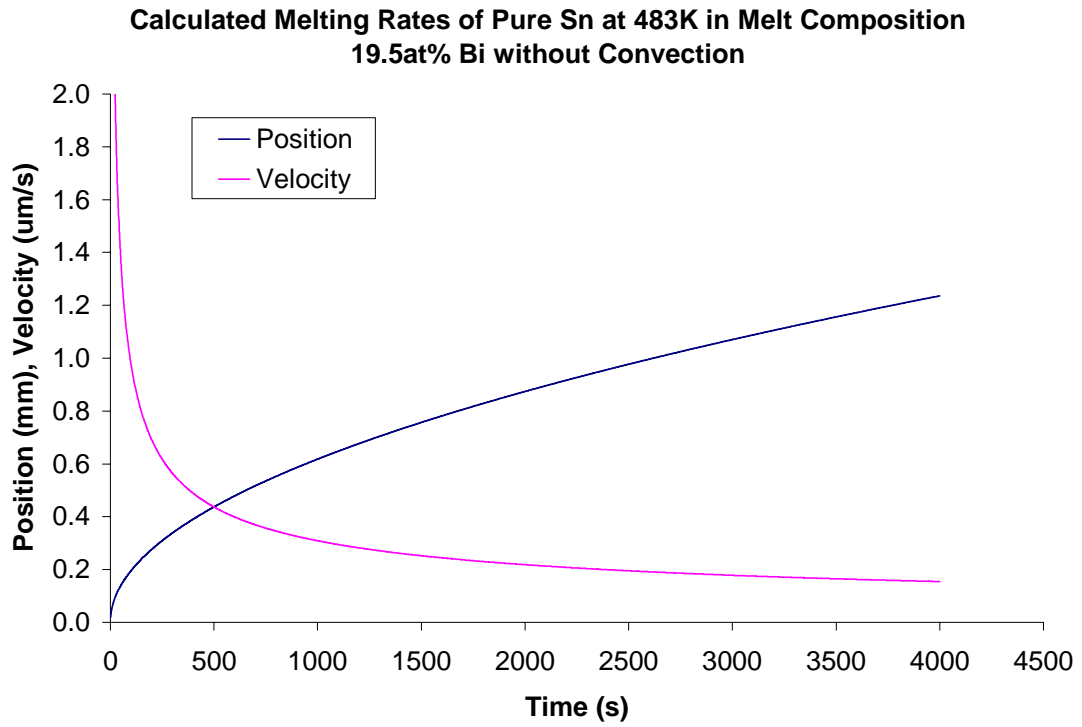


Figure 7 The predicted values of position and velocity against time for the conditions used to calculate the concentration profiles in Figure 6.

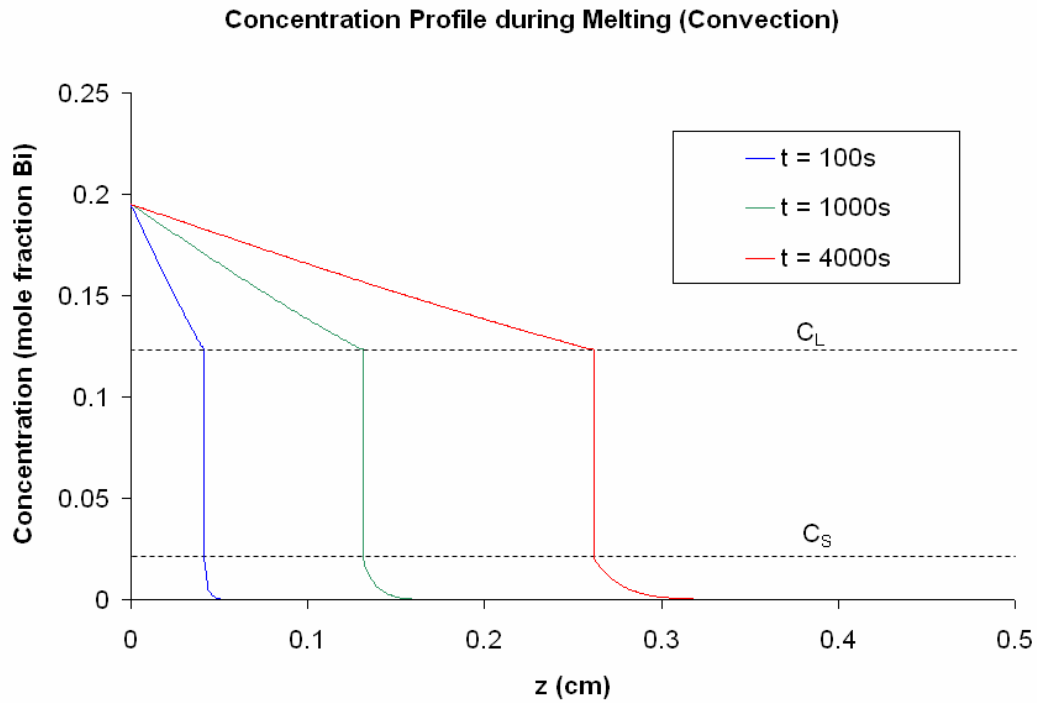


Figure 8 1-D diffusion into a capillary with a melting interface and convection in the reservoir. The left side of the graphs represents the liquid and the right side represents the solid. The vertical line in each profile represents the solid/liquid interface. Material properties were taken from the Sn-Bi system at 210°C. The diffusion constant in the solid was multiplied by 1000 to make the profile visible. The position $z = 0$ represents the opening of the capillary.

**Calculated Melting Rates of Pure Sn at 483K in Melt Composition
19.5at% Bi with Convection**

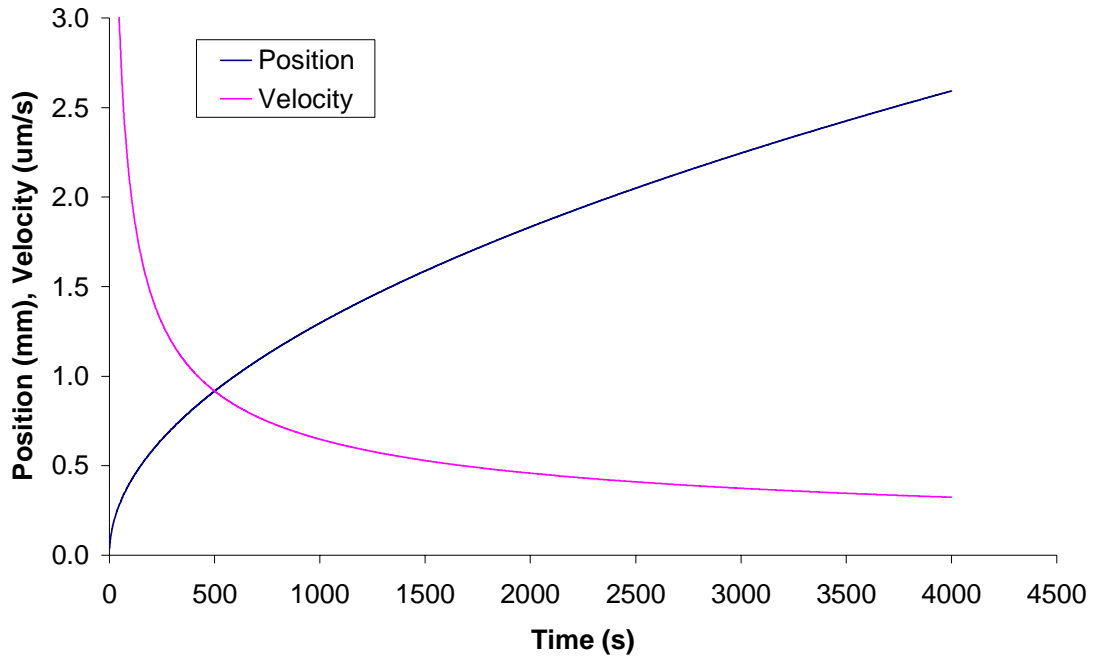


Figure 9 The predicted values of position and velocity against time for the conditions used to calculate the concentration profiles in Figure 8.

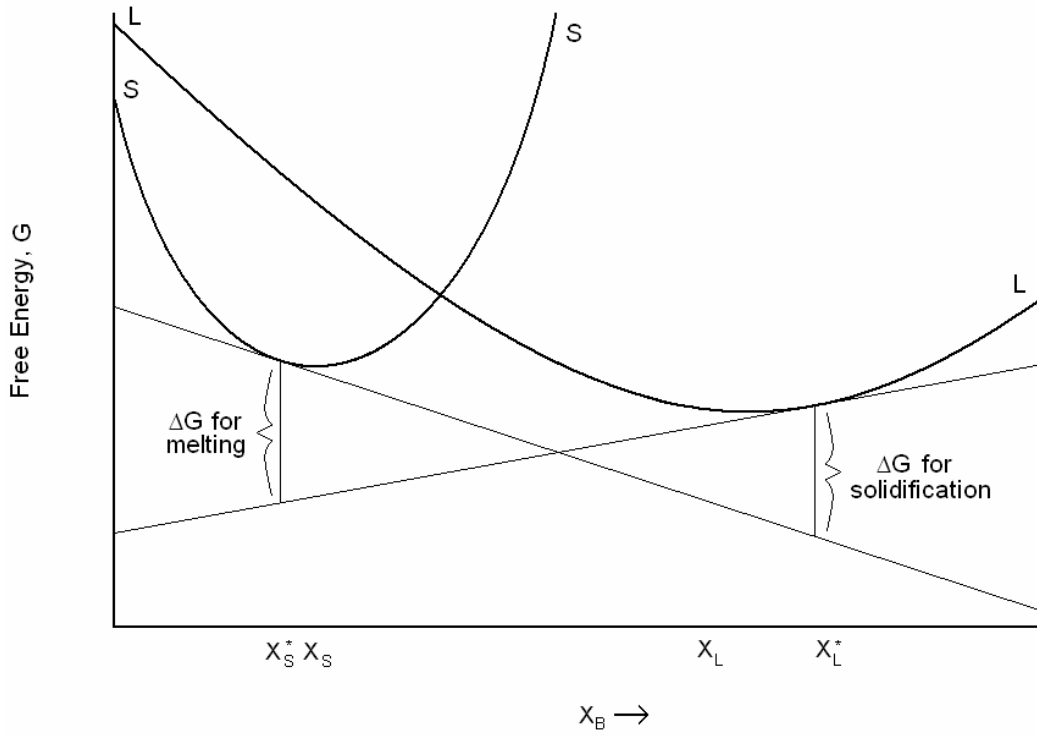


Figure 10 G-X diagram exhibiting the two driving forces that arise for the interface values marked.

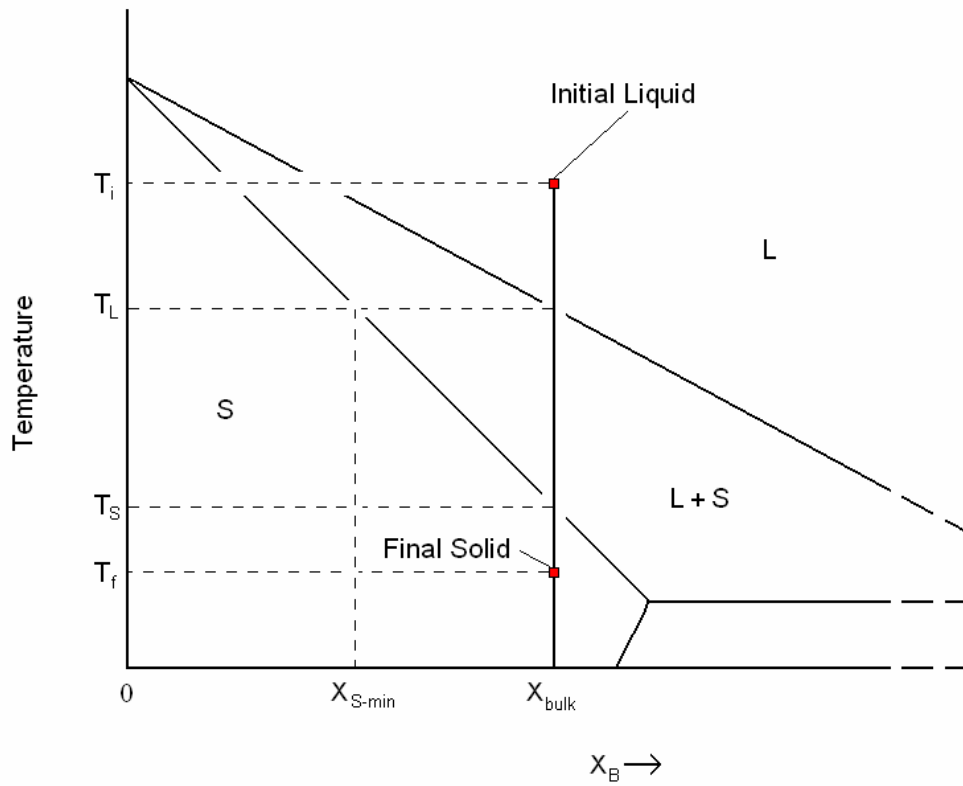


Figure 11 Phase diagram showing the conditions during solidification. At any given temperature during the cooling through the S + L phase field, the concentration at the interface equals the solidus value.

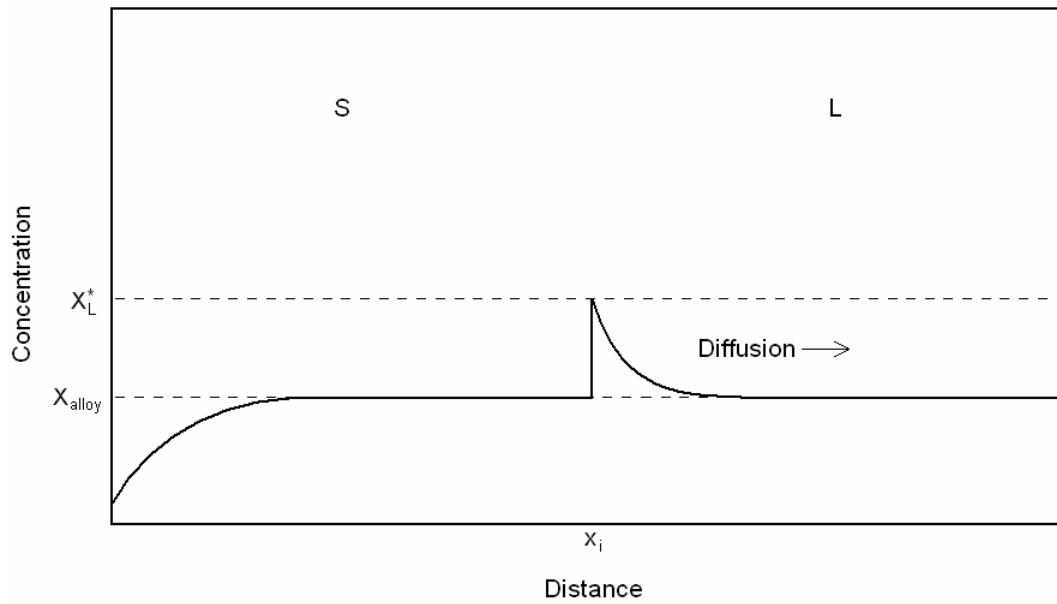


Figure 12 Concentration profile during solidification. Solute is rejected from the solid into the liquid causing the build-up at the interface. The initial transient occurs as the alloy passes through the S + L phase field.

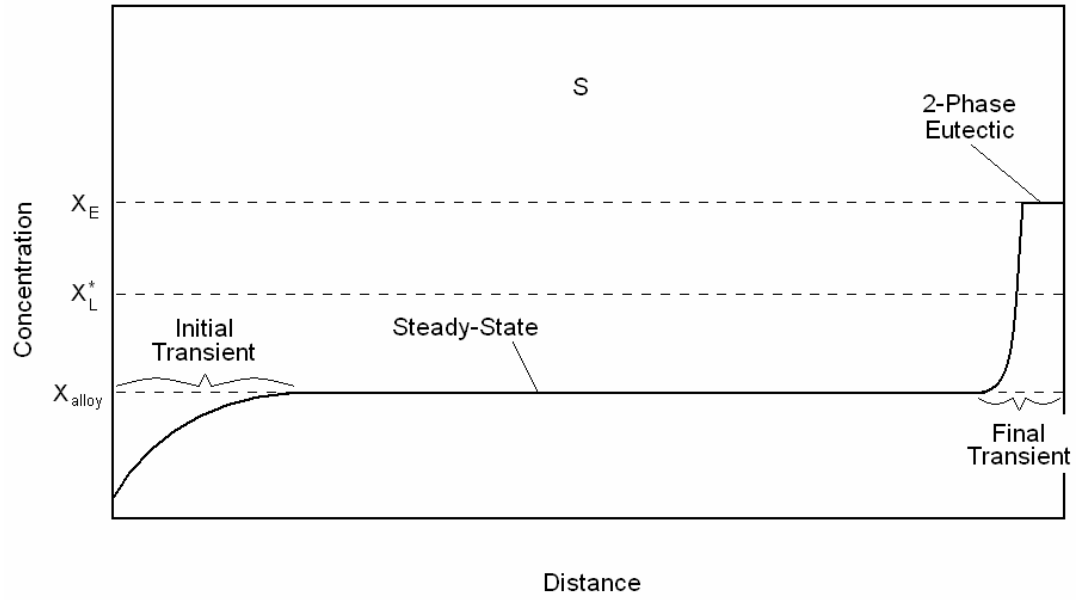


Figure 13 Concentration profile of the solidified ingot from Figure 12. The depletion in the initial transient equals the enrichment in the final transient.

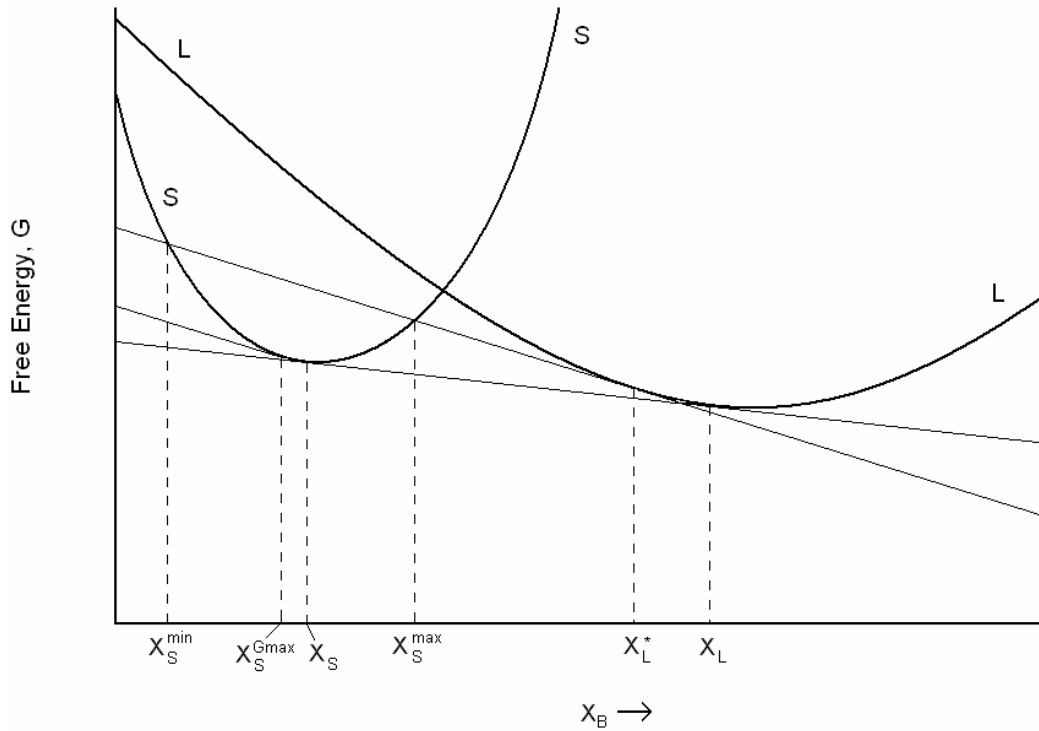


Figure 14 G-X diagram showing the determination of equilibrium concentrations by drawing the common tangent. Also, the maximum and minimum concentrations of solid that can be formed from the marked liquid interface concentration are marked. Solid can only form if the tangent to the liquid curve is above the solid curve denoting a negative free energy change upon changing phases. Also, the diagram shows the solid concentration for the largest free energy change.

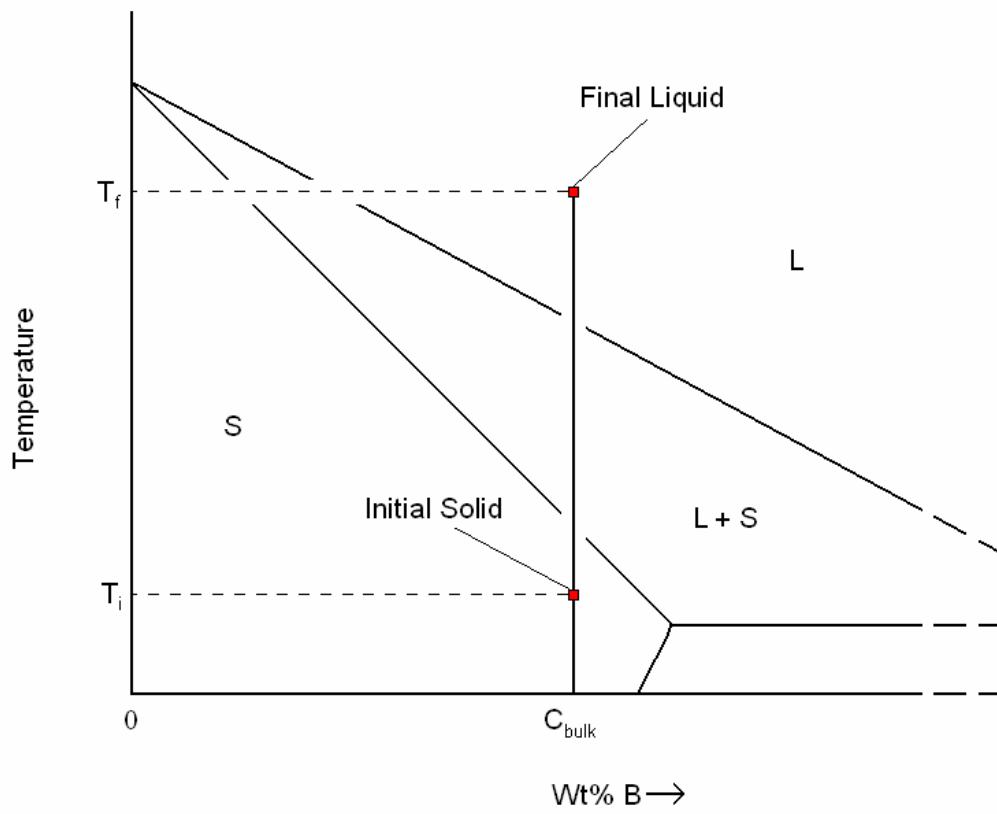


Figure 15 Phase diagram showing the initial and final conditions during melting of an alloy.

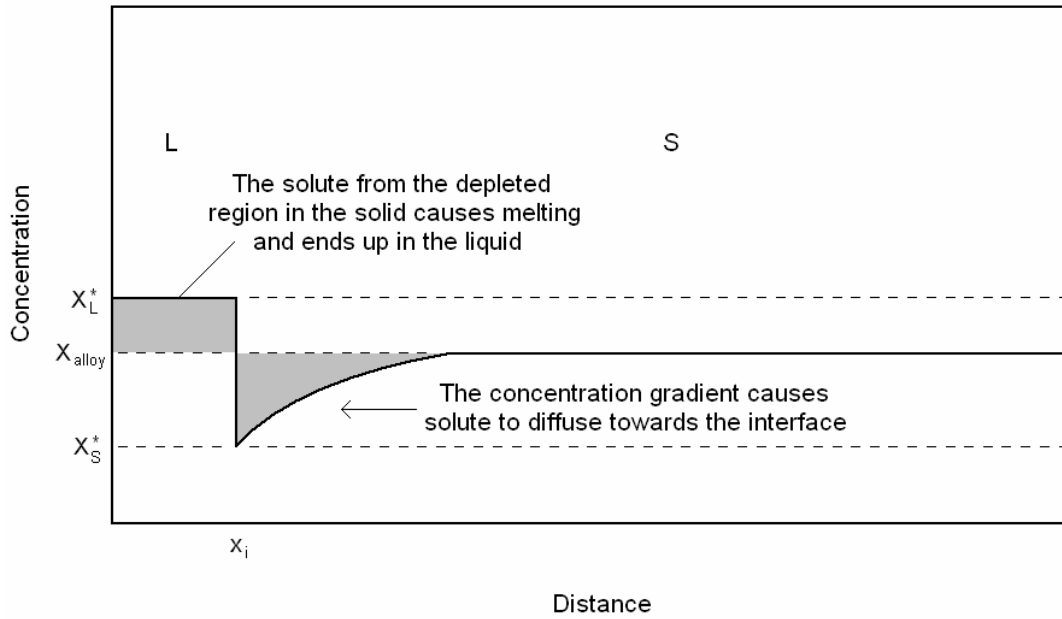


Figure 16 Concentration profile during the melting of an alloy. There is a depletion of solute near the solid interface.

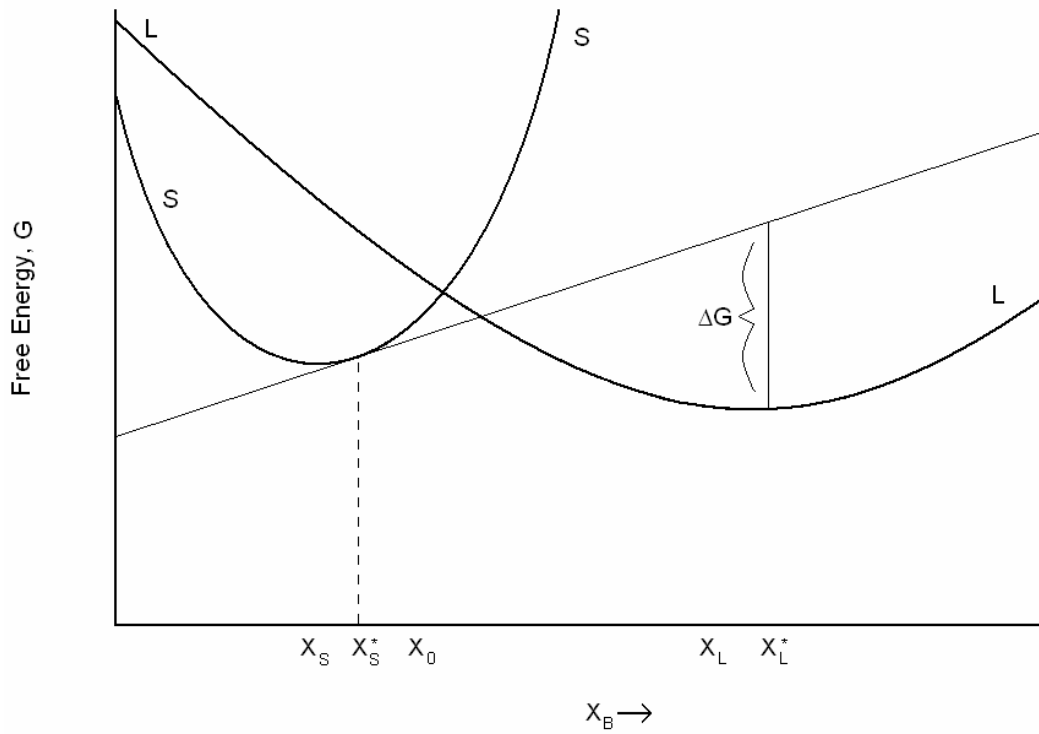


Figure 17 G-X diagram showing the driving force for melting of an alloy. This can be thought of as the "mirror image" of a G-X diagram showing the driving force for solidification. The driving force for melting is the distance between the tangent to the solid concentration and the liquid curve at the liquid concentration.

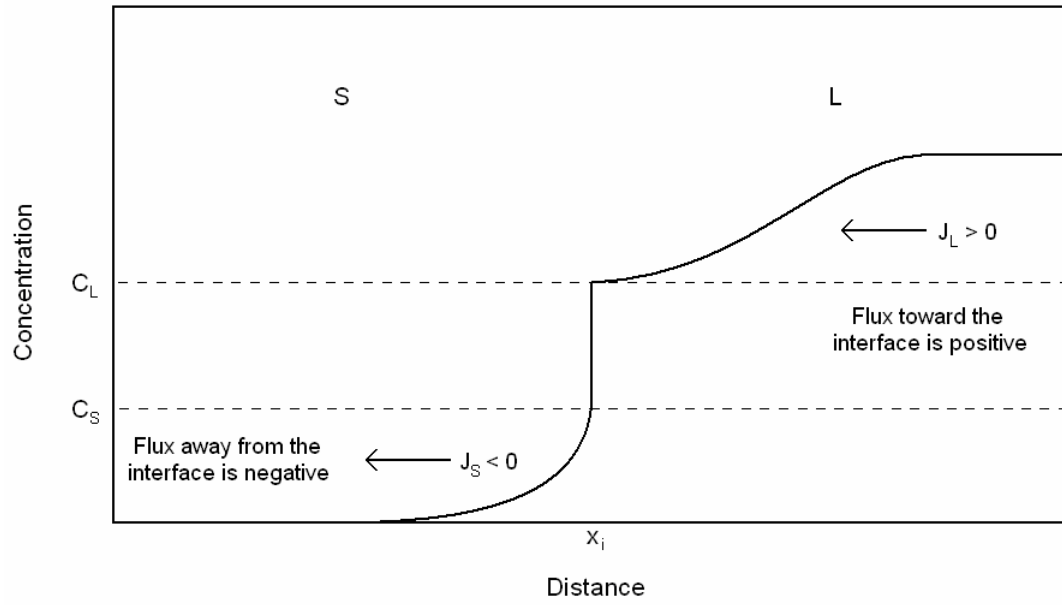


Figure 18 Concentration profile showing the convention for positive and negative flux. Flux is positive when pointing towards the interface.

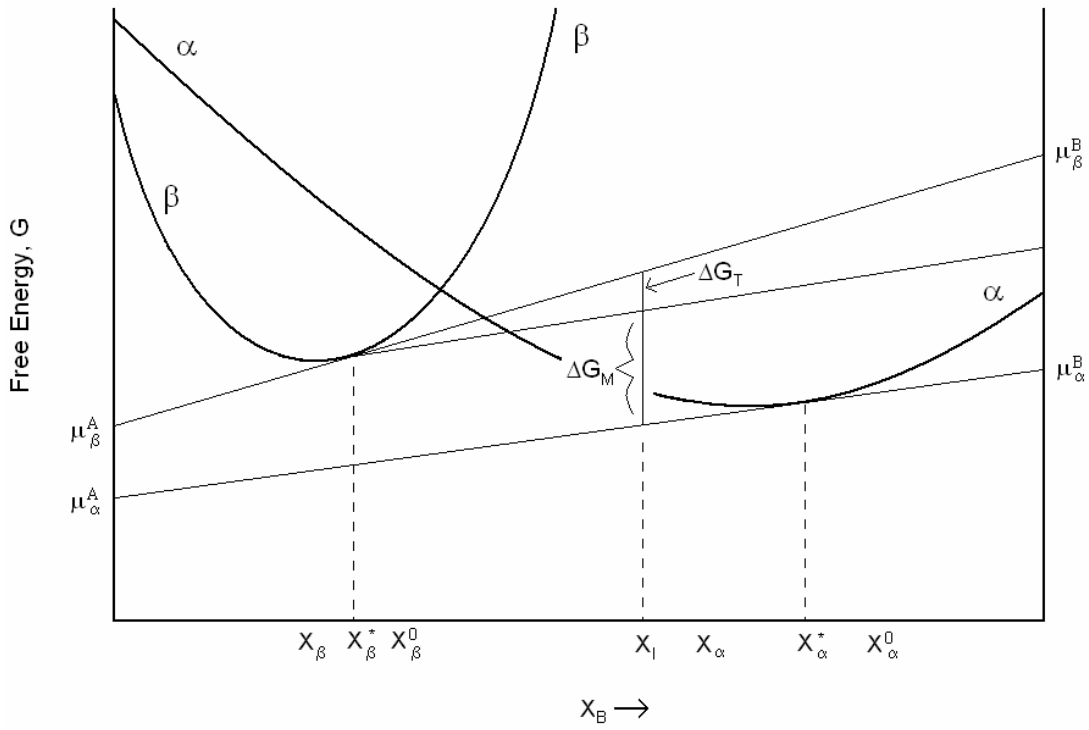


Figure 19 G-X curve showing the graphical representations of chemical potentials and X_I . The driving forces are determined graphically at X_I instead of the concentration of the product phase.

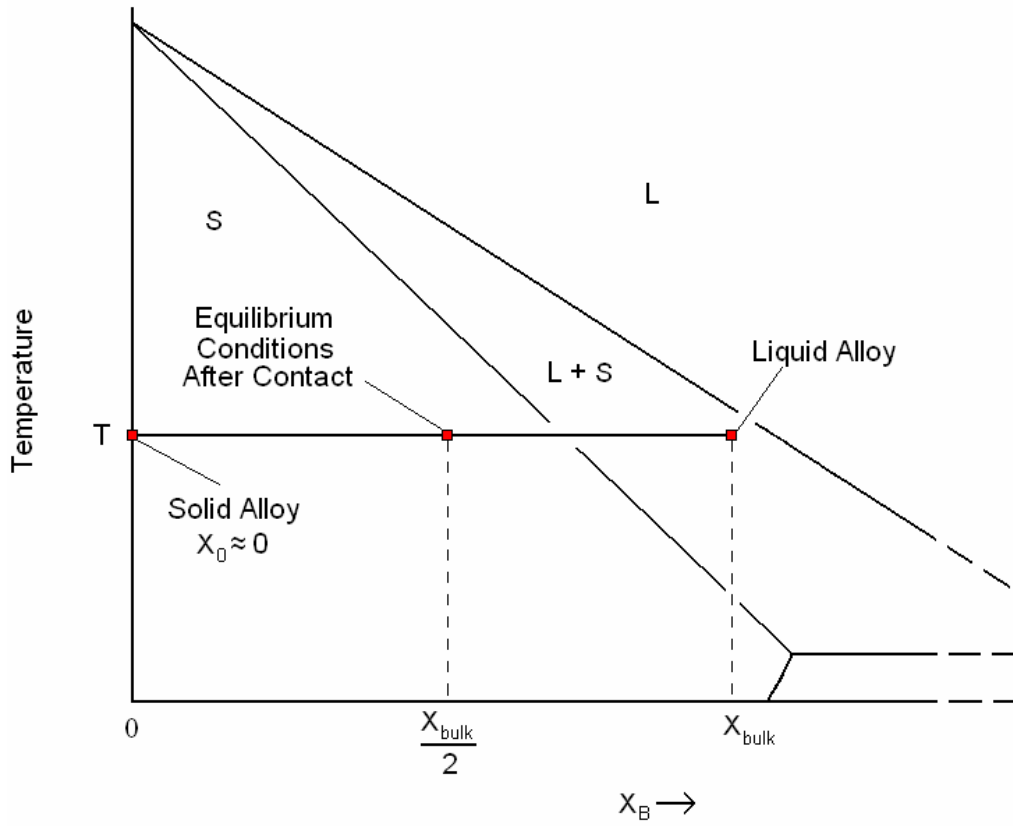


Figure 20 Phase diagram showing the conditions of the initial alloys and the resulting alloy when brought together. The two alloys are the same size and held at a constant temperature.

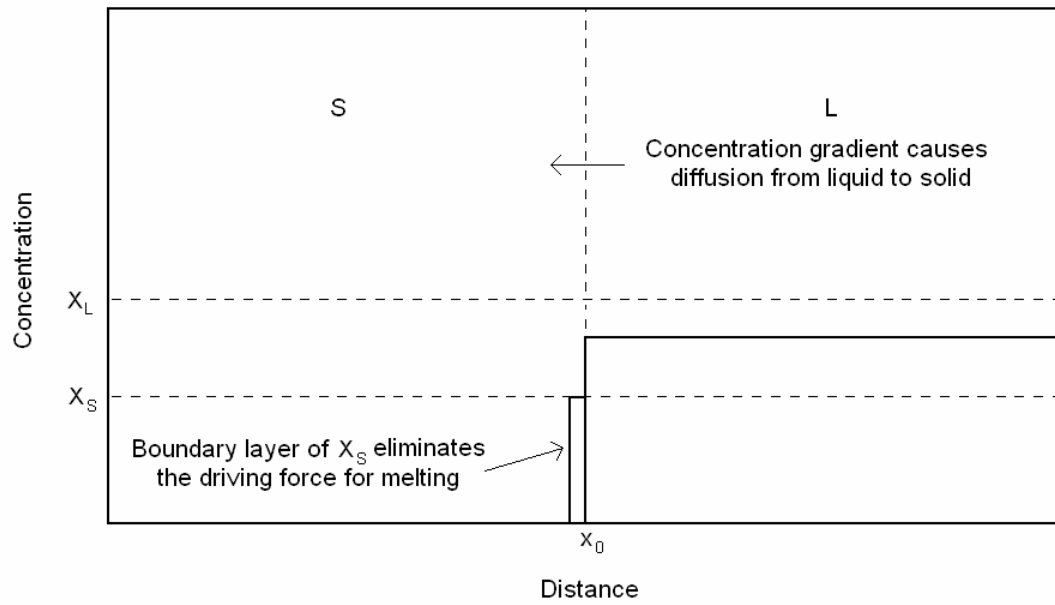


Figure 21 Initial concentration profiles for the alloys in Figure 20. The small diffusion barrier in the solid eliminates the driving force for melting (Figure 10). However, the initial concentration of the solid is still assumed to be close to zero.

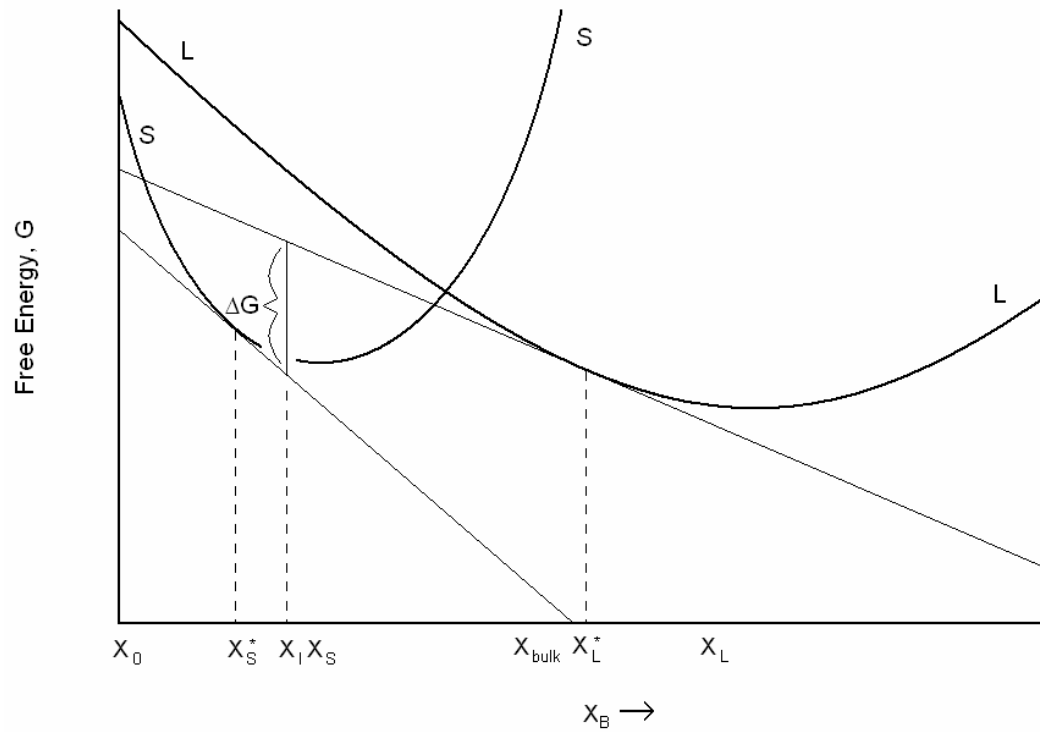


Figure 22 G-X diagram showing the driving force for solidification for the conditions presented in Figure 20. More solute passes across the interface than if the initial solid was not present because the depleted solid is a solute sink, and therefore X_I is greater than X_S^* .

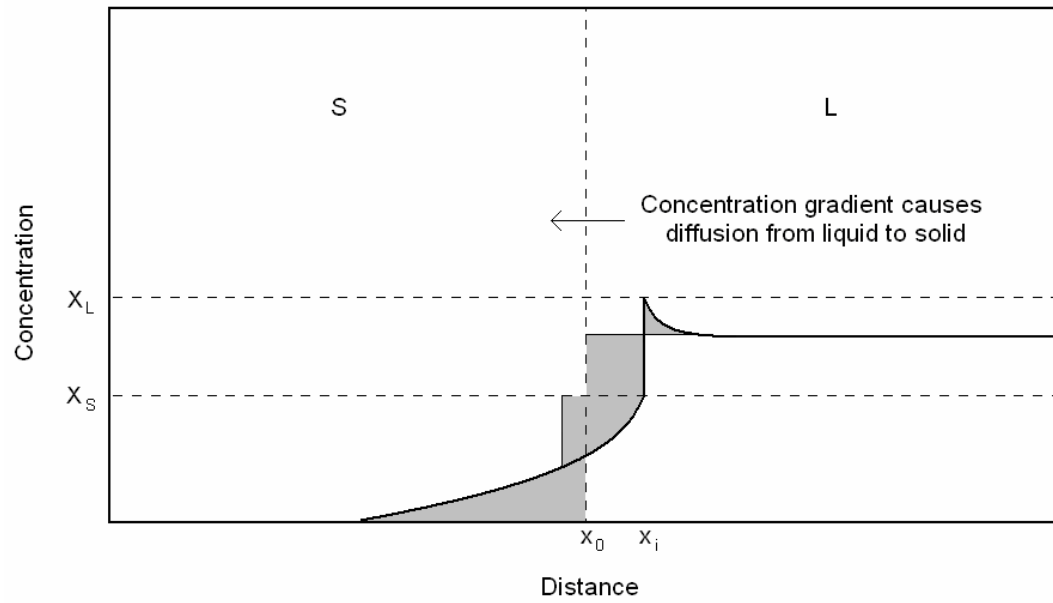


Figure 23 Concentration profile of solidification as a reaction between two phases. The grey regions underneath the profile line equal the grey regions above it at all times.

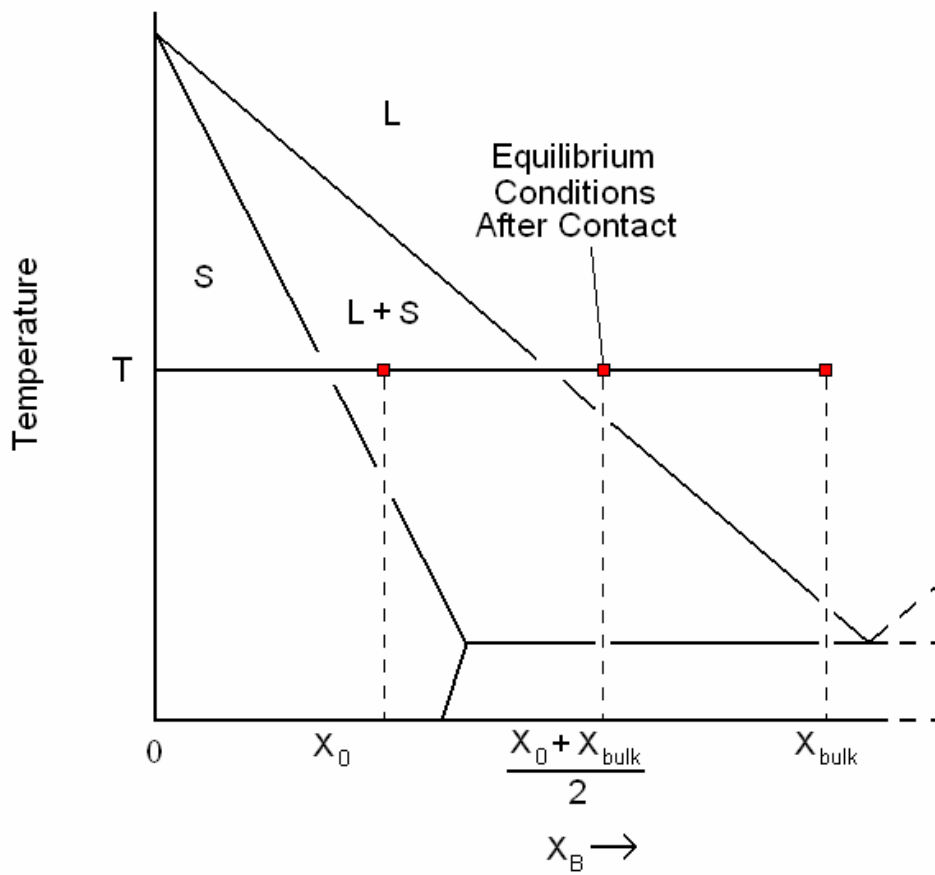


Figure 24 Phase diagram showing the initial conditions of two alloys and the final equilibrium conditions when they are placed in contact. The alloys are kept at a constant temperature.

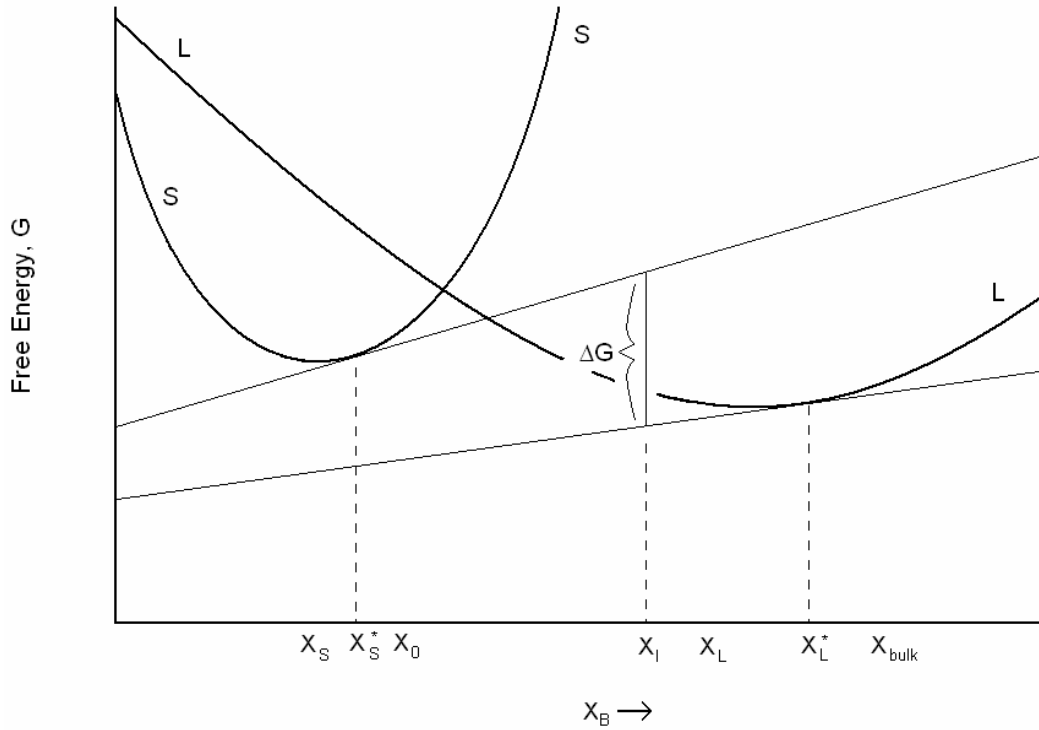


Figure 25 G-X diagram showing the origin of the driving force for melting with the initial conditions shown in Figure 24. Some solute needed for making the phase change from liquid to solid is supplied by the initially present liquid and therefore not as much solute needs to cross the phase boundary and X_I is less than X_L^* .

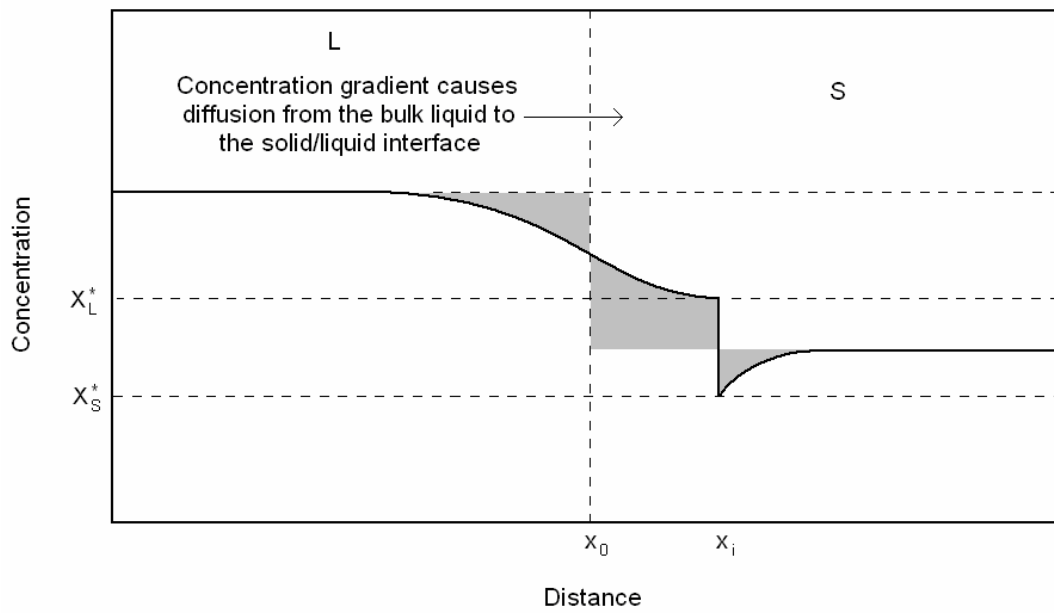


Figure 26 Concentration profile of melting as a reaction between two phases. The grey regions underneath the profile line equal the grey regions above it at all times.

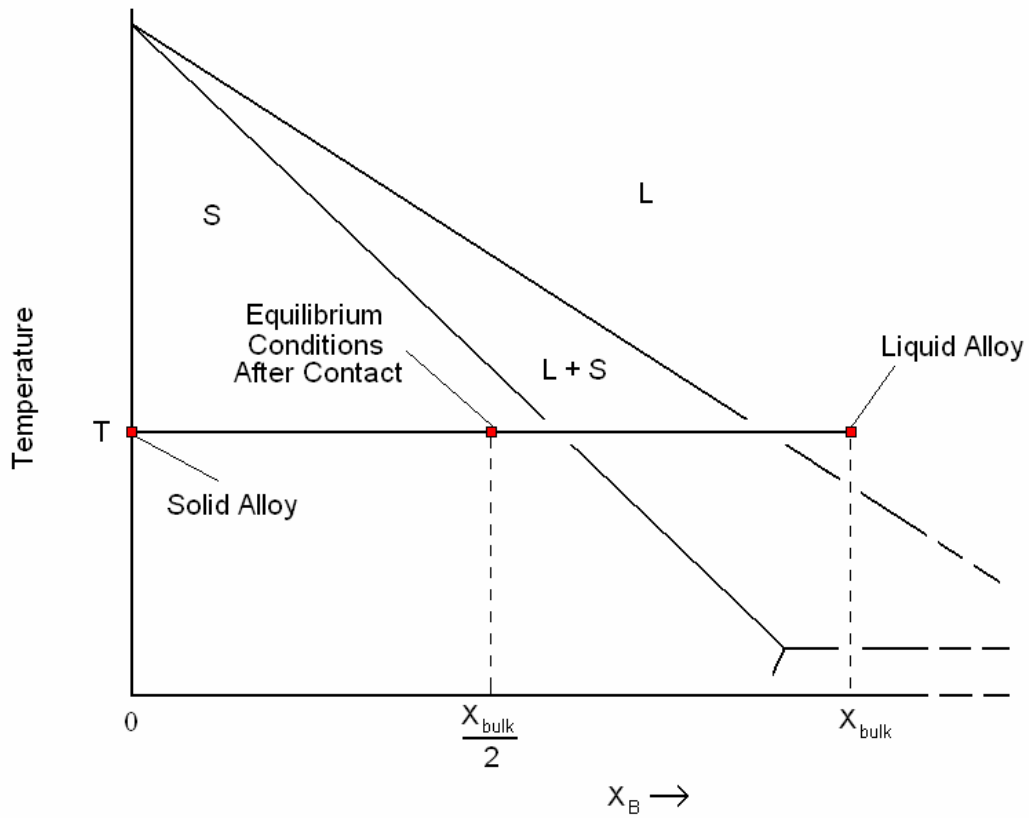


Figure 27 Phase diagram showing the initial conditions of two alloys and the final equilibrium conditions when they are placed in contact. Both of the initially present alloys are in their respective single phase fields. The alloys are kept at a constant temperature.

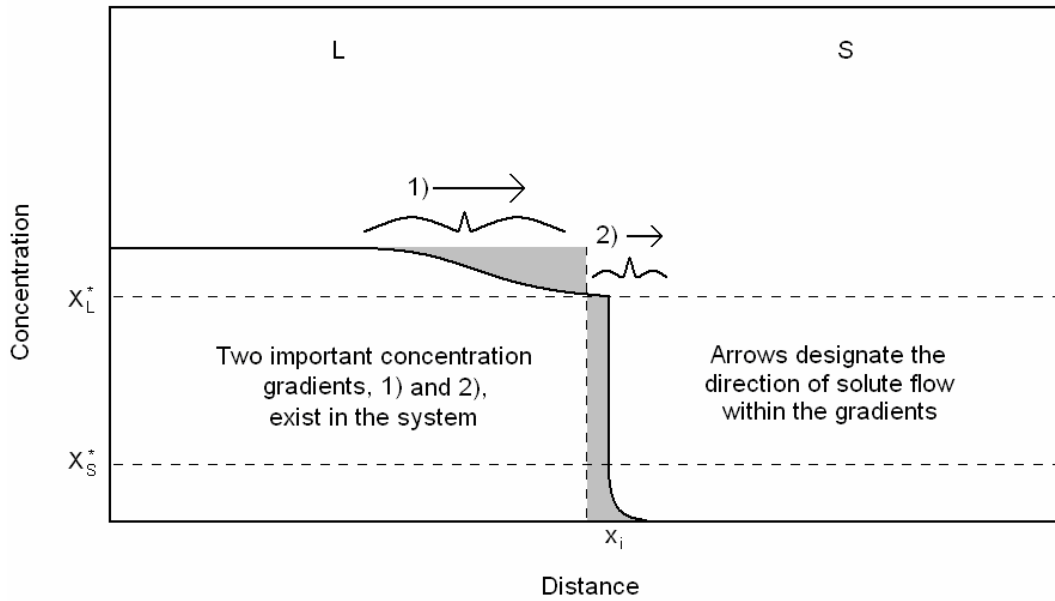


Figure 28 Concentration profile of melting as a reaction between two alloys in their single phase fields. The grey regions underneath the profile line equal the grey regions above it at all times. 1) shows the direction of solute flux due to the concentration gradient in the liquid and 2) shows the direction of solute flux due to the concentration gradient in the solid.

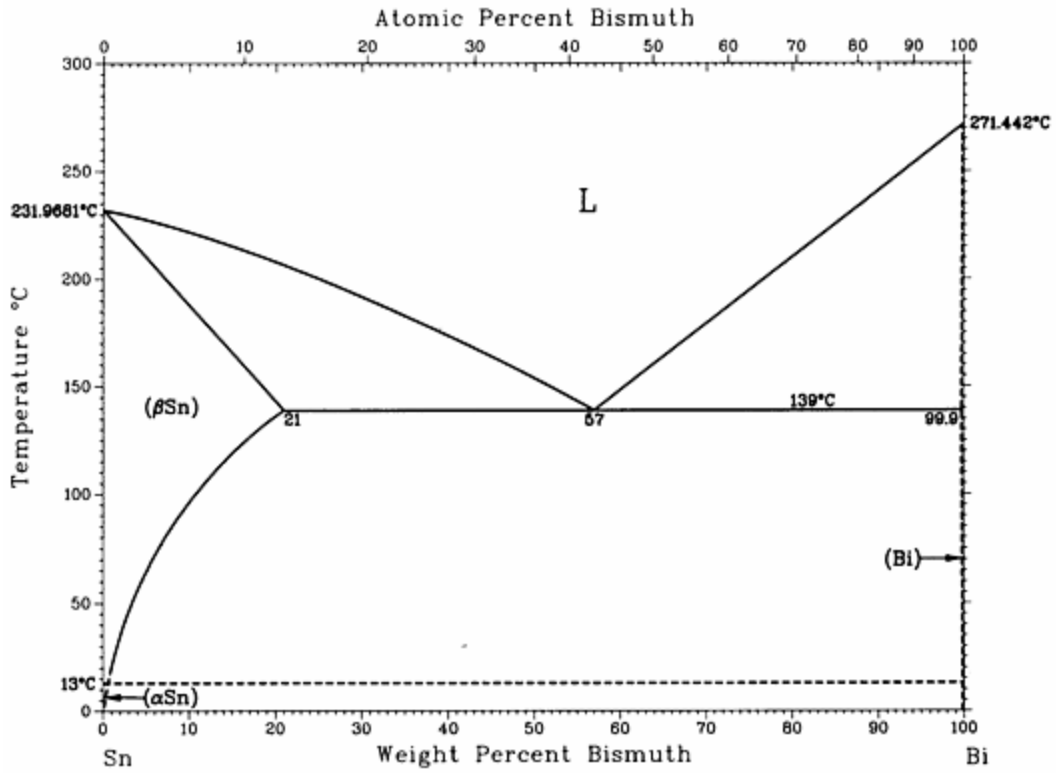


Figure 30 Sn-Bi T-X phase diagram [25].

Table 1 - Properties of Sn, Bi, and the Sn-Bi System

Property	Value	Unit	Source
Sn at. wt.	118.710	g/mol	
Bi at. wt.	208.980	g/mol	
Sn Melting Point	231.9	K	[25]
Bi Melting Point	271.3	K	[25]
Sn Rich C_L at 483K	12.4	at% Bi	[25]
Sn Rich C_L at 448K	27.1	at% Bi	[25]
Sn Rich C_{Lmin} at 483K	0.20	at% Bi	[25]
Sn Rich C_{Lmin} at 448K	0.08	at% Bi	[25]
C_E	42.9	at% Bi	[25]
Sn Enthalpy of melting H_m	7,060	J/(mol)	[30]
Sn Heat Capacity at 483K	29.5	J/(mol-K)	[31]
Sn Heat Capacity at 448K	30.0	J/(mol-K)	[32]
Bi Heat Capacity at 483K	29	J/(mol-K)	[32]
Bi Heat Capacity at 448K	29	J/(mol-K)	[32]
Solid Sn Density	6.14×10^{-5}	mol/mm ³	[33]
Diffusion in the Sn-Bi System			
Q at 42.9at% Bi	18,430	J/mol	[16]
Q at 27.1at% Bi	13,864	J/mol	[16]
Q at 19.5at% Bi	11,565	J/mol	[16]
Q at 12.4at% Bi	11,152	J/mol	[16]
D_0 at 42.9at% Bi	9.83×10^{-4}	cm ² /s	[16]
D_0 at 27.1at% Bi	4.49×10^{-4}	cm ² /s	[16]
D_0 at 19.5at% Bi	3.01×10^{-4}	cm ² /s	[16]
D_0 at 12.4at% Bi	2.89×10^{-4}	cm ² /s	[16]

CHAPTER 3 EXPERIMENTAL APPROACH

The first and only experimental apparatus that the author is aware of for the past investigation of solutal melting of alloys was designed by Rettenmayr et al. [9, 20]. They began by casting two cylinders made from two different alloys. One alloy was a dilute Al-Fe alloy that they claimed behaved like pure aluminum during the melting experiment. The other was an Al-Mg with a liquidus temperature below the melting point of the other alloy. The cylinders were cut in half longitudinally, and one half of each alloy was placed in a furnace crucible such that the rectangular faces were facing each other. A graphite sheet was placed between the halves to prevent physical contact between them. The temperature was raised to a value between the liquidus temperature of the Al-Mg alloy and below the melting point of the Al-Fe alloy. When the temperature stabilized, the graphite was removed and the remelting commenced. Measuring the temperature of the system in different places monitored the migration of the solid-liquid interface. Since the furnace was designed to be adiabatic and adjustments were made to account for lost heat, the temperature change due to the latent heat of fusion could be found. This temperature change could be used to calculate the velocity of the melting interface.

Elements from Rettenmayr's setup were borrowed for the design of the present apparatus. The schematic of the setup is shown in Figure 31. In this design, the metal to be melted is in the form of a long slender cylindrical ingot contained by a glass capillary. The capillary has open ends, and therefore the metal is exposed at the tips. The liquid alloy used as the melting agent is contained in a glass crucible topped with a graphite plug. The capillaries enter the crucible through holes drilled into the plug and connect with the liquid alloy inside the crucible. The remelting occurs at the opening of the capillary and continues upwards deeper into the capillary as time passes.

The process is observed by running many experiments at the same conditions and freezing them at different points during the process. By measuring the frozen position of the interface at different times, a clear trend for the position and velocity against time emerges.

In the next section, the equipment and sample preparation are described in detail. Then, the procedural steps are presented. Subsequently, the steps taken to run an experiment are detailed.

Equipment

Furnace

Experiments were performed in a controlled 31.5cm Marshall tubular shunt furnace with a 3cm opening either end. In order to adjust the position of the crucible in the furnace, a removable sectioned pedestal was produced. The resistance between the two shunts at opposite ends was 7.8Ω . The pedestal had six cylindrical sections, five of which were refractory brick, and the other one graphite. Of the five refractory brick sections, four were 2.8cm high and the other one was 4.3cm high. In addition to adjusting the height of the crucible for the experiment, these pedestal sections also prevented heat from flowing out of the bottom of the furnace. The crucible rested on the 0.5cm high graphite section that allowed heat to flow into the crucible from underneath. The crucible and the samples were all loaded through the top hole of the furnace. Therefore, several layers insulating fabric were fashioned in order to insulate the opening at the top of the furnace through which the capillaries and thermocouples protruded. Holes for the capillaries, thermocouples, and the ceramic rod were punched in the fabric. The pieces of fabric were slid over the protrusions and down to the surface of the furnace to cover the top opening.

Temperature Monitors

Two K-type thermocouples were used for all temperature measurements and controls. They were inserted into the melt through holes in the graphite cap immediately after the capillaries were submerged. The thermocouple sheathes were marked at a points outside of the furnace so that they could be positioned at the correct height. One was positioned at the height of the exposed tip of the capillary which was 1.5cm from the bottom of the crucible. This was termed “Low Melt”. The other was positioned 1cm above the Low Melt and termed “High Melt” 32. This position was higher than the liquid ever penetrated during any experiment, so the temperature during the entire remelting process can be assumed to be between the Low Melt and High Melt values. The difference was typically less than 0.4°C (see *Results*). The thermocouples were held in place by a claw attached to a laboratory stand.

Power Source and Controller

The furnace was connected to a Eurotherm 808 electronic controller within a Mellen case and motherboard. The controller was powered by a variable auto-transformer (variac) from Staco Energy Products Co. The variac was connected to the shunts at opposite ends of the furnace with the positive node at the top and the negative at the bottom. The controller monitored the furnace temperature with a K-type thermocouple. The thermocouple was inserted though the top of the furnace with the tip located between the inner furnace wall and the crucible 14cm from the top opening. This was the hottest section in the furnace. The temperature of the melt near the melting reaction was usually ~5°C lower than the monitor temperature. The Variac was set to 40% of 120V

Data Acquisition

Temperature and voltage data were acquired by a Hewlett Packard 34970A Data Acquisition/Switch Unit. The unit was capable of monitoring and logging data on 22 channels at

once, however the most channels used in any experiment was three (two temperature and one voltage). The acquisition rate was one measurement per channel per second. During the experiments, the parameters were monitored using Agilent/Benchlink software. The data were exported as tab-delimited text files. Microsoft Excel was used to graph and analyze the data.

Crucible and Sn-Bi Charge Preparation

Borosilicate sample bottles from the Lab Depot were used as the crucibles that contained the Sn-Bi melt during the experiments. The tip of the bottles were fashioned with threads and a plastic cap, below which the body of the bottle was a uniform tube with OD = 2.5cm and ID = 2.7cm (see Figure 33). The bottoms of the bottles were flat and circular. The tops were removed with a diamond saw so that only the uniform body and the flat bottom remained. After they were cut, the rim was sanded with 60 grit SiC sandpaper in order to provide a smooth surface that could be sealed. The crucibles were rinsed with acetone to remove any oily residue. The acetone was decanted and the crucibles were heated with a butane torch and for ~15 seconds to evaporate any remaining water or acetone left inside them. The crucibles were flushed with UHP argon three times while they were being heated.

Raw 99.9% pure Sn rods and 99.99% pure Bi needles were obtained from Aesar, a Johnson Matthey Company. Verhoeven observed that experimental results on the stability of melting interfaces in the Sn-Bi system were identical for 99.9999% purity and 99.99% purity graded Sn [17]. The relative weights of the Sn and Bi needed for the Sn-Bi alloy were calculated from the chosen atomic composition. The weight of each element was measured on an electronic balance with a resolution of 0.001g. The charges were placed in a prepared borosilicate crucible (see above), flushed with argon to avoid excessive oxidation, and covered with graphite plug. The graphite plug had holes drilled in them (for the glass capillaries), but they were plugged

when not in use. The charges were brought to 315°C in the furnace. After they melted, they were and homogenized for 3 hours. The melt was stirred intermittently with a glass rod to ensure complete mixing. At this point the melt was ready to use for experimentation.

It was desired to fill the crucible with as much of the alloy as possible so that it could resist temperature changes from dipping the capillaries, latent heat of melting, and other uncontrollable factors that affect the heat content. The total weights of the charges were ~200g, which filled the crucible to a surface height of ~5cm as a liquid. This was close to the maximum amount that would fit in the crucible after the graphite cap was inserted.

Sn Capillary Ingot Preparation

Both sizes of borosilicate capillaries, OD 2mm and ID 1mm, OD 4mm and ID 2mm, were ordered from Technical Glass Products, a company owned by GE (see Figure 33). They were cut to length, usually 20cm, and the ends were sanded with 120 grit sandpaper. Acetone was introduced into the capillary with a fine-tipped wash-bottle. The capillary was also tilted from side to side with the solvent in it to cleanse the entire inner surface. After rinsing for ~30 seconds, the acetone was decanted. The capillaries were then held in a butane flame with tongs in order to vaporize the remaining moisture and acetone. One end of the capillary was held in front of the flame and then was slowly pulled through the flame to the other end. The capillary was flushed with UHP argon twice during the process.

Sn was placed in a crucible and heated on a hot plate to ~300°C. A vacuum pump was used to fill the capillaries. The vacuum pump was attached to a rubber hose fit with a valve. A hole was drilled in a Neoprene stopper with a 1mm drill bit and plugged into the open end of the rubber hose. The empty capillaries were pushed through the hole in the stopper until they just came out the other side. This ensured a good seal between the capillary and the plug. The valve

between the pump and the capillary was closed and the pump was turned on. The capillary, stuck in the plug, was heated by a butane torch for ~30 seconds before it was filled. This was done in order to prevent Sn from solidifying on the capillary walls while it was still being sucked into the capillary. The free end of the capillary was quickly placed into the melt through a hole in the graphite cap. The valve was quickly opened and then quickly closed when the tube was full. After the valve was open, the capillary was filled in about 0.5s. It was then removed from the melt and from the stopper. Any excess metal coming out of the top was clipped off. The quality of the ingots was generally good with very few, if any, visible bubbles on the surface. After being cast, the end of the ingot to be melted was sanded. The tips were usually not cast well, and so at first, the tip to be used was ground with 120 grit paper until the high quality section of the cast was reached. The section removed was usually about 0.5cm.

Next, the edges of the capillary near the tip were tapered by grinding them on 120 grit paper. The resulting shape is shown in Figure 34. Finally, the tip was sanded again with 240 grit paper to achieve a smoother surface. The purpose of the tapering is to remove the surface area of the glass surrounding the exposed metal. This will increase the quality of the contact between the melt and the metal in the capillaries. The ingot, at this point ready for the experiment, was placed in a desiccator until it was used.

Procedure

The goal of the setup and the procedure is to impose known conditions on the melting interface so that the effects of certain variables can be explored. The variables to be controlled in this setup are:

- (1) Temperature of the liquid and solid.
- (2) Composition of the liquid in the crucible.

The temperature is intended to be fixed at a certain value for the entire region where there melting takes place. Composition gradients will arise in the capillary as solutal melting proceeds, but the initial composition of the liquid in the crucible should be fixed and homogeneous.

The experimental schedule can be found below, followed by an explanation of the steps:

- (1) Casting and preparing the pure Sn capillaries.
- (2) Weighing out a Sn-Bi charge to be melted in the crucible.
- (3) Flushing the crucible and furnace with Argon, placing the crucible in the furnace, and homogenizing the charge.
- (4) Securing the five capillaries within the graphite cap, insulating the tips with Teflon, and connecting the Teflon pieces to the ceramic rod (see below).
- (5) Inserting the capillaries with the open ends insulated by Teflon tape, and inserting the thermocouples.
- (6) After waiting for temperature to stabilize, starting the data logger and removing the Teflon with the ceramic rod to allow remelting to begin. Also, checking for contact between the capillaries and the melt with a multimeter.
- (7) Removing the capillary/s from the melt at the predetermined times, and quickly quenching them to preserve the interface position.

Steps (1) and (2) are described in the *Equipment* section. After the experimental materials were ready, the furnace was turned on, the desired temperature was set in the controller, and the chamber was flushed with argon. The Sn-Bi charge to be melted was placed inside on the pedestal. Homogenization of the Sn-Bi charge for step (3) is described in the *Equipment* section as well.

Step (4) is necessary in order to control the initiation of the melting process. As soon as the solid tin and the liquid alloy come into contact, unrestrained melting occurs. However, the moment that the capillaries were dipped into the melt, the temperature dropped several degrees. This temperature drop can considerably affect the rate of remelting. Therefore, a method was developed to insulate the liquid and solid metals from each other while submerging the capillaries, thus allowing the temperature to stabilize before remelting could occur. First, the outer walls of the capillaries were wrapped with Teflon at a certain point. The Teflon acted as a stopper, preventing them from sliding through the hole in the cap beyond this wrapped section (see Figure 32). The point was chosen such that the tips of the capillaries would hang ~1.5cm above the crucible floor. The capillaries were then slid through the holes in the graphite cap (which rested on its side on a workbench). Next, a thin piece of Teflon tape was pulled over the exposed end of each capillary to insulate the metals. Each piece of tape was also connected to a hook at the end of a ceramic rod that that was slid through a hole in the center of the graphite plug (see Figure 35). The rod was long enough to be manipulated from outside the furnace. The hook was wrapped with Teflon to prevent the metal from dissolving. After this apparatus was constructed, the capillaries were ready to be submerged in the melt without danger of being melted before the experiment started. After removing the Teflon with the rod, the temperature was still perturbed but the magnitude was very small (~0.1-0.2°C) and it quickly re-stabilized (see *Results*).

The viability of Teflon as an insulator was tested by submerging an insulated capillary into the melt overnight. The next day, the scratches on the exposed metal were still visible, and therefore no melting took place. Teflon was also found to be inert towards the metals used in this study. Its properties can be found at DuPont's website [33].

The graphite cap holding the capillaries and the rod was then inserted into the crucible within the furnace as noted in (5). This was done with a pair of metal pincers that gripped the cap by the thermocouple holes (Figure 35). After the cap was secure, the thermocouples were inserted into the melt. The position of the thermocouples was determined by marking the position on the thermocouple sheath that corresponded to the top of the furnace when the thermocouples were positioned properly.

The temperature is perturbed quite a bit in step (5), so time was allowed to pass, usually about thirty minutes, before the Teflon was removed in step (6). The data logger was started 5 minutes prior to doing so. After removing the Teflon, the rod was left at the bottom of the crucible for the duration of the experiment so that the temperature was not disturbed. After removal, a multimeter set to the buzz function was used to check whether or not good contact was made between the pure Sn and the Sn-Bi melt. The Sn in the open capillary tips protruding from the furnace was touched with the multimeter leads, and if both capillaries had good contact, the multimeter would buzz. If some capillaries didn't touch the melt initially, the capillary was slightly agitated to bring them together, or the experiment was aborted and restarted. The contact for the samples was checked a second time just before they were removed from the melt in the next step. If they were not in contact, the sample was considered to be corrupt and was not logged.

In (7), the capillaries are simply removed from the melt and water-quenched as quickly as possible to preserve the melting interface position. The capillaries were removed at a 10, 20, 30, 40, or 50 minute time interval. After quenching, the samples were ready for analysis.

Analysis

Metallography

The goal of the metallography was to expose the remelting interface and the solidification morphology of the remelted zone. After a capillary was removed from the melt and quenched, a 1cm section of end containing the remelted metal was removed with a diamond saw. None of the samples ever had remelted zones protruding more than 0.6cm from the tip of the capillary. The samples were set with the metal still within the glass capillary and with the outer wall of the capillary on the surface to be ground. The samples were set with a Buehler Sample-Kwick Fast Cure Acrylic Kit. This acrylic was chosen because the temperature while curing did not rise above 50°C. After mixing the acrylic, it was poured into the mold very carefully so that it did not move the samples as it flowed. After curing, the samples were polished on a polishing wheel using a constant and low flow of water as a lubricant. The polishing began with planer grinding on 60 grit SiC sandpaper until the center of the capillary was reached. Since Sn is a soft metal, only slight positive pressure was applied to the sample during polishing in order to avoid grain deformation and embedded particles. Polishing at each step began in a direction perpendicular to the previous step and continued for twice as long as the time it took for the scratches from the previous step to disappear from sight. The successively lower grit sizes of SiC paper used were 60, 240, 400, 600, and 800 by Beuhler polishing papers. Polishing with the 600 and 800 grit papers were carried out on a different wheel than the others to avoid contamination. At this point, the samples were polished by hand on a low-knap cloth impregnated with 5.0 μ m alumina particles for ~15 minutes. The concentration of particles was high in order to achieve a high cutting rate. This reduces the amount of time needed to polish the sample and reduces the number of embedded particles in the Sn section of the sample. After this polishing step, the remelting interface and dendrite orientation were clearly visible, so no etching was required.

Microscopy

The measurements of the melted zones were carried out with an optical microscope and SPOT digital imaging software. The eyepiece and objective lens magnifications were input, and SPOT converted pixels on the digital image to distances. Composite images of the samples were made by taking several pictures at high magnifications and overlapping the images based on landmarks in the microstructure. The length of the remelted zone was measured by finding the distance between the melting interface and the bottom of the glass capillary (the initial interface). Several photographs were taken at 200X between the two endpoints in the same fashion as for creating a composite image. Measurements were taken from each image along the capillary wall. Landmarks on the micrographs were used as endpoints for the distance measurements. Since the images overlapped, the same landmarks were used as endpoints in neighboring images. The distance of penetration for each sample was therefore the total of the distances measured on each photo of the composite image.

SEM

SEM analysis was carried out by the author on a JEOL JSM 6400 at the MAIC facilities at the University of Florida's Materials Science and Engineering department. Since the polished samples were mounted in a non-conductive epoxy, they had to be grounded in order to avoid surface charging effects. First, carbon paint was used to cover the non-conductive surface that would be exposed to the electron beam. A small section of the exposed metal was covered with carbon paint as well to bring the sample and the paint into electric contact. Then, the paint was used to create a conductive path from the carbon covered surface to the conductive sample mount that is placed into the SEM. Magnification for the images collected ranged from 200X to 1000X. Images were collected in BSE mode and SE mode. The probe size for EDX analysis was $\sim 2\mu\text{m}$. EDX was used for qualitative data only.

EPMA

EPMA was carried out in a JEOL SUPERPROBE 733 device at the MAIC facilities at the University of Florida's Materials Science and Engineering department. Analysis was carried out by Mr. Wayne Acree. The size of the probe was 1-2 μm . Precision of the measurements were within on hundredth of a percent (wt%). An arbitrary point near the interface region (see

Figure 57) was taken as the interface location for the scan. From this point, periodic measurements were taken in directions perpendicular to the interface and further into the unmelted and previously melted regions, respectively (see Figure 57). Six measurements were taken in either direction. The distance between each measurement was $10\mu\text{m}$.

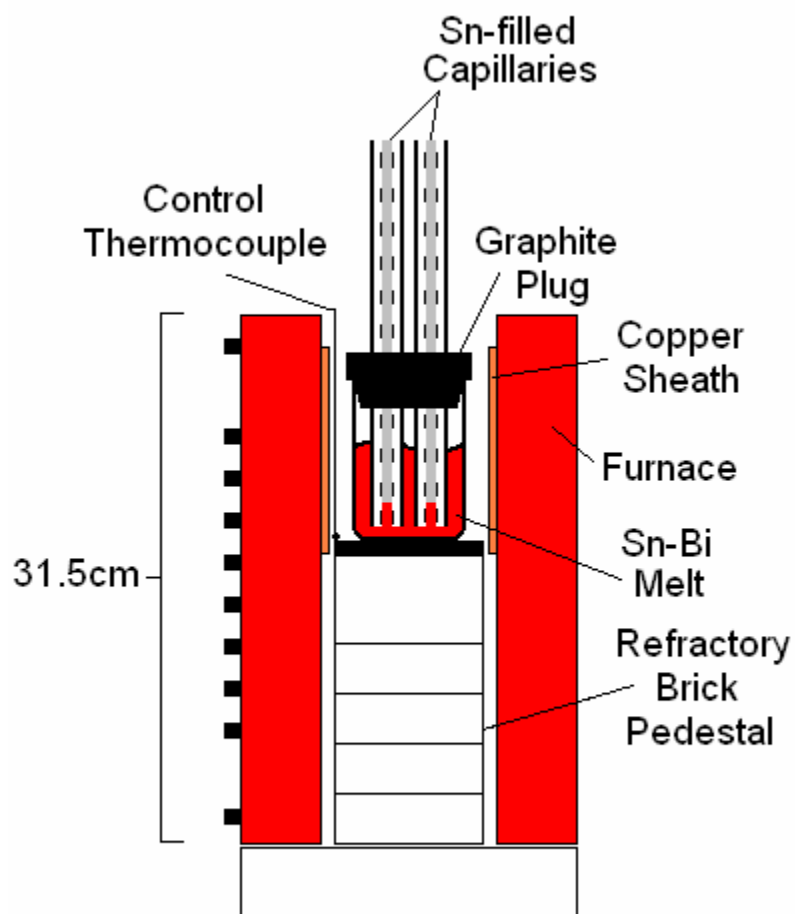


Figure 31 General experimental setup. The crucible sits on a refractory-brick pedestal and is held at a constant temperature by the furnace. The copper sheath helps to spread the head more evenly across the heated zone. The capillaries enter the crucible vertically via holes drilled in the graphite cap.

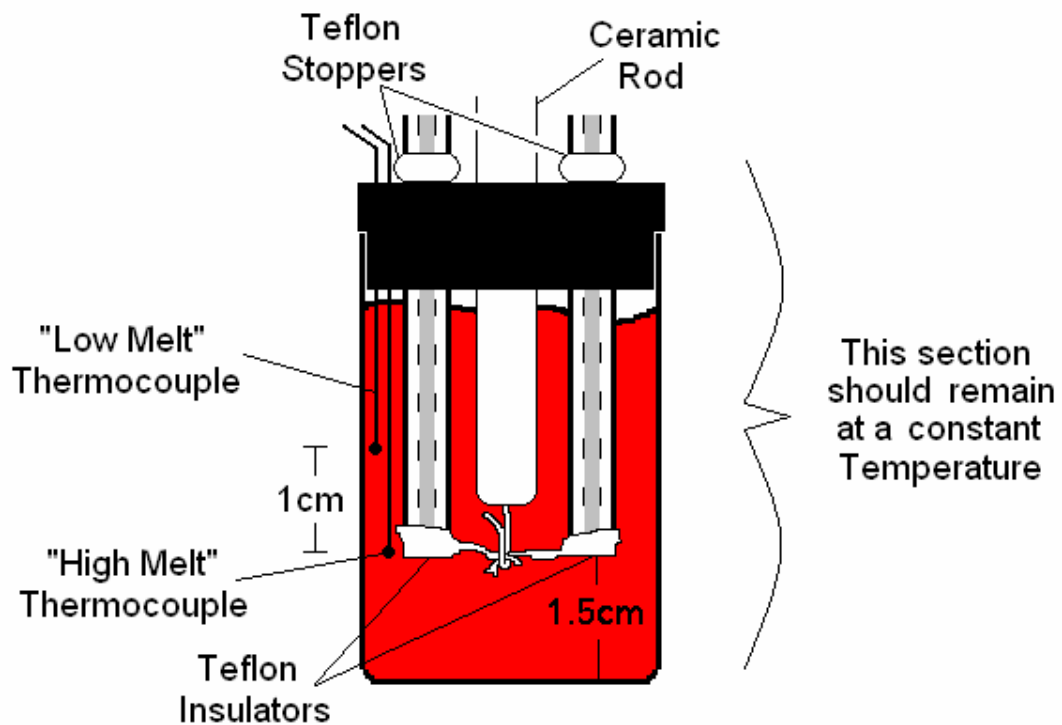


Figure 32 Close-up diagram of the crucible. The Teflon wrapped around the shafts above the cap supports the capillaries. Also, Teflon insulated the Sn in the capillary from the melt until it is removed by the ceramic rod. The thermocouples record the temperature gradient that the melting interface incurs as it moves up the capillary.

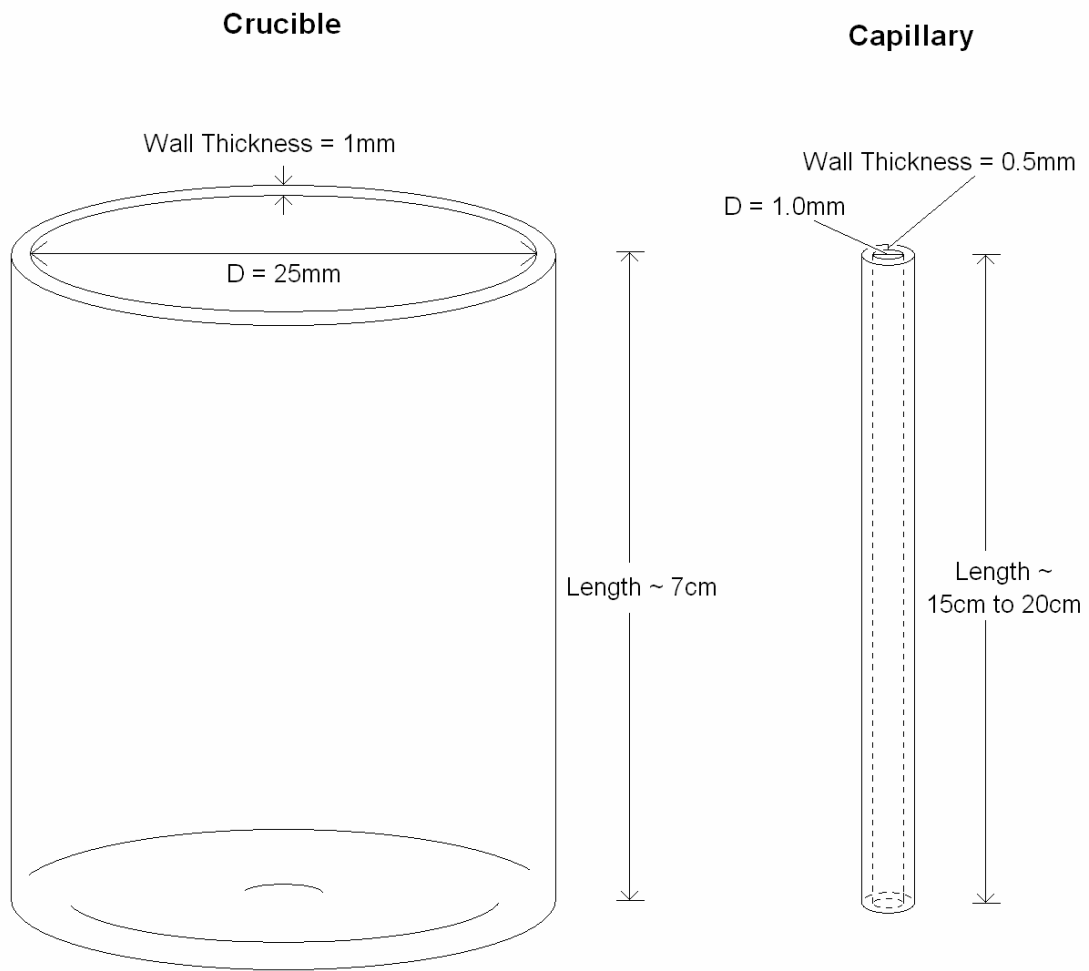


Figure 33 Crucible and capillary dimensions.

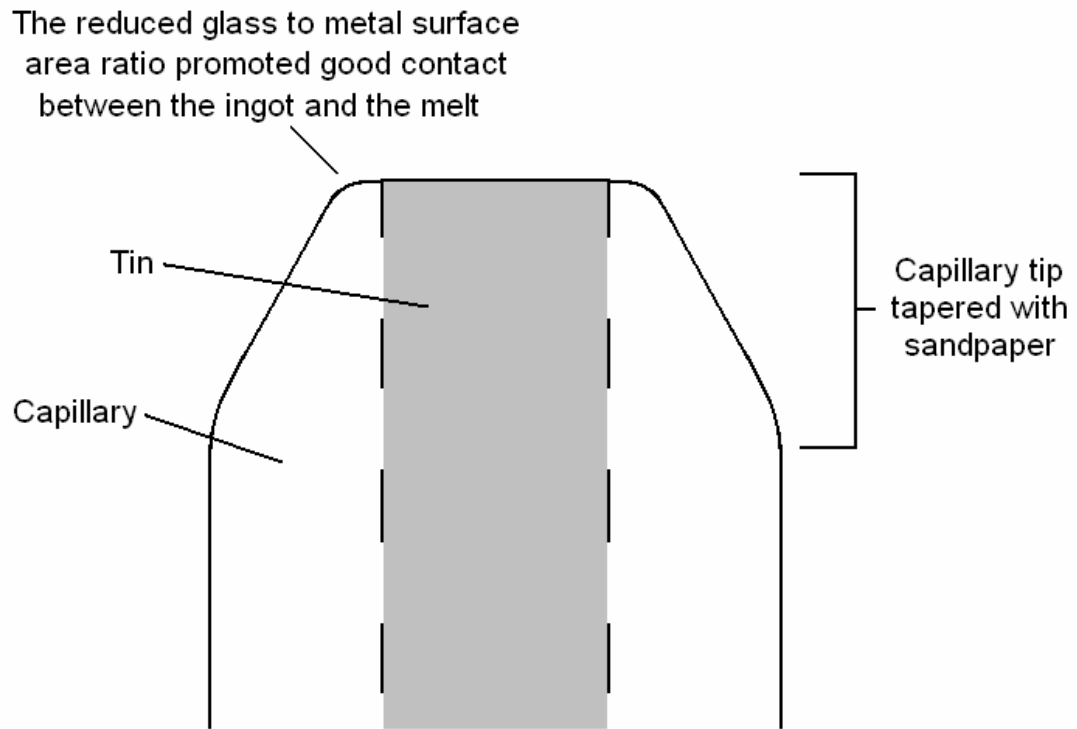


Figure 34 Schematic of the tapered capillary tip.

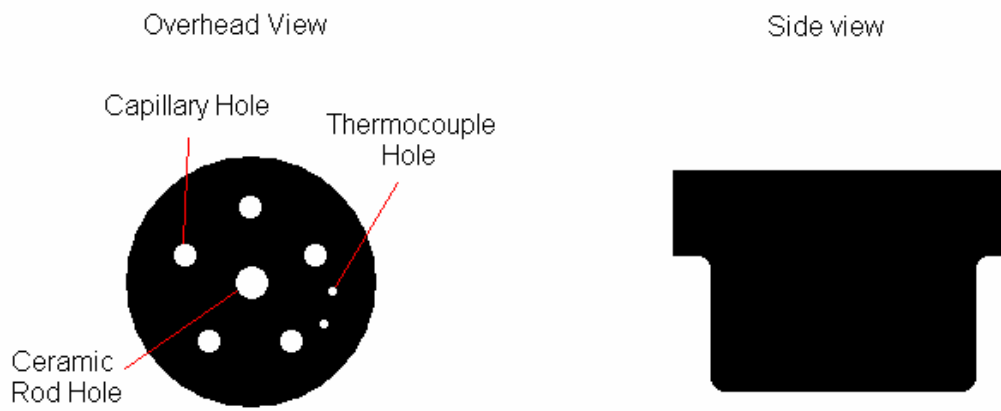


Figure 35 Graphite cap schematic and hole layout.

CHAPTER 4 RESULTS

Sample Labeling Conventions

The samples are labeled with four fields separated by hyphens. The fields are filled in as follows:

- The 1st field is preceded by a C and designates composition of the melt. The numbers are the tens, ones, and tenths places of the atomic weight percent.
- The 2nd field, preceded by T, designates the target temperature for the experiment. The actual average temperature for a group of samples usually deviated from this temperature by several hundredths or tenths of a degree. This deviation is accounted for in the analysis. The numbers are the hundreds, tens, and ones places of the temperature in degrees Celsius.
- The 3rd field designates the number of minutes that the sample was kept in the melt.
- The 4th field is simply an identifier to differentiate between samples that were run at the same three conditions mentioned prior. This field is a number.

Hence, a sample labeled C195-T210-40-3 refers to sample #3 that was dipped into a melt of composition 19.5at% Bi at approximately 210°C for 40 minutes. C195-T210-40 refers to all samples run at these conditions. Likewise, C195-T210 refers the group of samples run at the noted conditions for all durations investigated.

Since the Sn capillaries were always prepared with the same concentration, pure, their composition is not noted in the labeling system although it could affect the results. The conditions noted in the labeling system that were explored in this study are marked on the Sn-Bi diagram in Figure 36.

Micrographs

A typical Micrograph of the melting interface is shown in Figure 37. The smooth region with grain boundaries is pure Sn. The black particles shown in the Sn region are alumina from the polishing step that became embedded in the soft Sn matrix. The eutectic microstructure resulted when the liquid was quenched at the end of the experiment. In the micrograph one can note the location of the melting interface (the reference point for measuring the remelted distance), the region of planer solidification, and the onset of dendritic solidification. The length of the planer solidification region was larger at higher temperatures, yet did not seem to be dependent on the concentration of the liquid. For most samples, the shape of the interface was planer. However, some exhibited interface curvature and, in two cases, melting perturbations that protruded into the Sn matrix.

Before the experiment begins, the pure Sn ingot is entirely the BCT_A5 Sn phase. The flat circular cross section comes into contact with the liquid at the opening of the glass capillary. Melting initiates in a fashion that can be thought of as a “nucleation and growth” process [9]. The melting begins at one spot on the contact surface between the solid and liquid and then spreads over the entire surface. This manifests in the velocity profile as a sharp increase to the maximum value and then a gradual decrease. Before the metals can react, an oxide layer must be dissolved from the solid metal surface. During this incubation period, the velocity is zero. The moment the metals touch, the melting interface nucleates and grows and the velocity sharply rises. When the melting interface reaches the extent of the entire contact area, the velocity levels off and then slowly begins to decrease. Rettenmayr reported an incubation period of 40-50s from the moment of contact to the realization of the maximum velocity. In Rettenmayr’s experiments, however, the area of the interface was $\sim 25\text{cm}^2$, whereas in the present work, the

contact area for each ingot is only 0.00785cm^2 , about three orders of magnitude smaller.

Therefore the incubation period in these experiments may be much smaller. Melting proceeded, in most cases, with a planer interface until quenching.

During the first moments of the quench, planer solidification occurred for approximately $5\text{-}20\mu\text{m}$. The length of this region appeared to depend on the temperature of the melting reaction. Bismuth was rejected from the Sn as the Sn-rich BCT_A5 phase was formed. Afterwards, dendritic solidification dominated as the liquid segregated to form a 2-phase eutectic microstructure. In the eutectic section of the micrographs, the BCT_A5 phase (Sn rich) is lighter, and the Tetragonal_A7 phase (Bi rich) is the darker phase.

In some cases, the liquid from the melted Sn had evacuated the capillary. It was assumed that this happened as the capillary was being pulled from the melt because the contact between the capillaries and the melt was checked just before the capillaries were pulled (see step (6) in *Procedure* in the *Experimental* section) the results for samples under the same conditions regardless of whether the melted metal had been evacuated.

The uncertainty for the distance measurements is on the order of ten microns and stems from the error in choosing the same endpoints for distance measurements between photographs (see *Microscopy* in the *Experimental* section).

SEM Images

Figures 50 through 53 display typical SEM images of the interface between the material that melted and the material that remained solid during the experiments. Figures 54 through 56 show the results of EDX scans on various features in the images. The sample analyzed in these photos and EDX scans was melted for 40 minutes at 210°C with a reservoir composition of 19.5at% Bi. Figures 50 and 52 are SE images taken at 200X and 1000X, respectively. Figures

51 and 53 are BSE images of the same areas shown in Figures 50 and 52, respectively. The images According to the EDX data in figures 54 and 55, the darker areas on the images are the Sn-rich matrix, and the brighter spots are the Bi-rich matrix. EDX also returned results for C, O, and N in the sample. The O and N are most likely contaminants introduced by exposing the sample to the atmosphere. The C may be present due to the C paint used to electrically ground the sample. The contrast between the phases is clearer in the BSE images than the SE images

The vicinity of the interface is clear in the images taken at 200X, however, its precise location is not visible. It may appear that the interface line may be drawn to connect the end points of the Bi phase precipitates, but in fact, the interface lays several microns further into the pure Sn matrix. A small amount of planer solidification occurred before the dendritic or eutectic solidification took place; hence a small area of Sn-rich matrix precedes the formation of Bi-rich precipitates.

EDX analysis of a black impurity particle, present in many of the micrographs, returned the energy spectrum shown in Figure 56. The scan showed characteristic peaks for O, C, Si, and Al. These elements are probably artifacts from polishing with SiC and Al₂O₃ particles.

EPMA

The Data from the electron probe micro-analysis are plotted in Figure 57. The data are taken from a sample that was run at 200°C with a reservoir composition of 19.5at% Bi. The y-axis is positioned at the approximate location of the interface. The exact position of the interface is not clear from images or the concentration profiles. The left side of the chart shows the measurements in the section of the sample that remained solid during the experiment, while the left side shows the concentration profile in the section that had melted and subsequently been quenched. The section that remained solid had an average Bi composition of < 0.5at%. In the

liquid section, most measurements showed a composition of $\sim 2.5\text{at}\%$ Bi, but several measurements returned values of up to $87\text{at}\%$ Bi.

Melting Distance vs. Time Data

Tables 2, 3, and 4 display the data from C195-T210, C429-T210, and C429-T175, respectively. Most experiments have less than 5 data points for each set of conditions. This is because in most experiments, at least one of the data points was corrupted by the liquid leaking out of the capillary and losing contact with the solid before the experiment had concluded. In some cases, all of the samples were lost or corrupted.

The data points themselves are plotted against several models in Figures 58-60. Microsoft Excel generated the lines of best fit after choosing a power relationship between the variables. The exponent and the pre-exponential constant were calculated from the data. Figures 61-63 show the plots of the data as means with error bars against several models. The standard error was used to calculate error bars for the data points. Standard error was taken as standard deviation divided by the square root of the number of data points. A range of values from the mean plus or minus two times standard error gives an error bar that encompasses the true average value with 95% confidence.

Model Calculations

The data in the Figures 58-63 are plotted along with several models to observe the degree of agreement. The models, listed in order of lowest predicted melting rate to highest, are:

- Equilibrium melting, no convection
- Non-equilibrium melting, no convection
- Equilibrium melting, convection
- Non-equilibrium melting, convection

The differences between the models are only briefly described here, but are dealt with in detail in the literature review.

The difference between the equilibrium and non-equilibrium melting models can be understood by considering the model proposed by Rettenmayr and Hillert based on the large difference between D_L and D_S . If diffusion in the solid is slow compared to the liquid, say $D_L > 10,000 \times D_S$ as in this case, one may be able to assume that the solid interface composition during melting is close to or equal to its initial composition [6]. The melting process, if fast enough, does not allow enough time for solute to diffuse into the solid and raise its composition to C_S . If this is the case and C_S^* is smaller than C_S , an interesting phenomenon arises in the system. Referring to the G-X curves in Figure 29, a driving force for melting can be defined for liquid compositions within the two-phase field. The lowest theoretically possible concentration in the liquid occurs when there is negligible diffusion in the solid (hence $C_S^* \approx 0$) and the driving force needed for migration is negligible (hence $\Delta G_m \approx 0$). This value of C_L^* is dubbed C_L^{\min} by Rettenmayr and is noted on Figure 29. Melting with these interface compositions can continue until complete mixing in the liquid at C_L^* occurs.

This loss of equilibrium at the interface, of course, corresponds to different migration rates than equilibrium melting. One way to predict the effects of the interface compositions deviating from equilibrium is via the diffusion solution for solutal melting. The relevant equations are below.

$$z_I = 2d_{L-i}\sqrt{D_L t} = 2d_{S-i}\sqrt{D_S t} \quad (14)$$

$$v = d_{L-i}\sqrt{\frac{D_L}{t}} = d_{S-i}\sqrt{\frac{D_S}{t}} \quad (15)$$

$$\sqrt{\pi} = \frac{C_{bulk} - C_L}{C_L - C_S} \frac{e^{-d_{L-i}^2}}{d_{L-i}(1 + erf(d_{L-i}))} + \frac{C_0 - C_S}{C_L - C_S} \frac{e^{-d_{S-i}^2}}{d_{S-i}(1 - erf(d_{S-i}))} \quad (18)$$

Above, z is position, v is velocity, D is the diffusion coefficient, t is time, d is a dimensionless position value, and C_0 is initial solid concentration, C_{bulk} is the initial liquid composition, and C_S and C_L are equilibrium interface concentrations. As for subscripts, L denotes liquid phase, S denotes solid phase, and I denotes an interface value. (14) gives an expression for the position of the interface against time and (15) for velocity against time. (18) relates the dimensionless position d to the concentration profile of the system. Although the equations cannot be derived algebraically, the position-time and velocity-time profiles change if one inserts different values for interface concentrations than the equilibrium values because of (3).

The migration rate of the interface is inversely proportional to the interface concentrations. Therefore, if the properties of the system tend to drop the interface values below their equilibrium values, the equations predict a higher interface migration rate. The highest possible rate can be found by replacing zero for C_S and C_L^{min} for C_L . The lowest occurs when equilibrium values from the phase diagram are used for C_L and C_S . *This maximum rate is the one plotted in the non-equilibrium melting models.*

The difference between the convection models is simple. Both models predict that only diffusion occurs in the capillary. The models differentiate between whether or not convection occurs outside the capillary near the entrance. In the model that assumes no convection occurs, the concentration outside the capillary becomes depleted as solute diffuses into it. In the model that assumes that convection is present, the entrance to the capillary remains fixed at the bulk value. Convection currents, if present, would carry solute to the capillary entrance to eliminate concentration gradients faster than diffusion can create them. Quantitatively, this leads to

different boundary conditions for solving the diffusion equations that lead to (3). Solving using these new boundary conditions yields:

$$\sqrt{\pi} = \frac{C_{bulk} - C_L}{C_L - C_S} \frac{e^{-d_{L-i}^2}}{d_{L-i}(\text{erf}(d_{L-i}))} + \frac{C_0 - C_S}{C_L - C_S} \frac{e^{-d_{S-i}^2}}{d_{S-i}(1 - \text{erf}(d_{S-i}))}. \quad (21)$$

To summarize, the differences between the models, quantitatively, manifest in the following way:

- For the models that do not include convection, equation (18) is used, and for those that do, equation (21) is used.
- In the equilibrium melting models, equilibrium interface concentrations, C_L and C_S are plugged into equation (18) or (21) (depending on the convection conditions).
- In the non-equilibrium models, the lowest possible interface concentrations are plugged into either (18) or (21); that is, C_L^{\min} for C_L , and C_0 for C_S . These values are determined from the initial solid concentration and the G-X curves for the system.

For more details on the models, see the *Diffusion* section of the *Literature Review*.

C195-T210

Micrographs for these experiments can be found in Figure 37-41. The remelting interface is clearly planar in most cases. The thin strip between the pure Sn matrix and the dendritic region is the region of planar solidification. For these experiments, the length of that region was about 17 μm . This value was consistent between samples regardless of the time spent in the melt.

Figure 58 shows the plot of the data points against the models along with a computer generated trend-line, while Figure 61 contains a plot of the means for each experimental time against the models. The plot of the means contains error bars of 95% certainty.

The spread of the data is relatively high. This may be due to the fact that some of the data points came from earlier experiments during which the temperature profile was much more unstable. The trend-line in Figure 58 agrees rather well with the dependence on the square root of the abscissa present in the models based on diffusion control. The R^2 value of 0.91 for the power relationship is higher than that for the linear relationship, 0.85, thus indicating a significant departure from linearity. The trend seems to be fairly close to both the *Non-Equilibrium, No Convection* model and the *Equilibrium, Convection* model, but closer to the *Equilibrium, Convection* model. The error bars in Figure 61 encompass both of the nearby models.

C429-T210

Micrographs for these experiments can be found in Figure 42-44. The micrographs show that the melting interface was planar in most cases. For these experiments, the length of the planar solidification region was similar to that seen in the C195-T210 experiments, about 15-17 μm . Once again, the time spent in the melt did not seem to affect the size of this region.

Figure 59 shows the plot of the data points against the models along with a computer generated trend-line, while Figure 62 contains a plot of the means for each experimental time against the models. The plot of the means contains error bars of 95% certainty.

The spread of the data is lower than that encountered in the plots of C195-T210. This may be due to the more stable temperature profiles for C429-T210. Once again, the trend-line in Figure 59 agrees rather well with the dependence on the square root of the abscissa present in the models based on diffusion control. The data has an R^2 value of 0.96 for the power relationship and 0.94 for the linear relationship. Thus once again the power relationship yields a better fit, but the linear model may be feasible as well. The trend seems to be fairly close to the *Non-*

Equilibrium, No Convection model and the *Equilibrium, Convection* model, but closer to the former.

C429-T175

Micrographs for these experiments can be found in Figure 45-49. The micrographs show that the melting interface was planar in most cases. The lengths of the planar solidification regions were significantly shorter than in C195-T210 and C429-T210. In these experiments, planar solidification occurred for about 6-9 μm before breaking down into dendritic solidification. As in all the other experiments, the amount of time spent in the melt did not seem to affect the size of this region.

Figure 60 shows the plot of the data points against the models along with a computer generated trend-line, while Figure 63 contains a plot of the means for each experimental time against the models. The plot of the means contains error bars of 95% certainty.

The spread of the data is rather low and imply a clear trend. The data has an R^2 value of 0.889 for the power relationship and 0.895 for the linear relationship. Since these numbers are so close (< 0.1% difference), either trend could possibly be the correct relationship. It should be noted the in both C195-T210 and C429-T210 the power relationship yields a better fit. In either case, the trend seems to agree well with the *Equilibrium, No Convection* model; the model with the lowest predicted melting rate. No other models appear to be relevant to these data points.

Kinetic Relationships

Table 5 contains numbers relevant to the calculation of kinetic values for the Sn-Bi system. Data was gathered for three sets of conditions.

The independent variables were T, the temperature, and C_{bulk} , the concentration of the bulk liquid. The “Data” column indicates the nature of the data in the row. Three rows of data

were gathered from experiments, while the bottom row of data was interpolated from the top two rows. This will be explained below. C_L is the equilibrium liquid concentration for the given temperature, and ΔC , the supersaturation, is equal to the difference between C_{bulk} and C_L . A and B are constants in the displacement curve equations calculated from the data gathered under the determined conditions. The equation for displacement of the interface, z_I , was derived in the *Diffusion* section of the *Literature Review* and has the form

$$z_I = At^B. \quad (22)$$

In (22), t is time. A is a characteristic value for each of these experiments, however, due to the slightly different values of B between them, A has slightly different units for each set of conditions. In order to compare the values of A for the different experiments, they had to be normalized. This was done by finding the best-fit lines for which B was equal to 0.5 and recalculating the value of A. These values can be found in the final column of Table 5, and are used for the kinetic computations.

Change in A with Driving Force

We can calculate an approximation for the change in A with driving force (supersaturation) by comparing the data from the first and third rows of Table 5. These experiments were carried out at the same temperature with different degrees of supersaturation. Rettenmayr et al. found a linear relationship between driving force and average velocity in their experiments. By plotting A against ΔC , one obtains the graph in Figure 64. It is peculiar that the line does not intersect contain the point (0,0). Theoretically, when $\Delta C = 0$, the driving force should disappear and the velocity should equal zero. It seems that this relationship does not hold for these experiments.

Despite the fact that Rettenmayr saw a linear relationship in his work, another possibility may exist. By examining equations (18) and (21), the expected changes in A with supersaturation ΔC ($\Delta C = C_{\text{bulk}} - C_L^*$) can be plotted. The exact relationship cannot be derived due to the nature of the governing equations, but the shape of the curve can be plotted by calculating the relationship at different points. Consider the following equations that predict the relationships between bulk concentrations, interface concentrations, and interface position:

$$A = 2d_{L-i}\sqrt{D_L} = 2d_{S-i}\sqrt{D_S}, \quad (\text{R-1})$$

$$\sqrt{\pi} = \frac{C_{\text{bulk}} - C_L}{C_L - C_S} \frac{e^{-d_{L-i}^2}}{d_{L-i}(1 + \text{erf}(d_{L-i}))} + \frac{C_0 - C_S}{C_L - C_S} \frac{e^{-d_{S-i}^2}}{d_{S-i}(1 - \text{erf}(d_{S-i}))}, \quad (\text{R-2})$$

$$\frac{C_{\text{bulk}} - C_L}{C_L - C_S} = \sqrt{\pi} \frac{e^{-d_{L-i}^2}}{d_{L-i}(1 + \text{erf}(d_{L-i}))}. \quad (\text{R-3})$$

Since $D_L \gg D_S$, we can omit the second term on the right-hand side of the equation (R-2) [10], and the result is (R-3). Different initial liquid concentrations, C_{bulk} , give different values for d_{L-i} and in turn, different values for A . The plots using (R-1) and (R-3) are found in Figure 65. Relationships for two models at 210°C, the *Non-Equilibrium, No Convection* and *Equilibrium, Convection* are found in this plot, as well as the data from the experiments. The plots of the models depart from linearity, and the data do indeed fit much better with this type of relationship. Additionally, this type of relationship makes more sense in that the average velocity approaches zero as the supersaturation approaches zero. If the diffusion equations are valid at all, then the proper relationship between velocity and supersaturation has what appears to be a power relationship with an exponent less than unity. The resulting trend-line for the data can be found in Figure 65. This trend-line was used to calculate the data in Table 5.

It should be noted that the departure from linearity in the present case is exaggerated by the fact that the diffusion coefficient changes significantly from the lowest concentrations to the

highest. The effect of this change was accounted for in the calculation of the curved in 65. Higher concentrations were explored in this study than in Rettenmayr's, making the change in diffusion coefficient more pronounced. This may be one reason why Rettenmayr observed a linear relationship.

Change in A with Temperature

In order to investigate the change in A with temperature, we need at least two data points with constant driving force. We have data at two different temperatures, but none have the same amount of supersaturation. However, by using the relationship gained from Figure 65 we can approximate A at 483K with the same supersaturation as the experimental data from 448K. The results of these calculations are in the last line of Table 5.

With two data points at equal supersaturation and different temperatures, we can begin to quantify the relationship between temperature and A. Typically, the rates of atomic phenomena and temperature have an Arrhenius relationship. Indeed, Rettenmayr et al. [9] as well as Kang [15] have shown that temperature and melting interface velocity can be described this way. Figure 66 shows the logarithmic plot of the two data points along with the equation of the line that they imply. From the equation in Figure 66 we can calculate the expression for A (in mm/s^{1/2}) as a function of temperature (in K):

$$A = 2.208 \times 10^5 \exp\left(-\frac{61,526}{RT}\right). \quad (\text{R-4})$$

In (R-1), R is the gas constant with units of J·mol⁻¹K⁻¹. The activation energy is therefore 61,526 J·mol⁻¹. It is worth noting that the calculated activation energy for diffusion of Bi in Sn changes across the concentration profile from 18,430 J·mol⁻¹ at the bulk composition of 42.9at%Bi to 11,152 J·mol⁻¹ near the interface composition of 12.4at%Bi [16].

Error

Temperature Fluctuations

The spread in temperatures for different experiments is small, and the temperature remains fairly constant during the experiments. A small dip in temperature, usually $\sim 0.1^\circ\text{C}$ is noticeable in each of the profiles corresponding to the moment the Teflon tape is removed from the capillaries. The dip may be due to the hot liquid coming into contact with the slightly cooler glass/metal underneath the Teflon insulation. After the dip, the temperature slowly rose back up to the temperature reached during the stabilization period.

There were small variations in the conditions for experiments that were intended to have identical conditions. For example, there were 5 experiments carried out at 210°C with a bulk melt concentration of 42.9at% Bi. However, there is a small degree of spread associated with the actual conditions from one experiment to the next, say, between C429-T210-10 and C429-T210-20. The temperature profiles for the different runs can be found in Figures 67 and 68. The different lengths of the profiles indicate the different durations in the melting times. The spread between the temperatures during different experiments was always less than 0.6°C . The temperature used in the calculations was the average of the average temperature during each experiment. Hence, the temperature in the calculations for C429-T210 was actually $209.8^\circ\text{C} \pm 0.3^\circ\text{C}$. This corresponds to ± 0.14 at% Bi in C_L , 0.042 at% Bi in C_S , and $0.0285 \times 10^{-6} \text{ cm}^2/\text{s}$ in D_L . The difference between the temperatures of the high melt and the low melt was usually smaller than 0.3°C over the distance of 2cm. Thus, assuming a linear temperature gradient between the high melt and low melt temperatures, the change in temperature due to this gradient during the longest melting distances ($\sim 3\text{mm}$) was still below 0.05°C .

Change in Melt Composition

The change in the composition of the melt between experiments was approximated by calculating the amount of solute diffused into the five capillaries during the experiment and subtracting that from the bulk. The most solute was diffused into the capillaries during the 5-C429-T210 experiments. Approximating a linear slope in the liquidus line for the small temperatures dealt with here, change in solute content of the melt is only about changed by 0.02% after 5 experiments. This corresponds to a small change in velocity.

Latent Heat of Melting

Melting consumes energy in the form of heat. We know that this reaction does not affect the global temperature inside the crucible enough to greatly disturb the melting rate (see above). However, the temperature change locally at the melting interface is a concern. The amount of heat consumed at the interface must be estimated. This can be accomplished by multiplying several physical properties together.

The experimental conditions that should have incurred the most possible cooling will be examined. For these experiments, this was 1.45×10^{-4} mol of Sn melted (0.785 mm^2 capillary area \times 3mm penetration \times 6.14×10^{-5} mol/ mm^3 density). Multiplying this by the latent heat of fusion gives 1.02J of heat consumed by melting during the process. This corresponds to an average power of $340 \mu\text{W}$ if the energy is divided by 3000s, the amount of time needed to melt this much metal. Compared to the $\sim 100\text{W}$ power of the furnace, the energy consumption of the latent heat of melting is negligible.

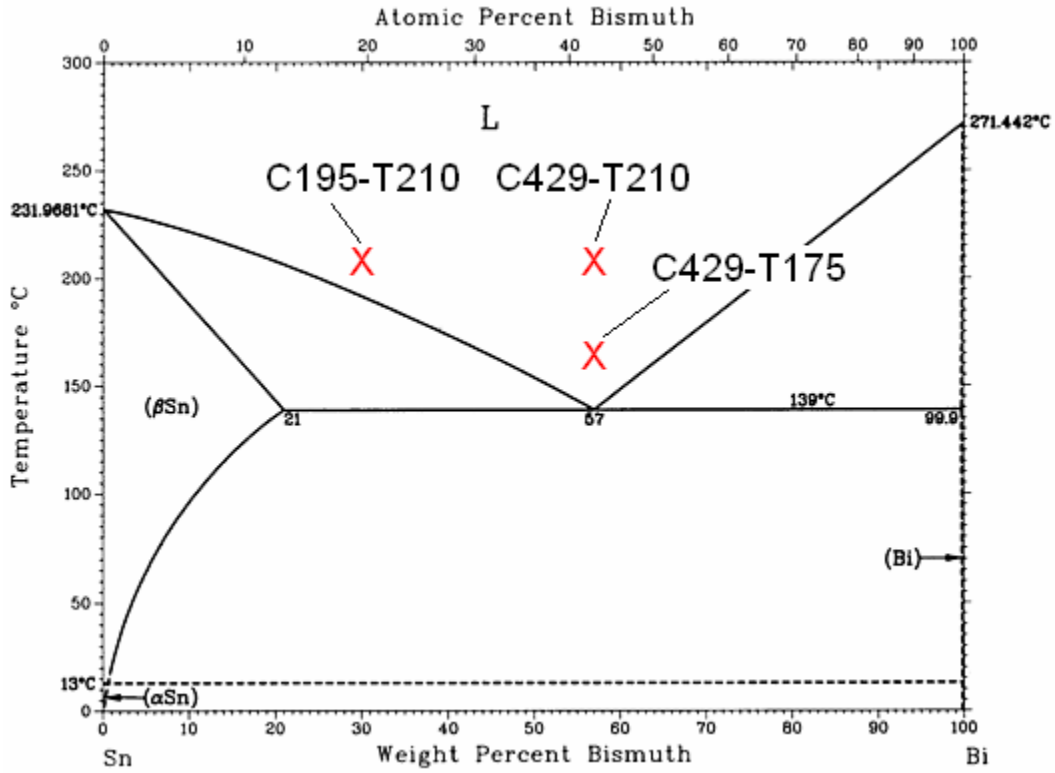


Figure 36 Sn-Bi phase diagram conditions explored in this study. The concentrations refer to the concentrations of the melt in the reservoir. The concentration of the solid was always pure Sn.

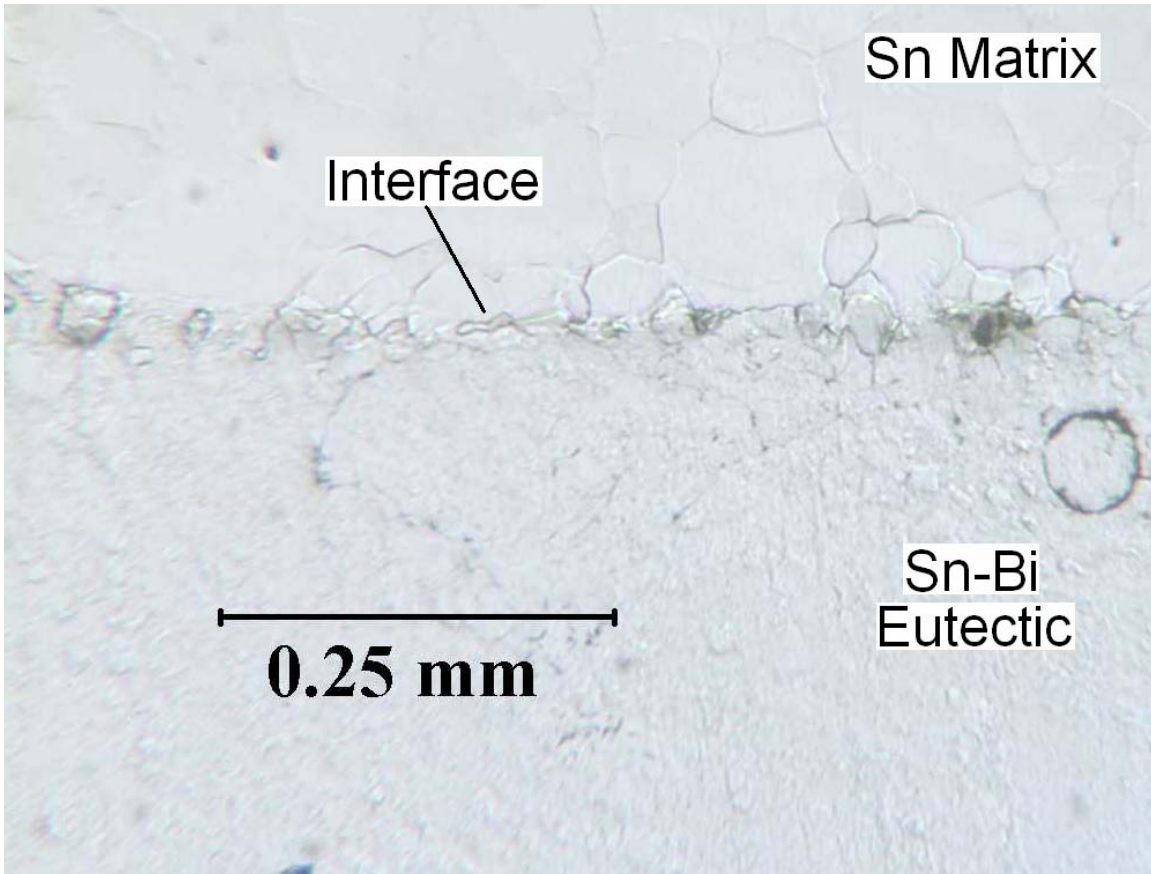


Figure 37 C195-T210-10 at 100X. The Sn matrix and the Sn-Bi eutectic are marked. The interface is planer along with most of the other samples.

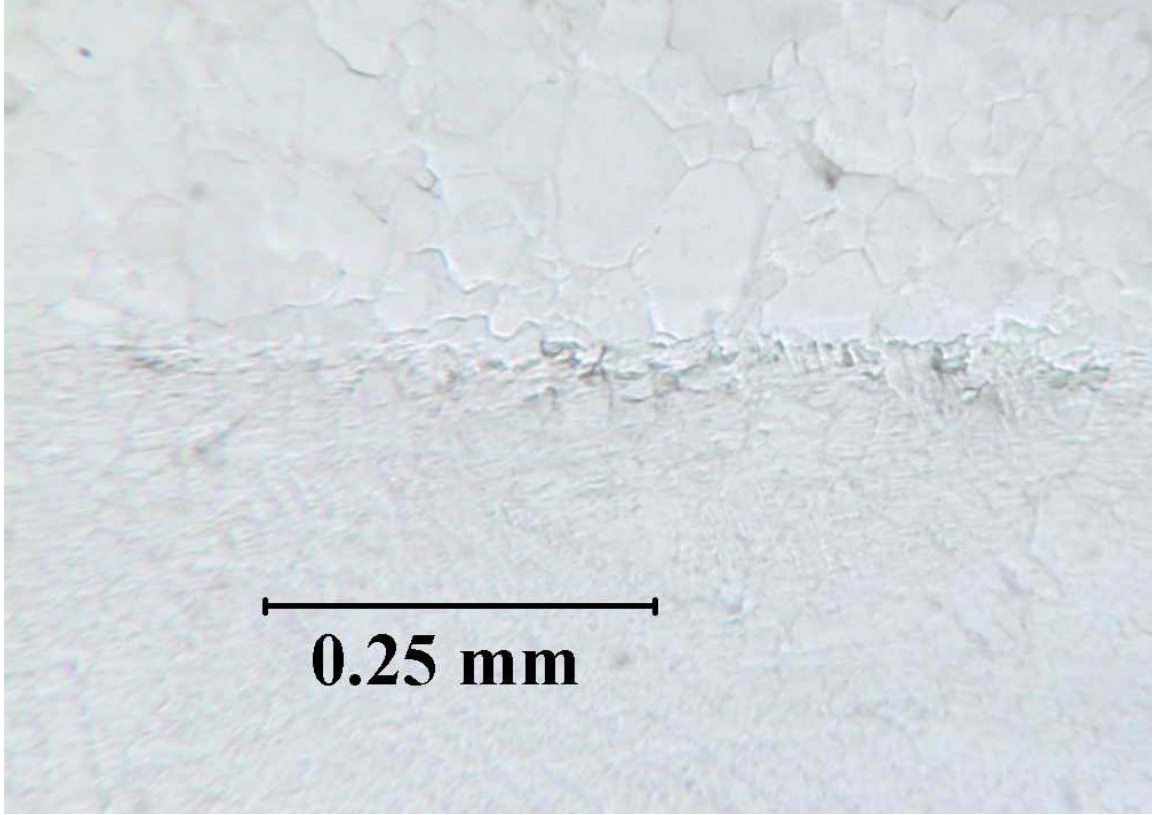


Figure 38 C195-T210-20 at 100X.

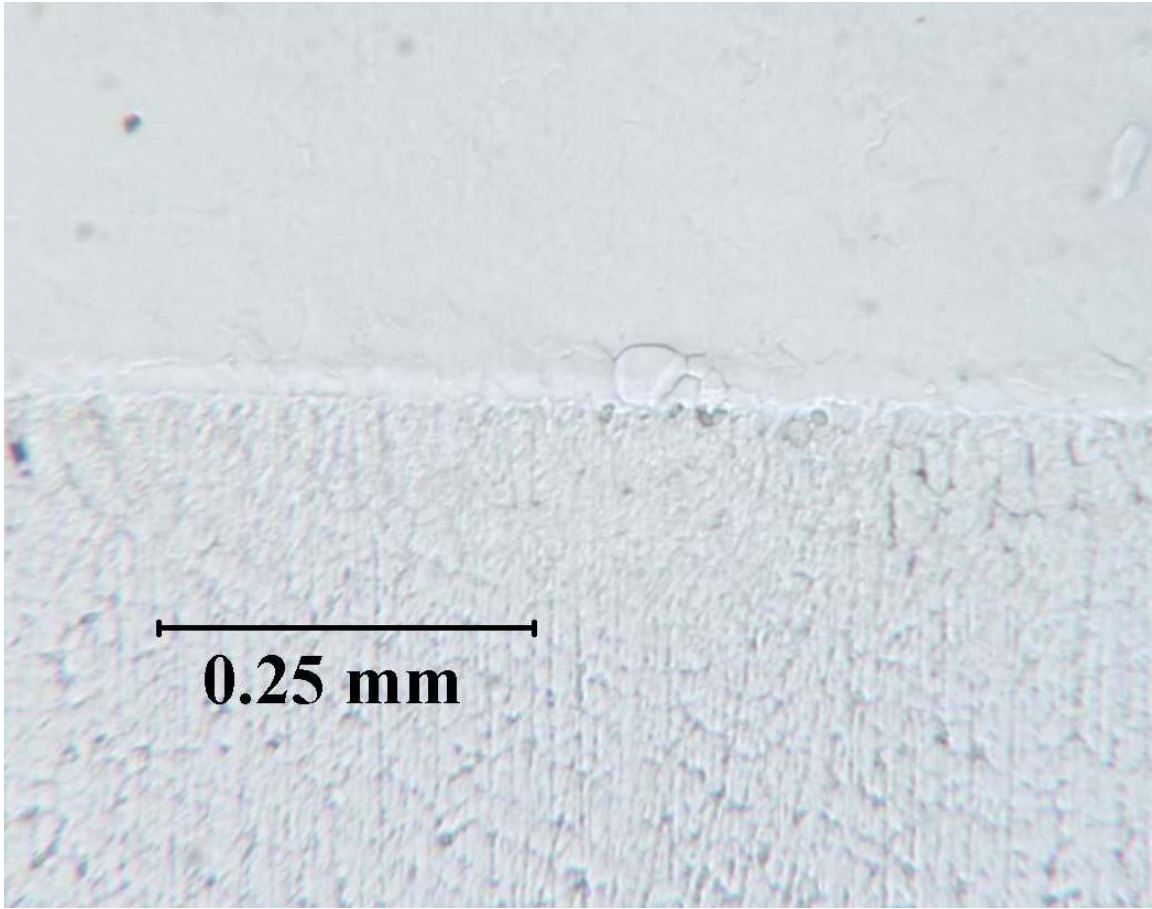


Figure 39 C195-T210-30 at 100X.

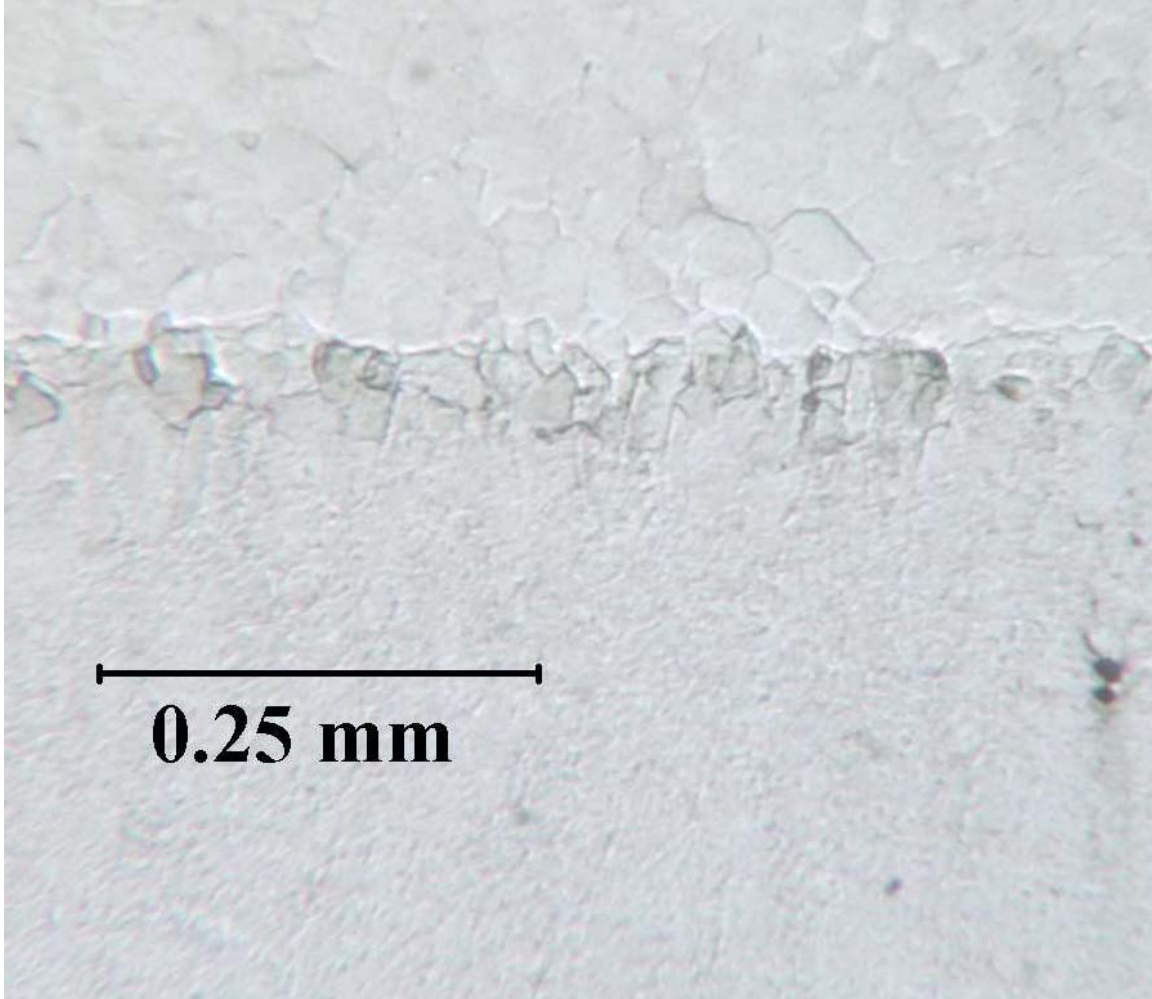


Figure 40 C195-T210-40 at 100X.

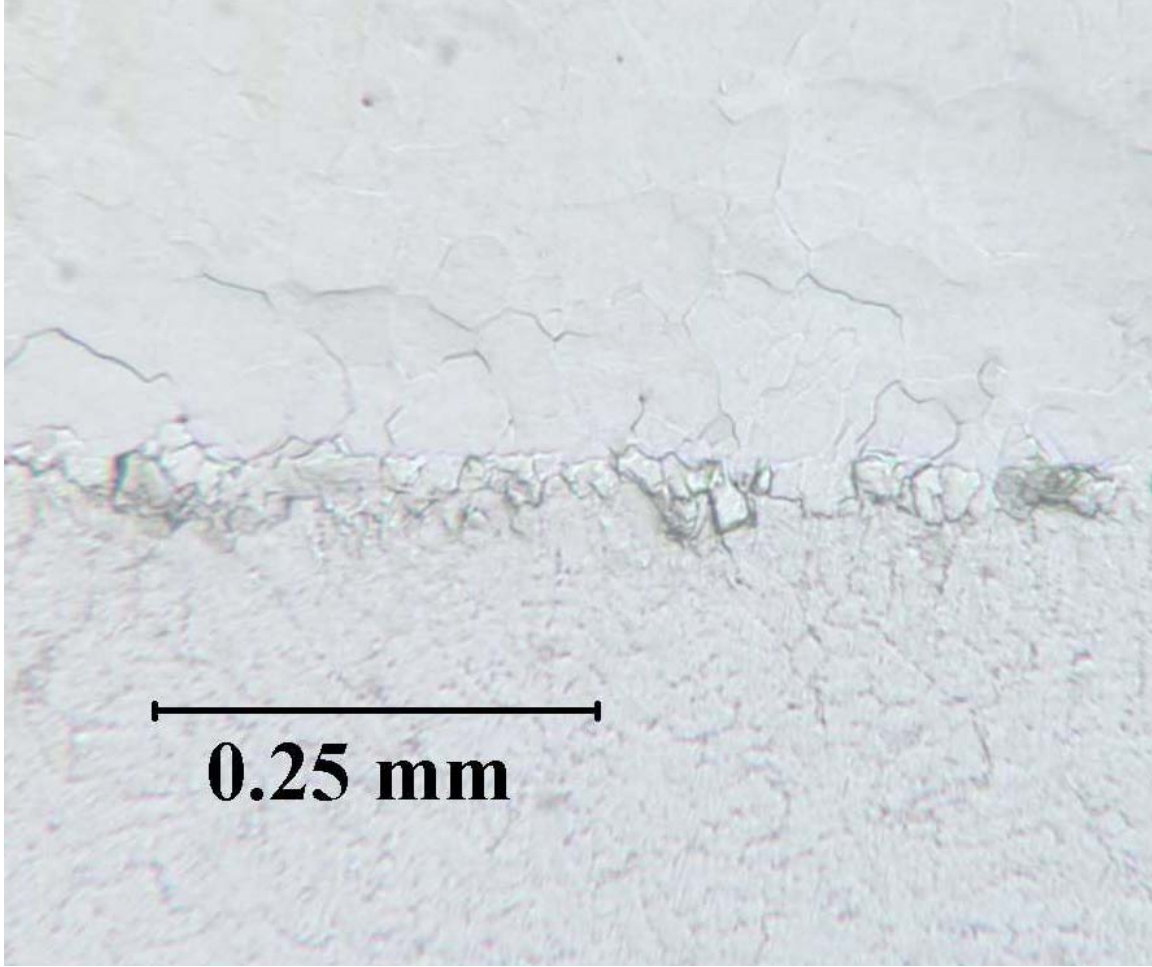


Figure 41 C195-T210-50 at 100X.

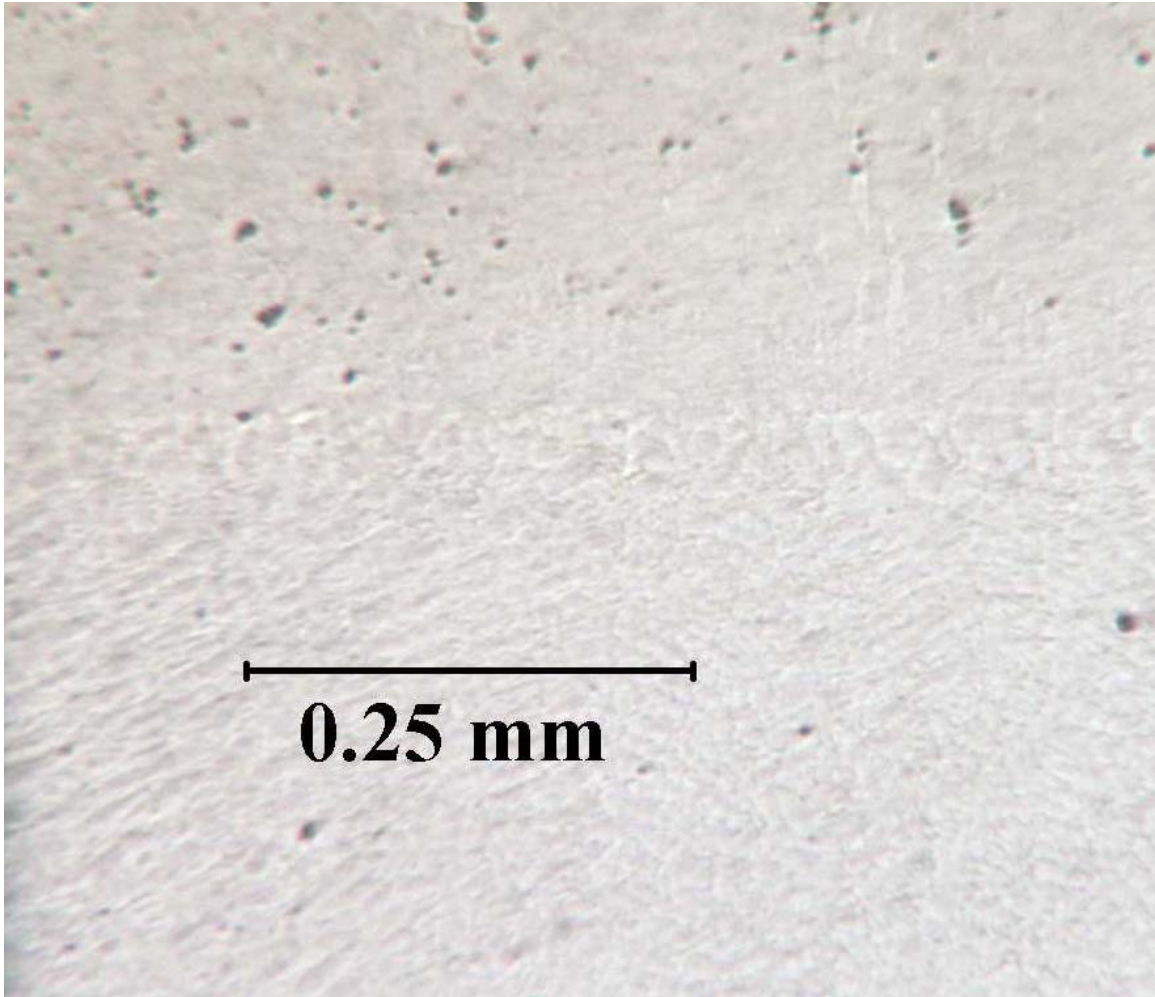


Figure 42 C429-T175-10 at 100X.

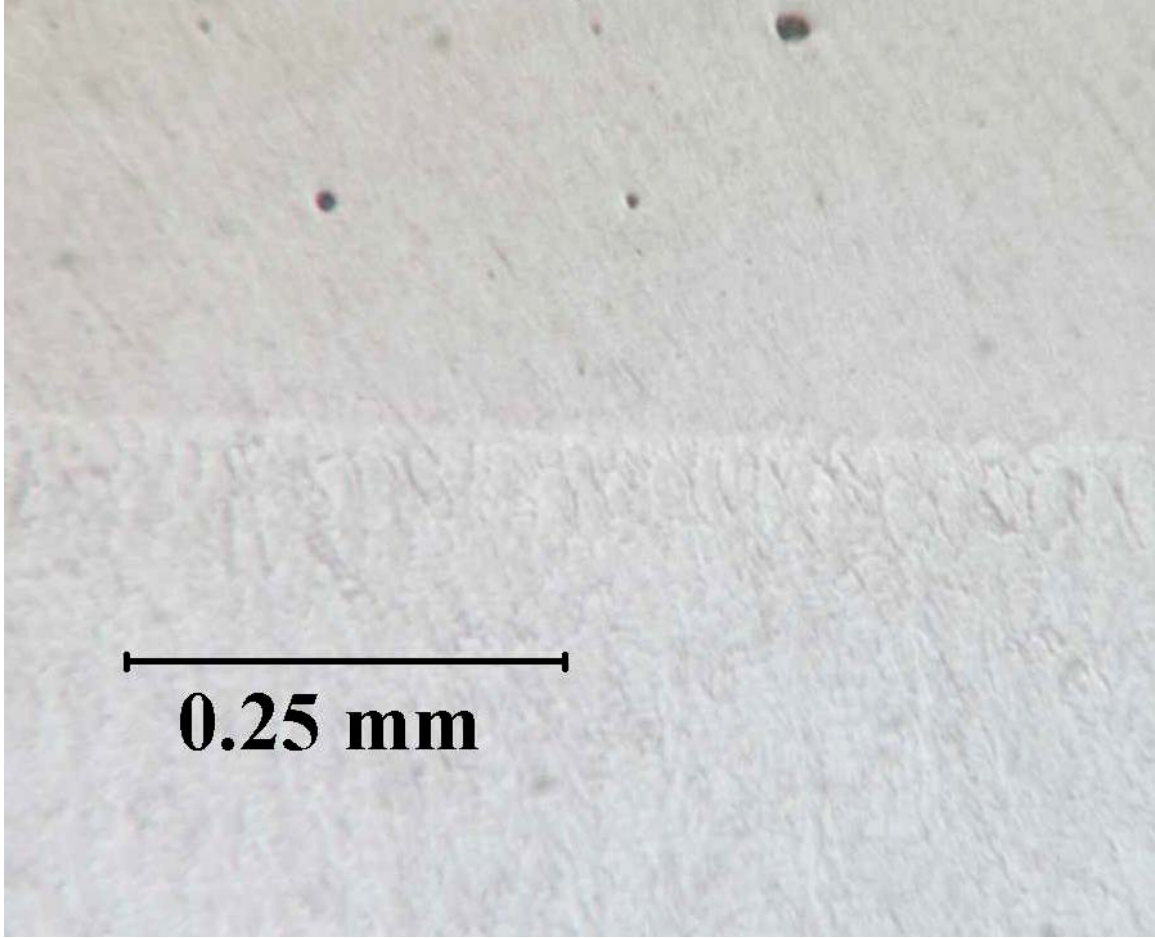


Figure 43 C429-T175-20 at 100X.

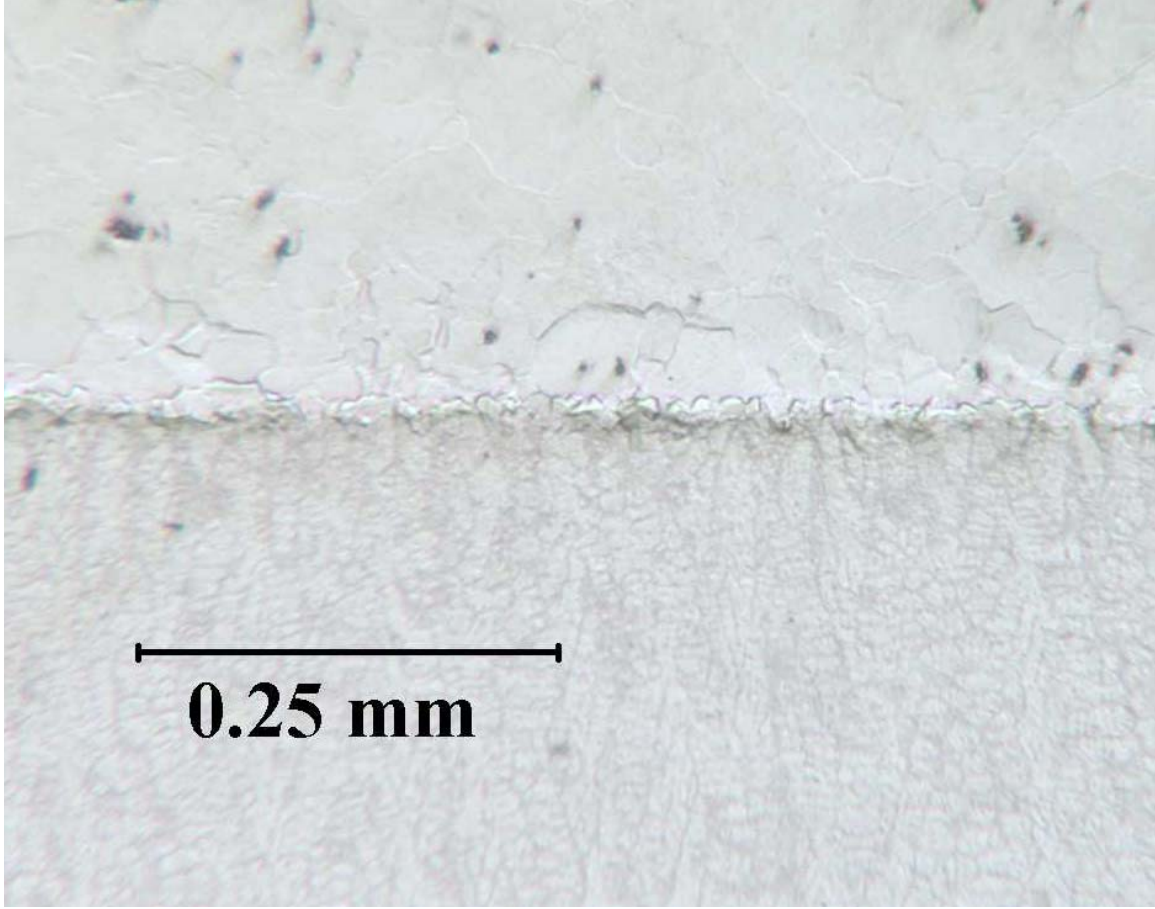


Figure 44 C429-T175-30 at 100X.

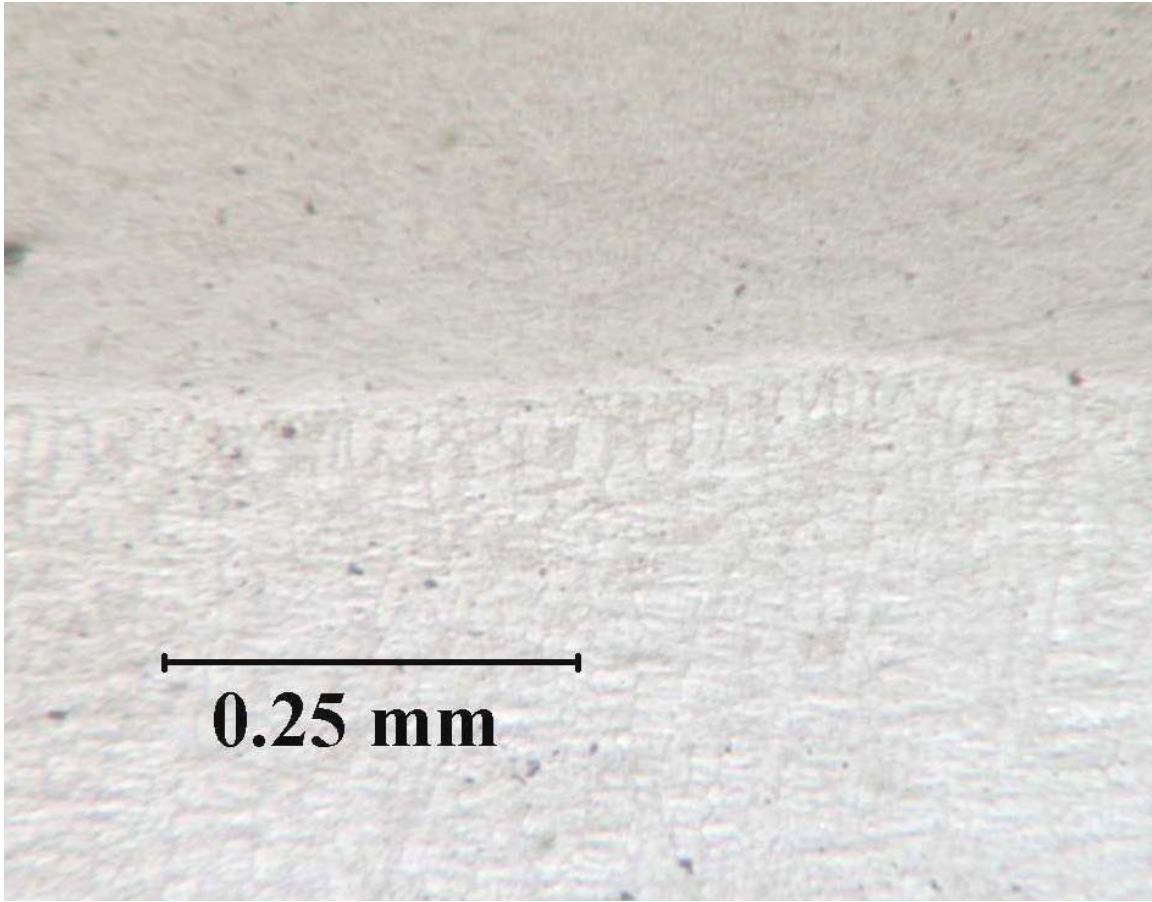


Figure 45 C429-T175-40 at 100X.

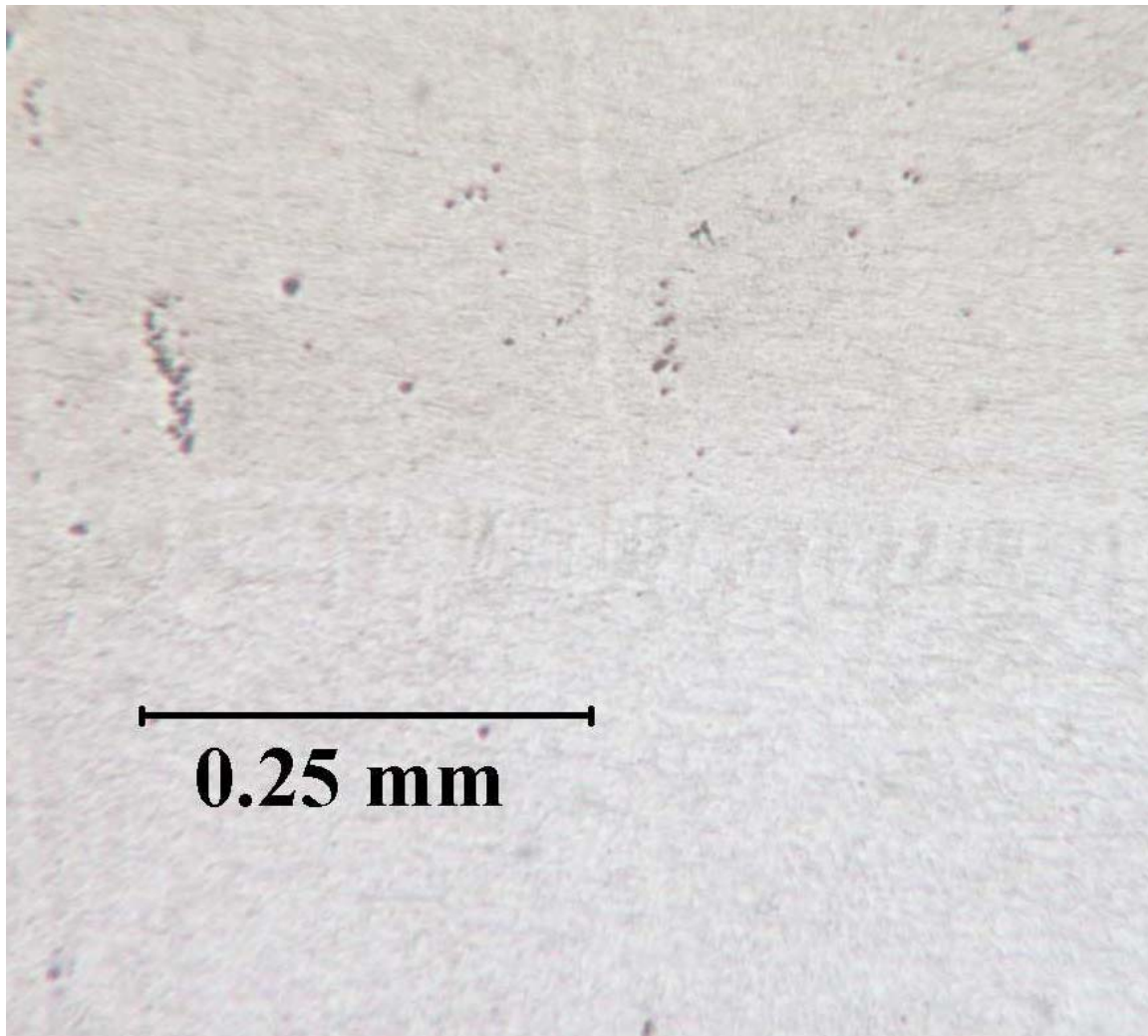


Figure 46 C429-T175-50 at 100X.

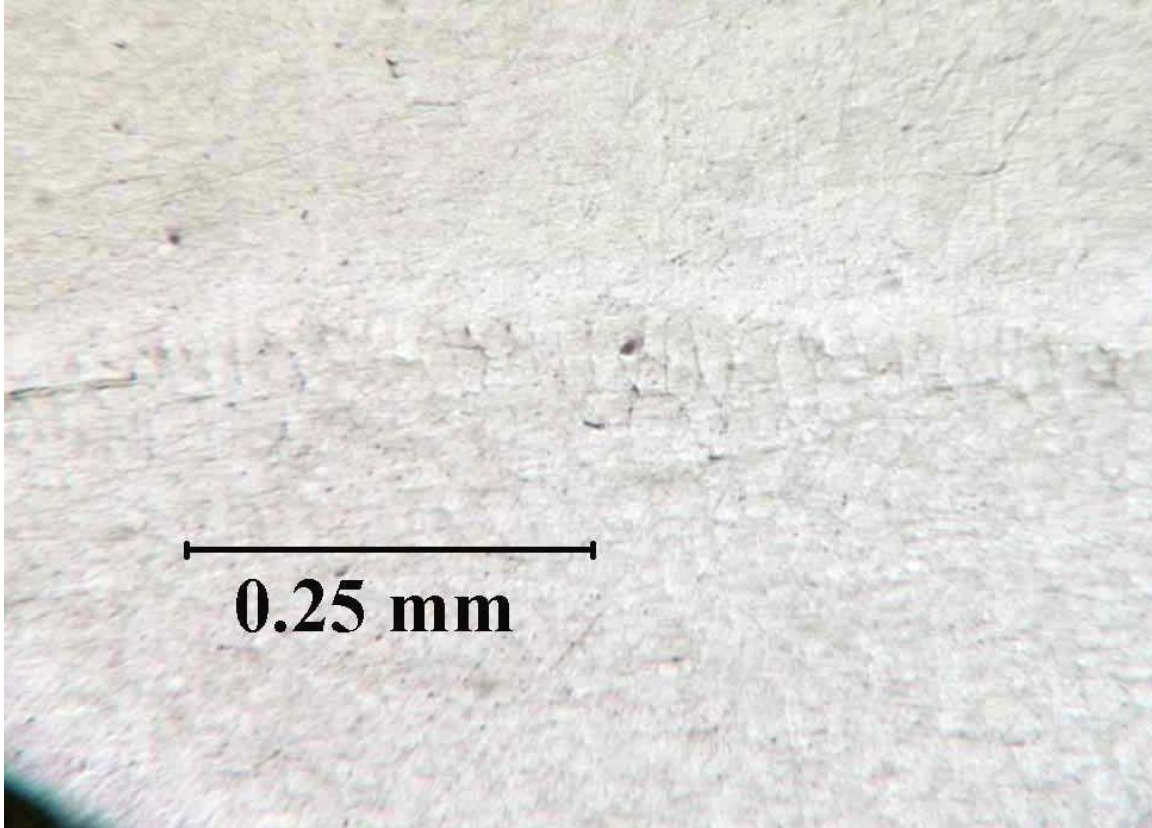


Figure 47 C429-T210-10 at 100X.

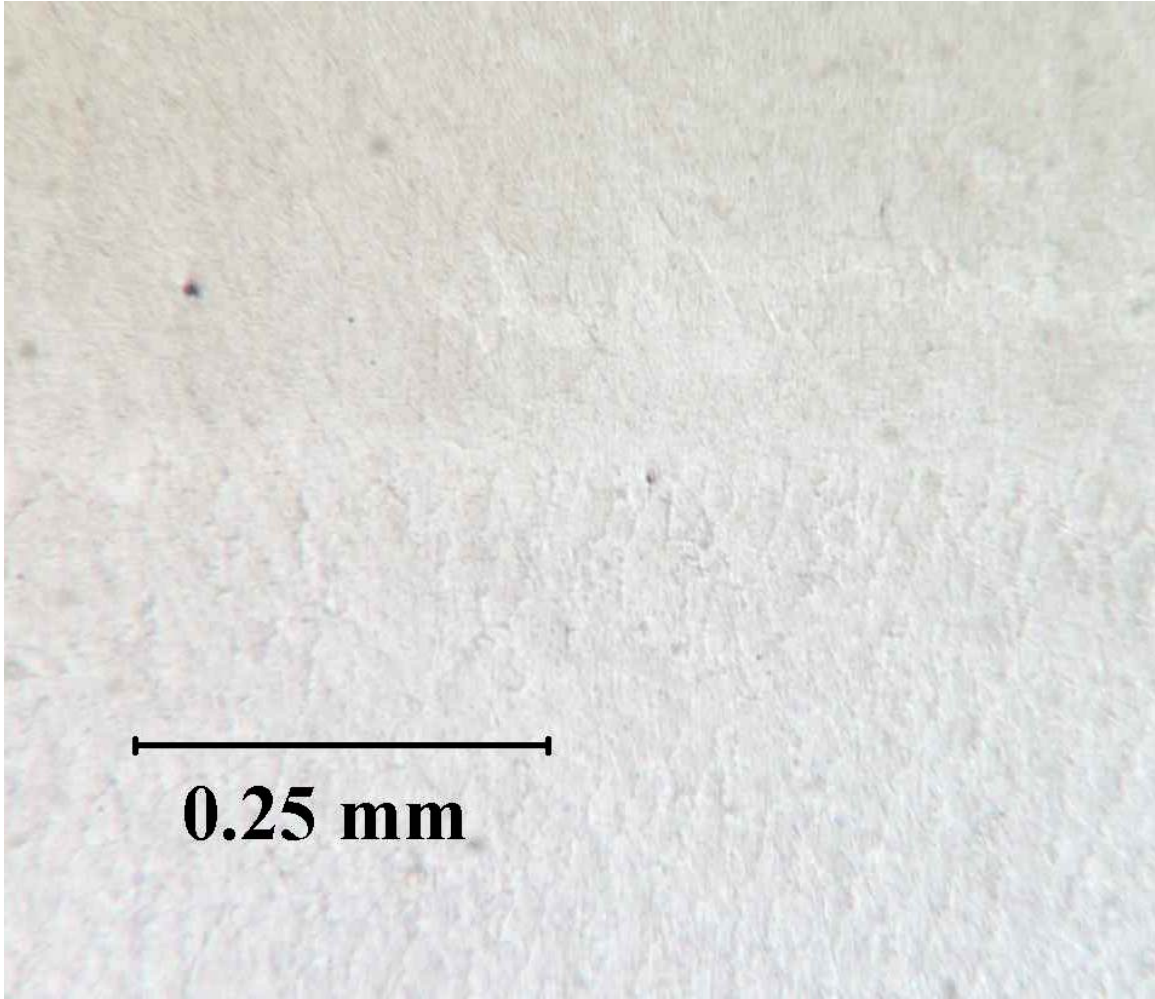


Figure 48 C429-T210-20 at 100X.

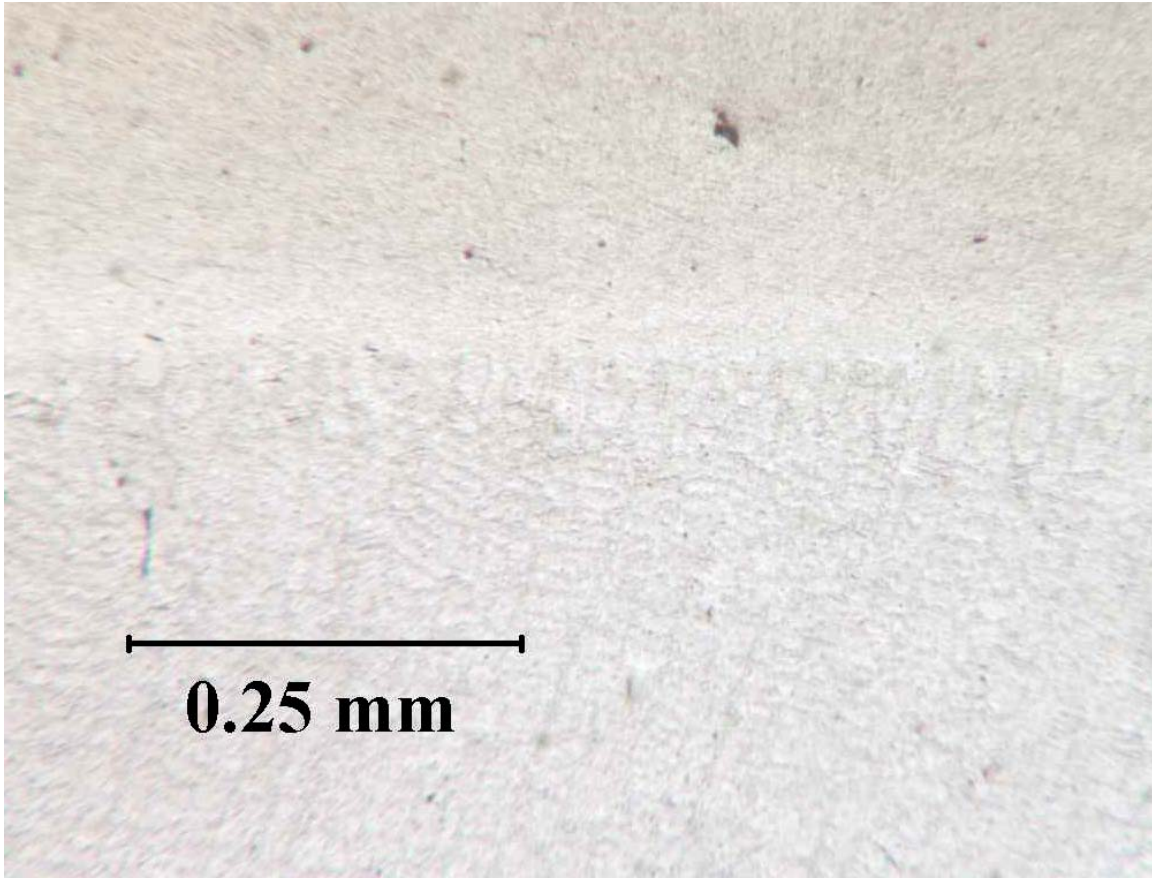


Figure 49 C429-T210-50 at 100X.

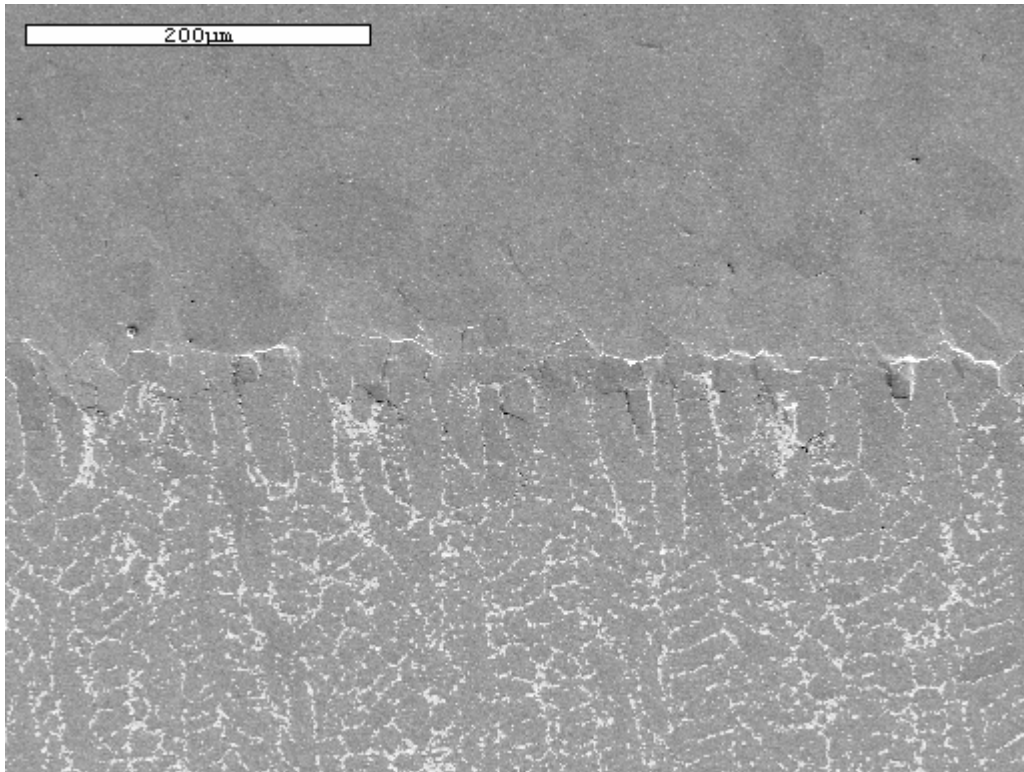


Figure 50 SE image of the melted interface at 200X. Sample was run at 210°C with a reservoir composition of 19.5at% Bi for 40 minutes.

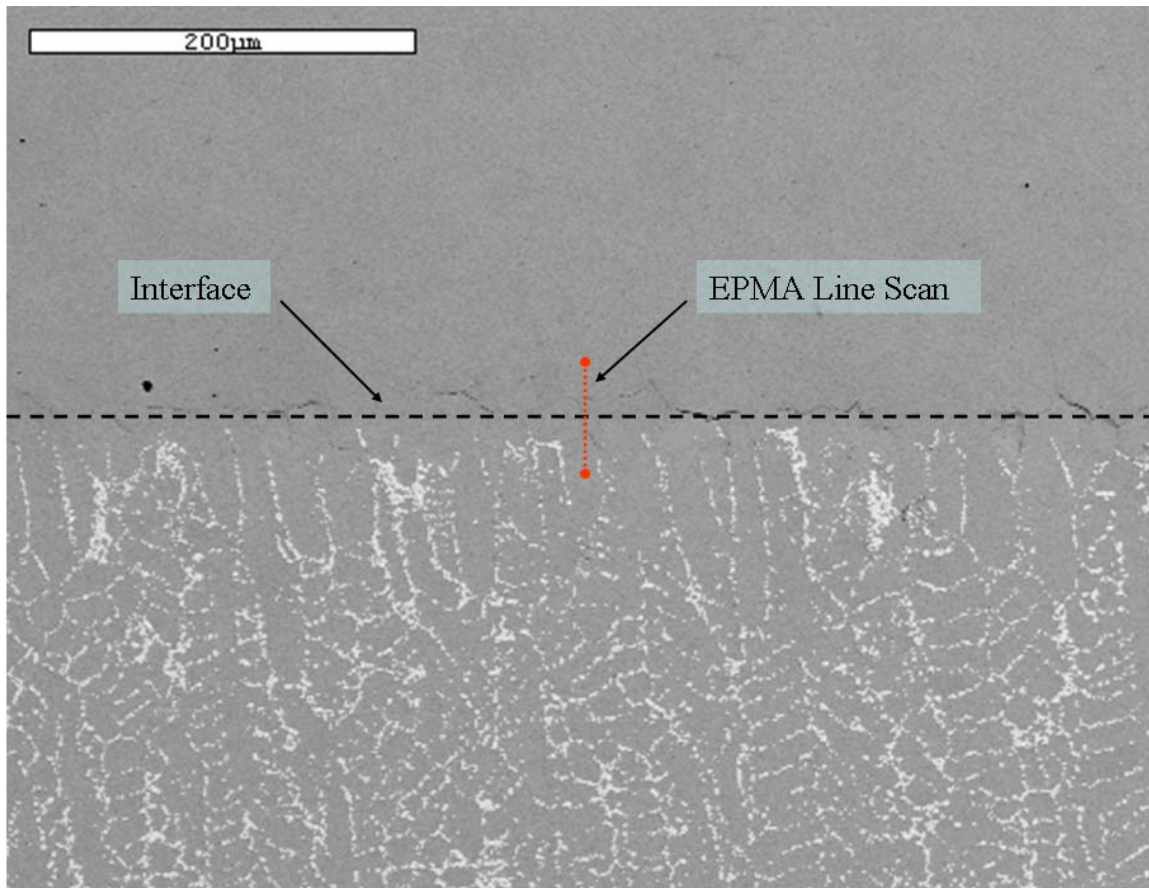


Figure 51 BSE image of the melted interface at 200X. Sample was run at 210°C with a reservoir composition of 19.5at% Bi for 40 minutes. The approximate location of the interface is shown with a black dotted line. The red dotted line shows the size and orientation of the line scan taken by the electron probe micro-analyzer. The results of the line scan are shown in Figure 57.

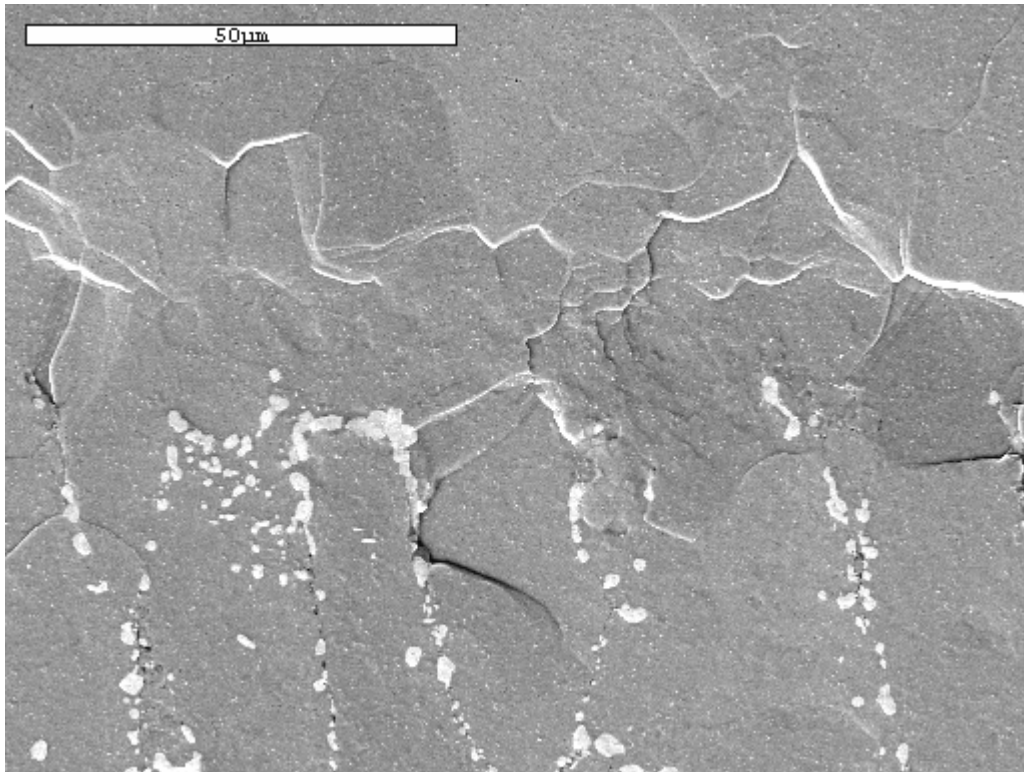


Figure 52 SE image of the melted interface at 1000X. The image is of the same sample shown in Figure 50.

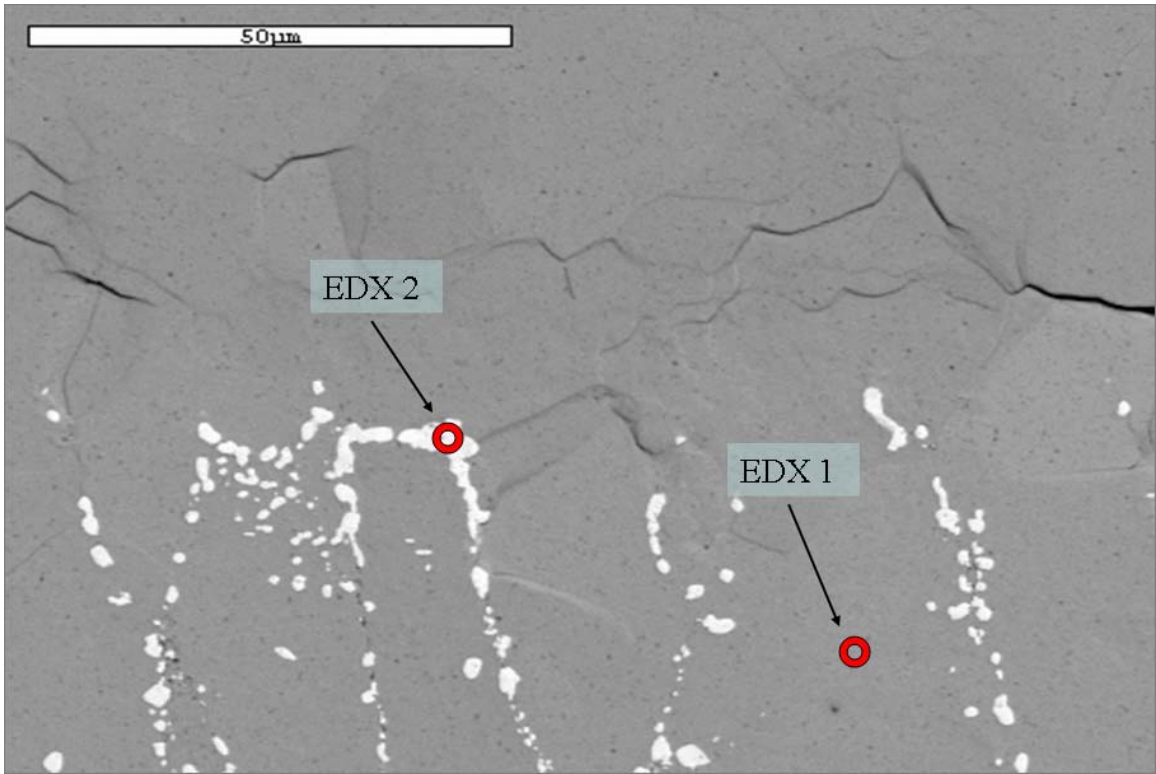


Figure 53 BSE image of the melted interface at 1000X. The image is of the same sample shown in Figure 50. The red circles indicate the areas that were chosen for EDX analysis. The spectrum obtained from EDX 1 is shown in Figure 54, and from EDX 2, in Figure 55.

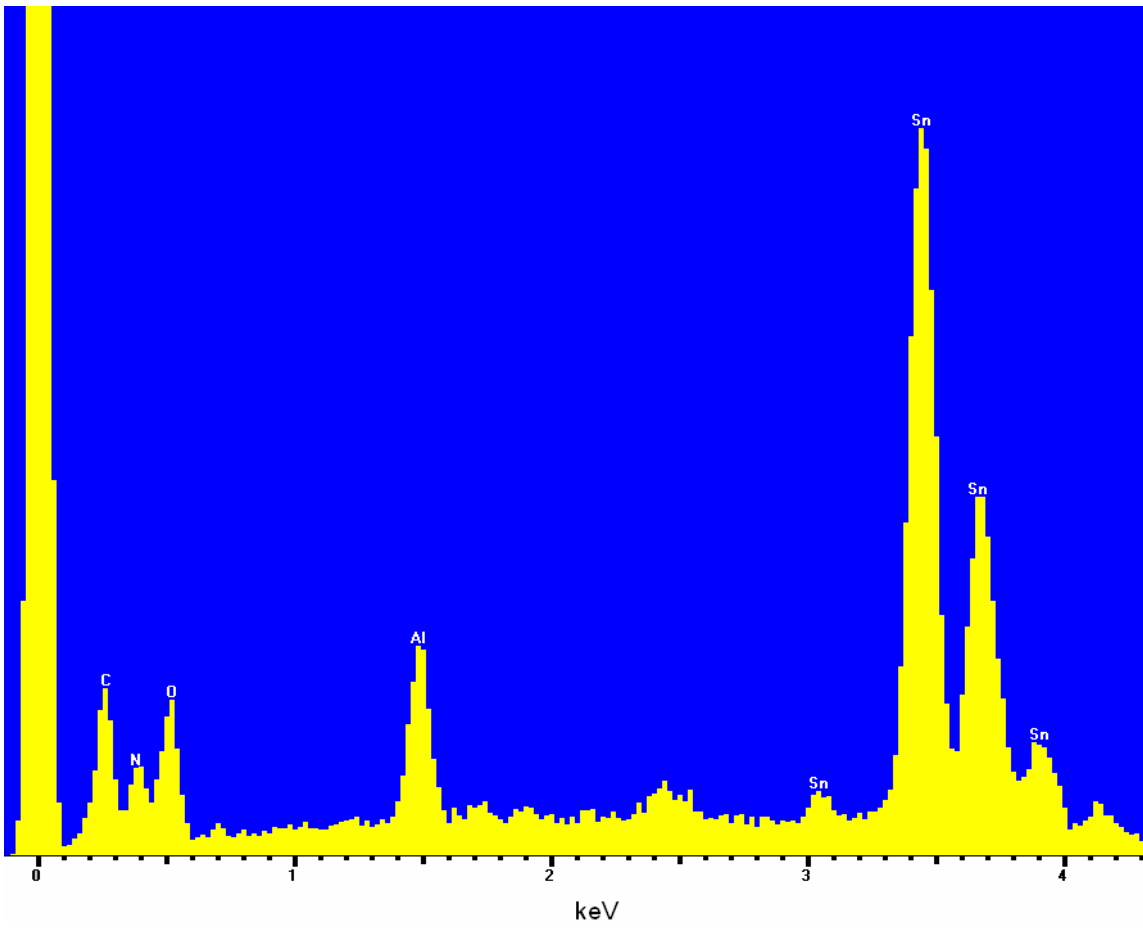


Figure 54 EDX 1 spectrum (see Figure 53).

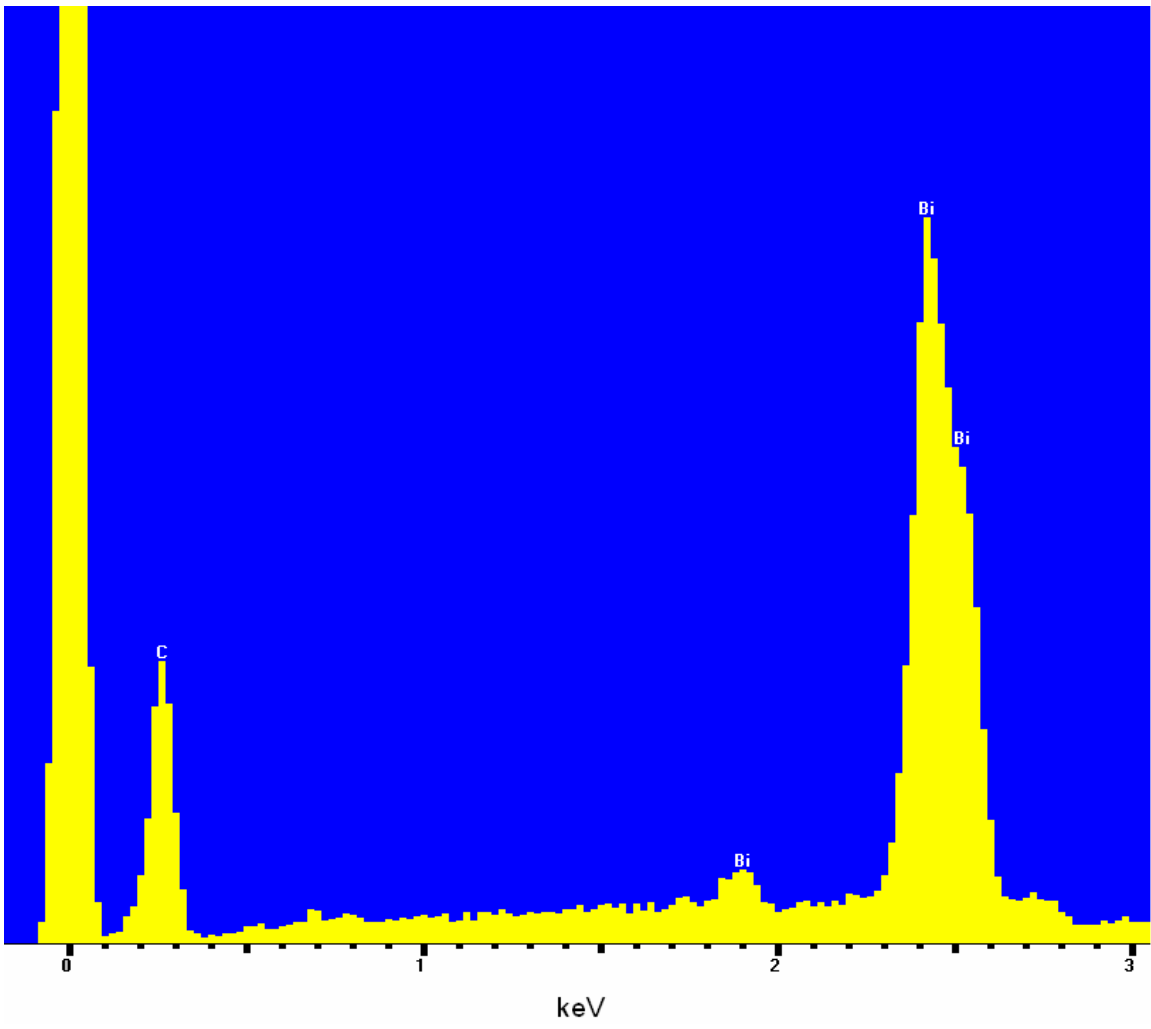


Figure 55 EDX 2 spectrum (see Figure 53).

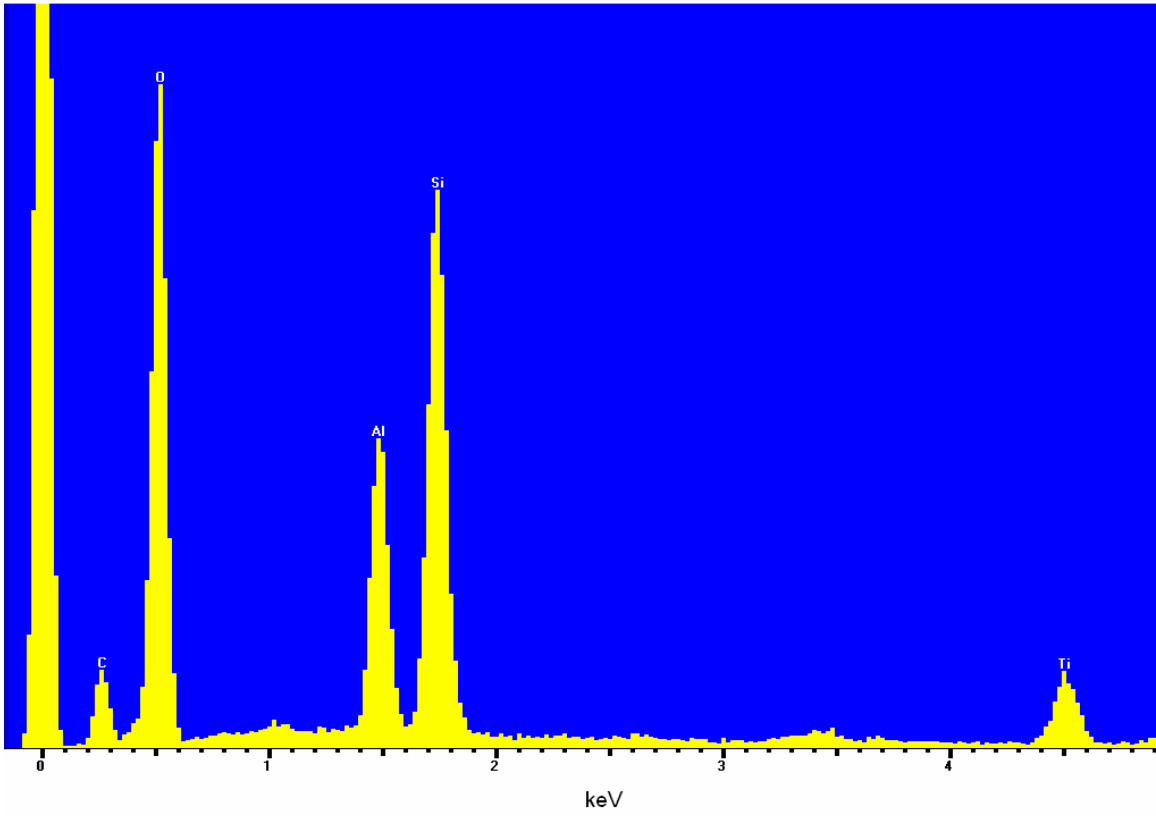


Figure 56 EDX analysis of black impurity particle.

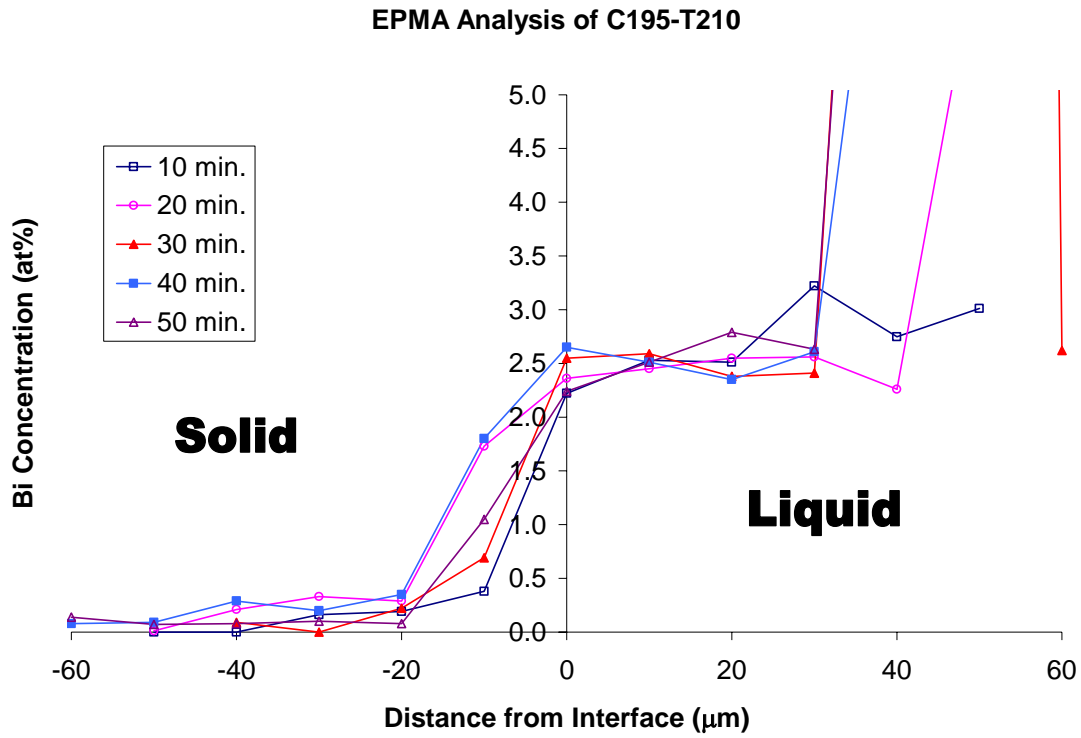


Figure 57 EPMA results from the samples run at 210°C with a reservoir composition of 19.5at% Bi. The y-axis is positioned in the approximate location of the interface. On the chart, “Solid” signifies the area of the sample that had not melted, while “Liquid” signifies the area of the sample that had been liquid during the experiment.

Table 2 - Melting Distances at 210°C and 19.5 at% Bi (C195-T210)

Time (s)	600	1200	1800	2400	3000
Melted Distance (mm)	1.09	1.02	1.52	2.08	1.79
	0.97	1.53	2.28	2.11	2.36
	1.15	1.36	2.33	2.08	2.32
	1.24	1.64		1.65	2.52
	0.62	1.69		1.96	2.17
	1.01	1.56		2.10	
	1.21	1.55			
		1.60			
Mean (mm)	1.04	1.49	2.04	1.99	2.23
Standard Deviation (mm)	0.209	0.214	0.454	0.179	0.275
2xStandard Error (mm)	0.158	0.151	0.343	0.207	0.208

Table 3 - Melting Distances at 210°C and 42.9 at% Bi (C429-T210)

Time (s)	600	1200	1800	2400	3000
Melted Distance (mm)	1.34	2.15			2.81
	1.18	1.98			3.20
	1.31	2.11			3.48
	1.43	2.15			3.49
	1.53				3.40
Mean (mm)	1.36	2.10			3.28
Standard Deviation (mm)	0.134	0.080			0.287
2xStandard Error (mm)	0.120	0.072			0.257

Table 4 - Melting Distances at 175°C and 42.9 at% Bi (C429-T175)

Time (s)	600	1200	1800	2400	3000
Melted Distance (mm)	0.45	0.53	0.73	0.78	0.79
	0.27	0.48	0.54	0.67	0.86
	0.36	0.50	0.66	0.70	0.89
	0.28	0.52	0.71	0.72	0.87
Mean (mm)	0.34	0.50	0.66	0.72	0.85
Standard Deviation (mm)	0.083	0.022	0.087	0.048	0.044
2xStandard Error (mm)	0.083	0.022	0.086	0.048	0.044

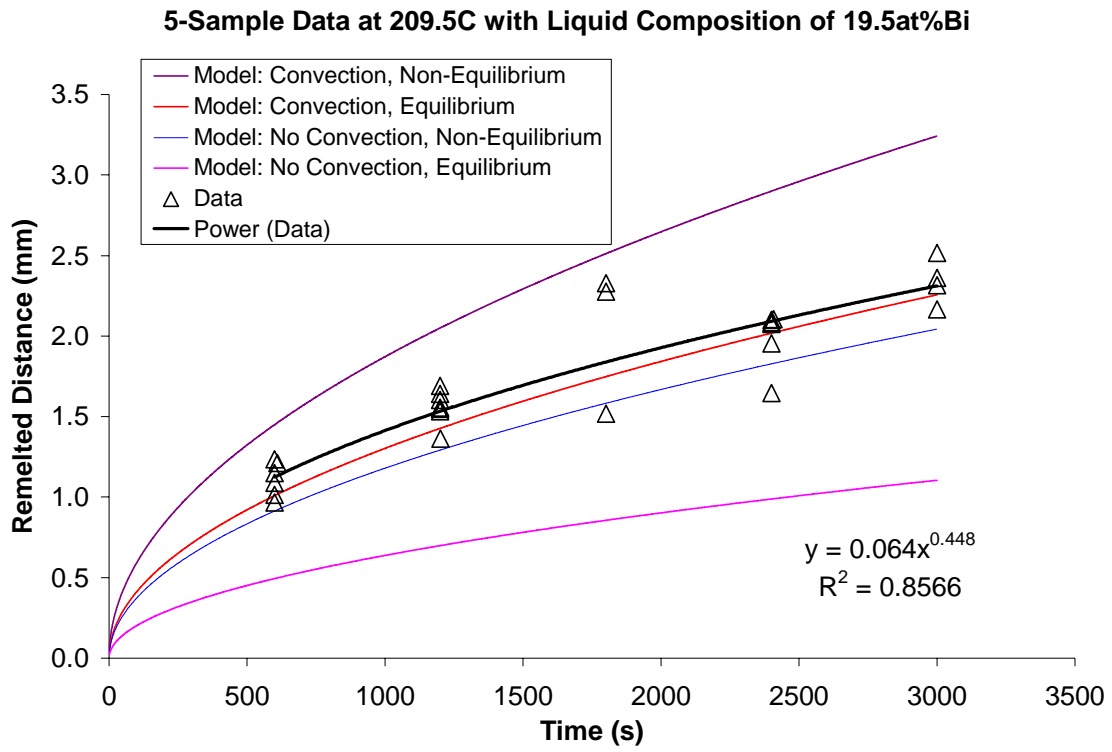


Figure 58 C195-T210 data and trend-line.

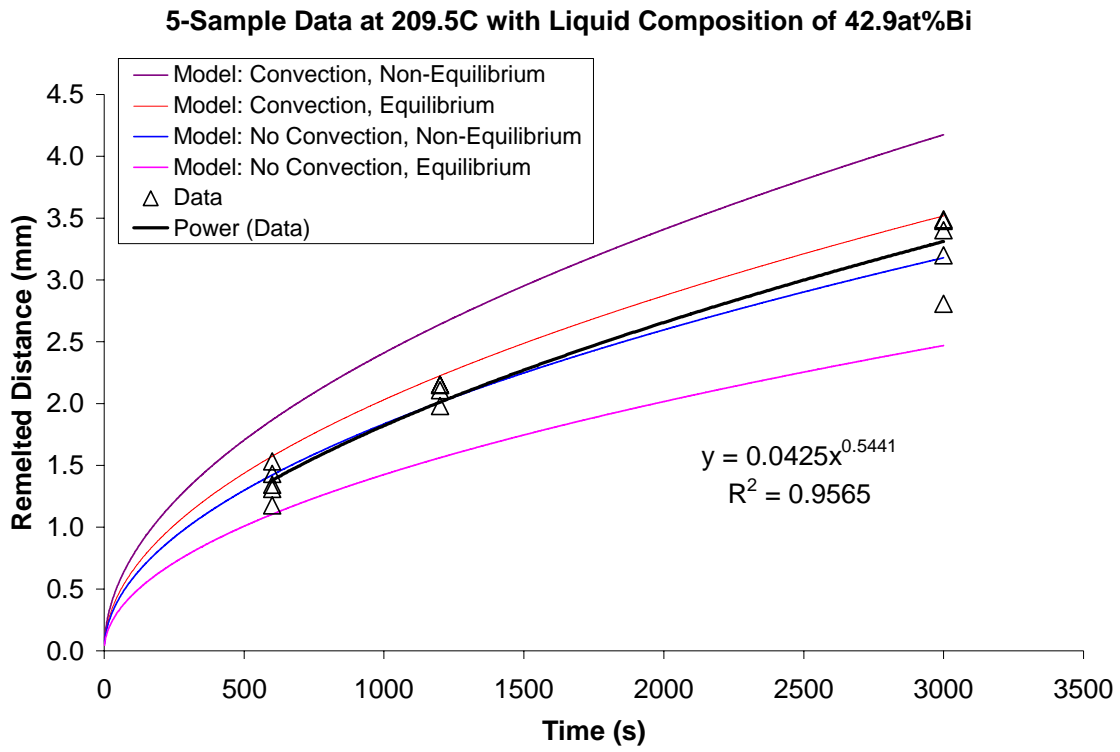


Figure 59 C429-T210 data and trend-line.

5-Sample Data at 175.0C with Liquid Composition of 42.9at%Bi

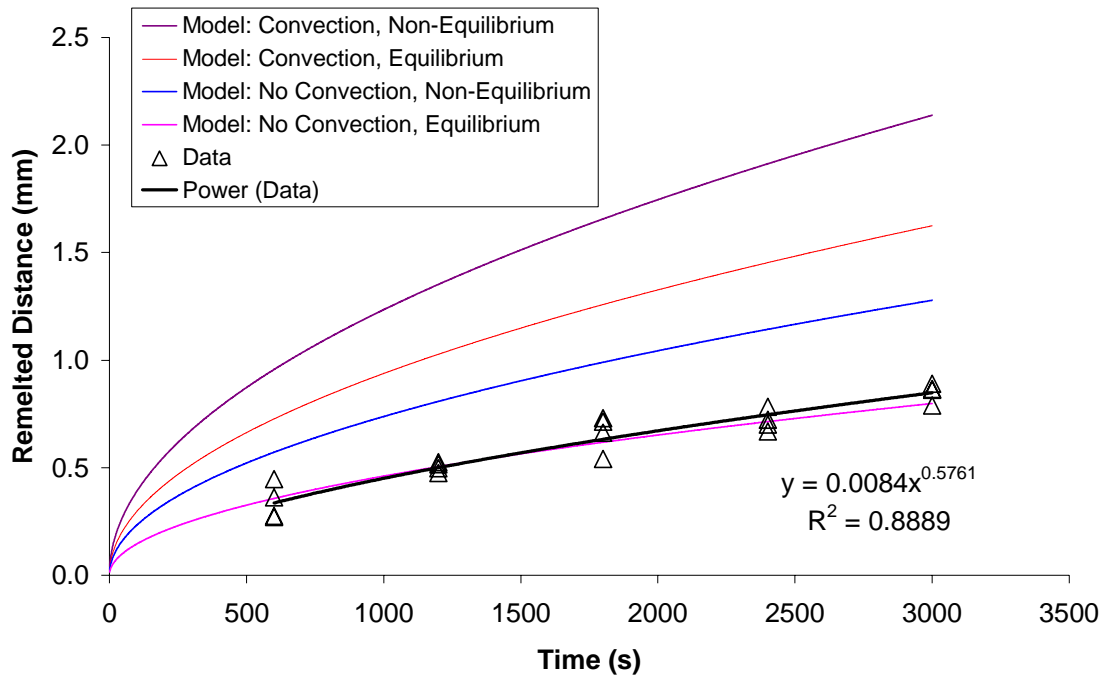


Figure 60 C429-T175 data and trend-line.

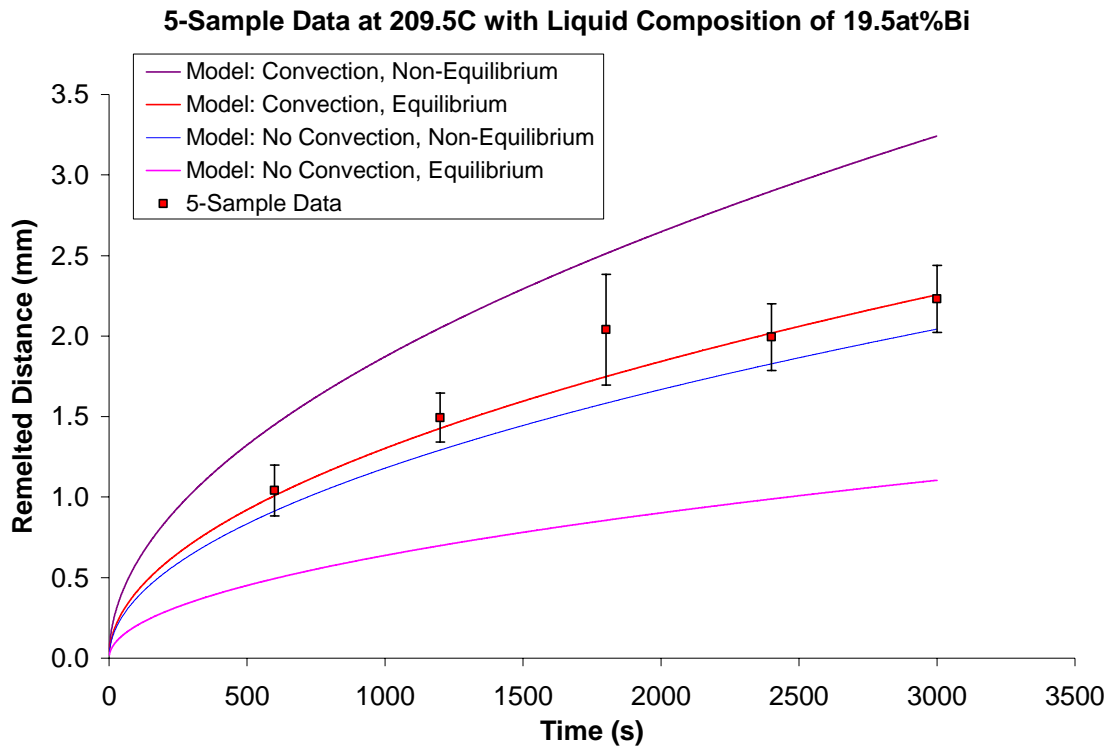


Figure 61 C195-T210 mean values and error bars.

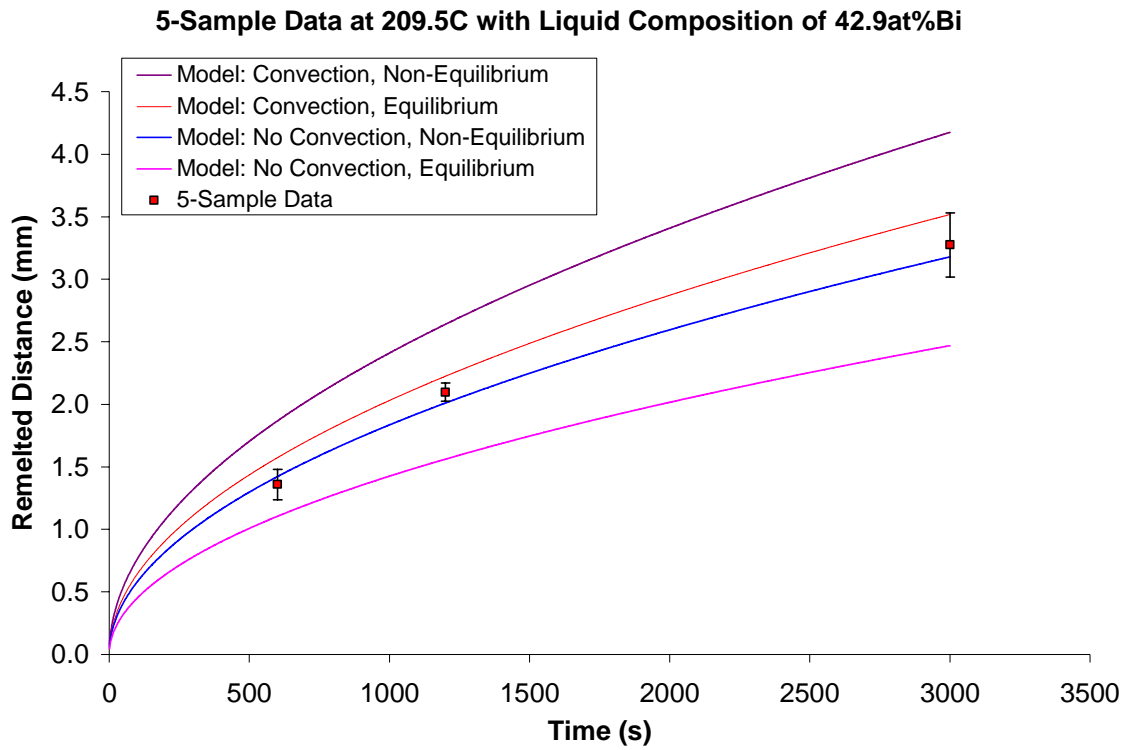


Figure 62 C429-T210 mean values and error bars.

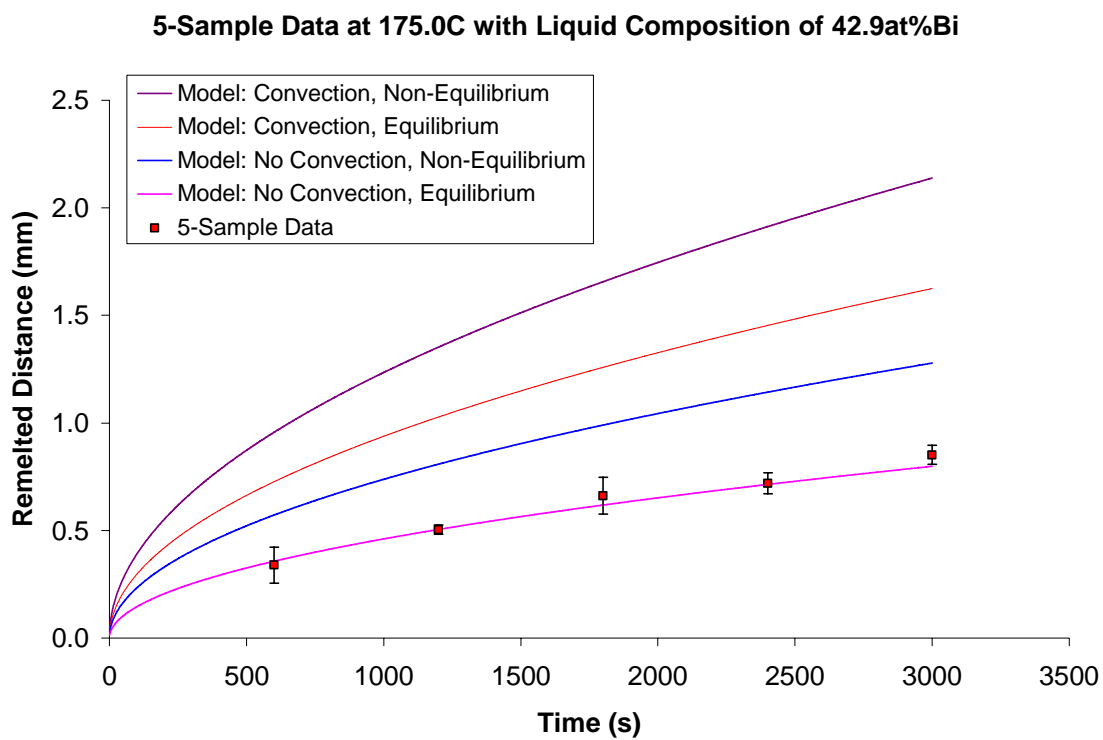


Figure 63 C429-T175 mean values and error bars.

Table 5 - Empirical Kinetic Values for Melting in the Sn-Bi System

Data	T (K)	C _{bulk} (at%)	C _L (at%)	ΔC (at%)	A (mm/s ^B)	B	Normal A (mm/s ^{1/2})	Error in A (± %)
Exp.	483	0.195	0.124	0.071	0.0562	0.467	0.0429 ± 0.0054	12.5%
Exp.	483	0.429	0.124	0.305	0.0425	0.544	0.0609 ± 0.0039	6.4%
Exp.	448	0.429	0.271	0.158	0.0084	0.576	0.0148 ± 0.0016	10.6%
Calc.	483	0.282	0.124	0.158			0.0490	

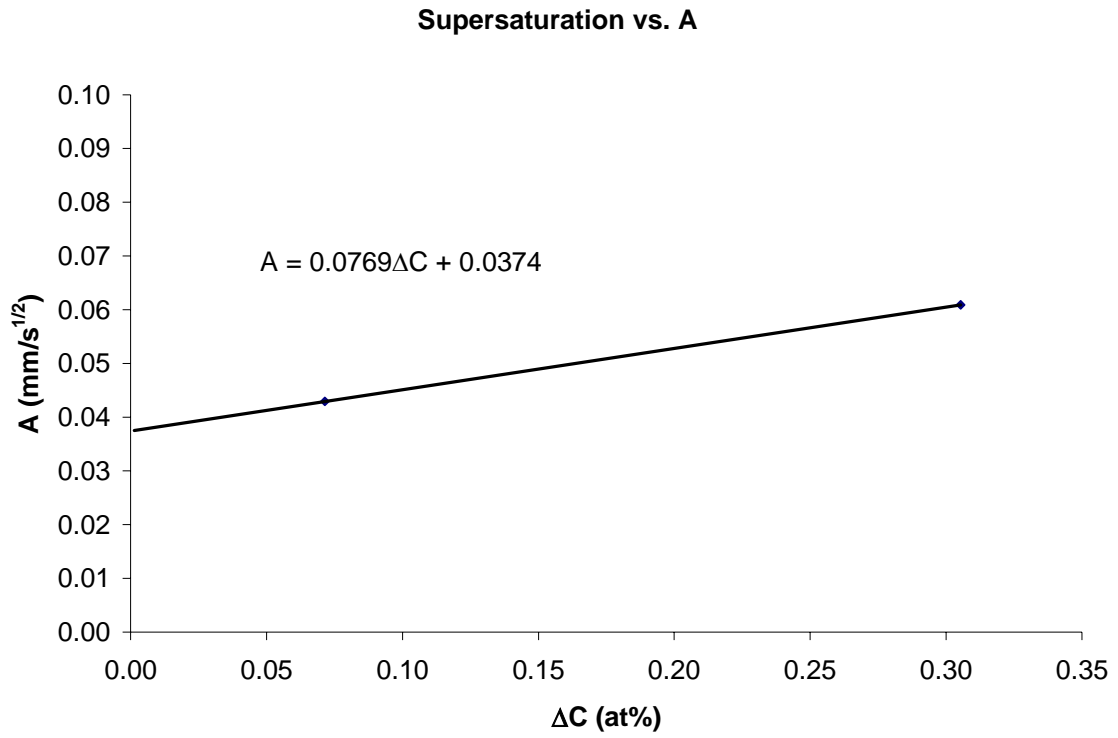


Figure 64 Linear trend-line for Supersaturation vs. A.

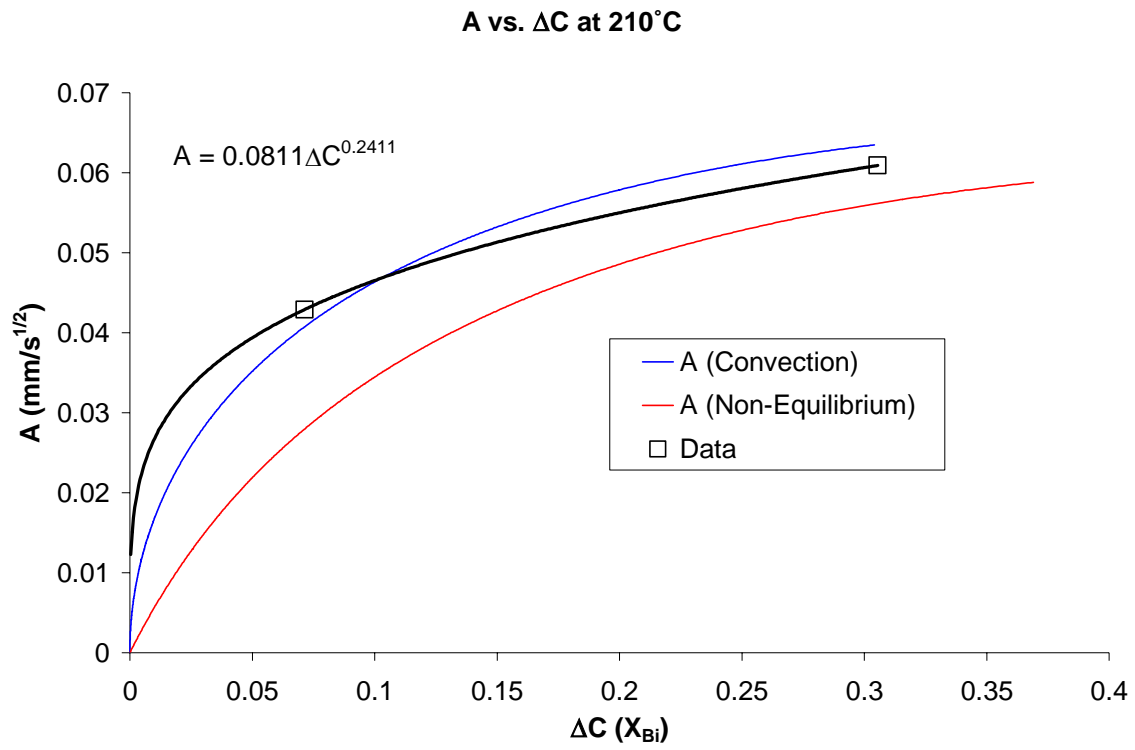


Figure 65 Non-linear trend-line for supersaturation vs. A.

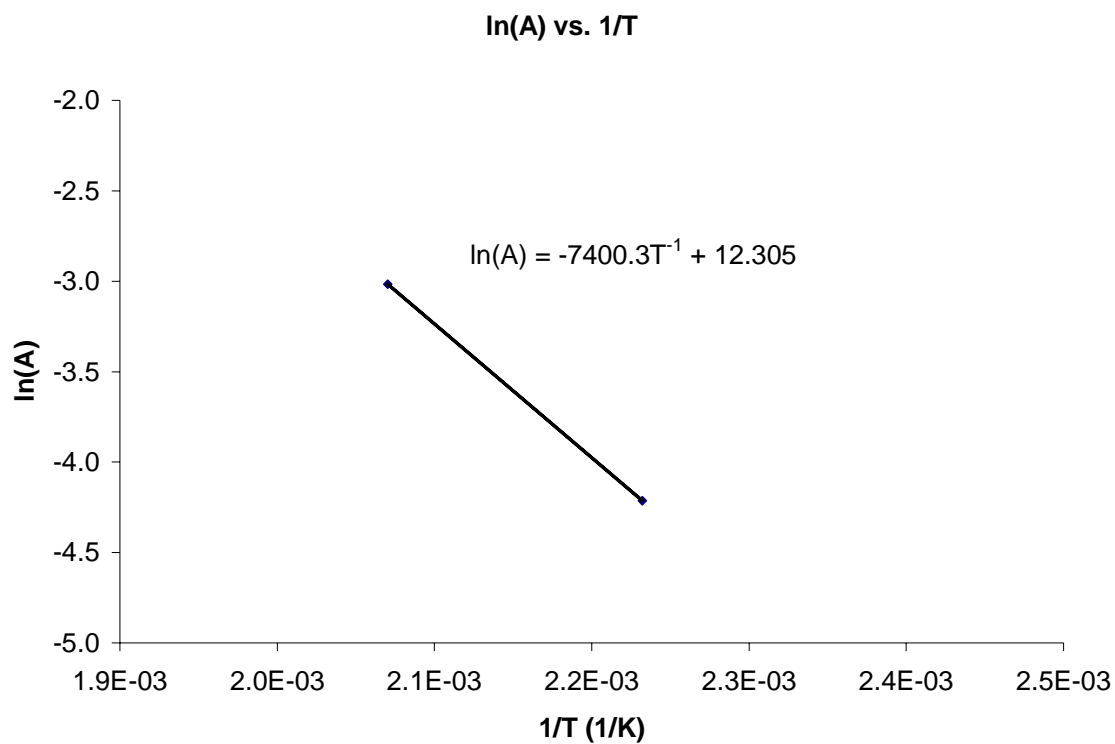


Figure 66 Logarithmic plot of A against the reciprocal of absolute temperature for the determination of activation energy.

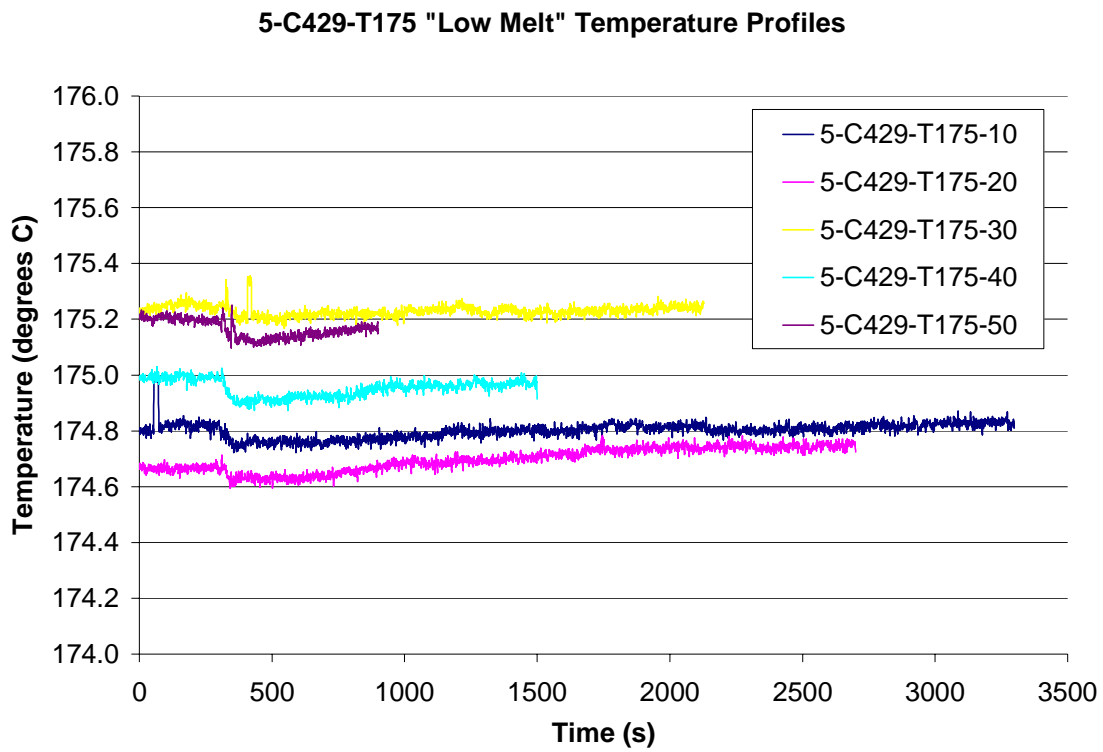


Figure 67 "Low Melt" temperature profiles during experiments displaying the temperature near the openings of the capillaries.

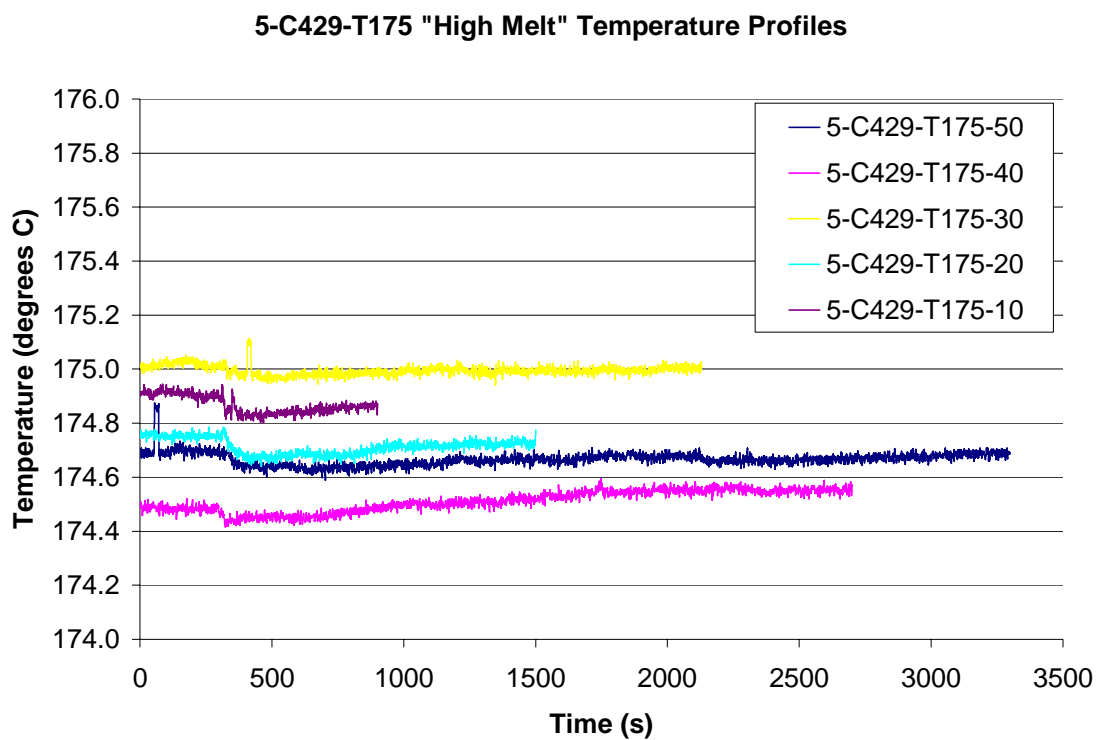


Figure 68 "High Melt" temperature profiles during experiments displaying the temperature 1cm above the openings of the capillaries.

CHAPTER 5 DISCUSSION

Micrographs and SEM Analysis

In almost all of the samples analyzed, the interface at the moment of quenching was linear. Planer phase transformation interface imply that there is little resistance to the formation of the product phase, i.e. a small amount of driving force, ΔGM is needed to push the phase interface forward. This makes sense in the case of melting. The atoms that are crossing the interface from solid to liquid can easily be incorporated into the liquid, as opposed to solidification where atoms may not as easily find an energetically favorable spot to attach to the solid. This is why supercooling a common phenomenon, while superheating is difficult to produce even in a laboratory setting.

Diffusion Control

One of the purposes of confining the melting to a capillary is the suppression of convection. By observing the melting behavior in the capillaries we can gain some insight into the nature of the convection within the tube.

Invoking the following analysis of Huppert and Sparks [5] as well as Woods [4], we can argue that convection currents crossing the entrance to the capillary are suppressed; that is no convection currents flow into or out of the capillary. The melt density follows the following relationship:

$$\rho = \rho_0 - \alpha T + \beta C \quad (D-1)$$

Above, ρ is the density of the newly melted material, ρ_0 is the density of the initial liquid, α is the coefficient relating the change in temperature to the change in density, β is the coefficient relating the change in composition to the change in density, T is the difference in temperature between the newly melted material and the initial liquid, and C is the difference between the

composition of the newly melted material and the initial liquid. In most systems, α is significantly smaller than β . For the Sn-Bi system, $\alpha T/\beta C \ll 1$ because, in part because the temperature gradient across the melted material is very small. Because of the dependence of the melted material's density on its composition as well as the concentration gradient that arises in the melt (see *Diffusion* in the *Literature Review*) the convection within the crucible/capillary system can be classified in three regimes based on the value of β and the thermal stability. In our case, we assume that the system is always stable since there is a relatively small temperature gradient in the z direction. Therefore, only two cases, $\beta > 0$ or $\beta < 0$, may apply. Since $\rho_{\text{Sn}} < \rho_{\text{Bi}}$, the density increases as the concentration of solute, Bi, increases and β is positive.

The implications of a positive value for β are that the convection is split into two layers. Since the melted material has a lower concentration, it is buoyant with respect to the highly concentrated liquid underneath, and two layers with distinct identities form. Thermal convection currents may arise within either layer, but minimal mixing between the layers occurs. Heat flows freely across the interface, but mass transfer is limited to diffusion. Thermal destabilization could cause the layers to mix, however this is unlikely due to the very small temperature gradient across the region. Therefore, we can assume that the only material entering the capillary does so via diffusion and is not flown with liquid from the melt. This analysis does not, however, discount the fact that diffusion could still possibly be at work within the capillary.

In all three cases studied here, C195-T210, C429-T210, and C429-T175, the melting position fit well with a power-type equation. Each generated line had an equation for position that depended on, approximately, the square root of time. This kind of relationship is indicative of a process wherein diffusion controls the rate. This is evidence that diffusion is the dominant

mechanism of mass transport in the capillary and as the rate controlling mechanism for interface migration.

The fact that the activation energy for melting calculated here, $60,282 \text{ J}\cdot\text{mol}^{-1}$, does not agree with those associated with diffusion through the capillary raises suspicions about whether or not convection was controlling the process. The calculated activation energy for diffusion of Bi in Sn changes across the concentration profile from $18,430 \text{ J}\cdot\text{mol}^{-1}$ at the bulk composition of 42.9at%Bi to $11,152 \text{ J}\cdot\text{mol}^{-1}$ near the interface composition of 12.4at%Bi. However, there are several factors that could have caused the discrepancy between these numbers even if the process is diffusion controlled. First, the activation energy for diffusion changes as bismuth moves from the bulk across the depleted region and into the interface, and a single calculated figure for activation energy cannot reflect this situation. The effect would cause the calculated activation energy to be higher than the highest activation energy seen for diffusion. Incidentally, that is the case in this study. Secondly, convection outside the capillary could affect the calculation of the activation energy for melting. If differing amounts of convection occurred in each of the conditions investigated, then the diffusion profiles would differ between them. This may have occurred in this study. Finally, if deviations from equilibrium at the interface manifested in one set of conditions and not the other, then the activation energy calculated for the reaction will not equal that for diffusion even if the process is diffusion controlled. This may have also occurred in the present work. These effects are discussed below.

EPMA Data

The first noticeable trait in the EPMA data is the increase in average Bi concentration near the interface. In the section that was not melted, the average concentration is close to zero. However, in the interfacial region, the concentration rises to nearly 2.5at% Bi. This is close to

the equilibrium concentration for Bi in Sn. In the region that had melted during the experiment, the concentration remains close to 2.5at% except for several points at which the concentration jumps sharply to concentrations of up to 87at% Bi. These jumps indicate areas at which the electron probe took measurements from an area that entirely or partially contained the Bi-rich phase in the eutectic region. According to the data, the transition occurs over a distance of less than 20 μm . The calculations presented in this paper predict the length of this profile to be from 1-7 μm , so these numbers are in decent agreement. Unfortunately, since the exact position of the melting interface cannot be extracted from the data at the present time, the precise concentration at the interface cannot be found. During quenching, solute rejection with planar solidification will occur for a short amount of time before the solute build-up becomes too large and the cooling rate too rapid for planar, single-phase solidification to occur. After this occurs, dendritic two-phase solidification prevails. The interface between planar and dendritic solidification is clear, however, the planar solidification region obscures the true melting interface (although the size of this region may be able to be seen in several of the optical photographs).

However, the fact that a measurable diffusive concentration profile exists at all is evidence that diffusion is occurring at a comparable pace with the interface migration, and hence is evidence that the migration is diffusion controlled.

Deviations from Equilibrium

Although the data for C195-T210 and C429-T210 seem to fall near the *Non-Equilibrium, No Convection* model and the *Equilibrium, Convection* model, decoupling of the effects of convection and deviations from equilibrium concentrations at the interface is not possible at this point. However, the profiles obtained do provide evidence of convection or non-equilibrium or a combination of both. The data collected in this study would prove useful if studies were to be

carried out with convection eliminated, i.e. carried out in microgravity, etc. Future data could be compared to data given here to decouple the effects.

In the case of C429-T175, the effects of convection and non-equilibrium interface concentrations appear to be absent. The profile gathered from experiments seems to fit well over the *Equilibrium, No Convection* model. Since both effects are absent, we can conclude with some certainty that the interface concentrations were very close to their equilibrium value. Had there been a significant departure from equilibrium, the rate would have been faster than that predicted by the model.

The question arises of why C429-T175 obeys the *Equilibrium, No Convection* model and why C195-T210 and C429-T210 have rates much higher than that model predicts. The reason at this point is not clear. Since parameters such as temperature and composition appear to be under control (see *Error in Results* section) and the melting profiles imply the within the capillary the rate was diffusion controlled, the answer is that either equilibrium was lost at the interface, that convection raised the concentration at the capillary opening, or that a combination of both occurred. Any of these explanations make sense at this point. High rates of reaction would cause equilibrium to be lost at the interface because the atoms do not have enough time to reach their lowest energy states before the reaction occurs. The loss of equilibrium thus causes even more driving force to be generated and increase the rate even further. It is possible that at 210°C and at the compositions investigated, this rate was high enough to cause non-equilibrium melting to take place, while at 175°C, the rate was low enough for equilibrium to be maintained. Similarly, at higher temperatures, convection currents are more intense than at lower temperatures. It is possible that the temperature of 210°C induces significant convection while at

175°C, the currents only raise the composition at the tip of the capillary a negligible amount. At this point, the reason is unclear

Combined Statement for the Effects of Temperature and Supersaturation

The pre-exponential factor in (R-4) can be thought of as a combination of the effects of driving force and of a separate constant dubbed the kinetic constant, K_K . The contribution from driving force is quantified as the relationship derived from Figure 1, and K_K can be calculated as:

$$K_K = \frac{2.208 \times 10^5}{0.0811(0.158^{0.2411})} = 4.248 \times 10^6. \quad (D-2)$$

In the denominator in the middle section of the equation, a supersaturation of 15.8at% was used because that was the composition at which the pre-exponential factor in the numerator was found. The value of K_K found in Rettenmayr's work was 3.446×10^8 .

The combined expression for temperature and supersaturation effects on the average velocity of a solutally melting interface is therefore

$$A = K_K (K_C \Delta C^{0.2411}) \exp\left(-\frac{Q}{RT}\right) \quad (D-3)$$

where K_C and is the coefficient from Figure 57. Inserting values for the constants found from this analysis, we have

$$A = (3.445 \times 10^5 \Delta C^{0.2411}) \exp\left(-\frac{7,400.3}{T}\right). \quad (D-4)$$

with T in K and ΔC in mole fraction.

These numbers take into account the many complicated factors involved in the melting process that were observed during this study, i.e. the change in diffusion rates from the bulk to the interface, the possible change in the amount of convection in the crucible, and the possible change in interface concentrations at different melting velocities. More research in this system

should be done to decouple these effects in order to gain a deeper understanding of the kinetic mechanisms at work in this process.

Future Work

The evidence gathered in this study proves the concept that a melting interface will move upwards through a capillary. Furthermore, there is evidence to suggest that the small size of the capillary reduces the convection currents in the melting region. Of course, the major disadvantage is the fact that the observations are *ex-situ*. Obviously *in-situ* measurements are more desirable because *ex-situ* measurements may become corrupted between the time the phenomena occur and the time the measurements are taken. Also, profiles can be gathered with just a few, i.e. 2-4 samples instead of ~20. For future studies, *in-situ* monitoring of the interface would be recommended.

A simple way to convert the present setup into an *in-situ* setup would be to add resistance measurements across the interface. The setup in Figure 69 shows a schematic of how this can be achieved. A current can be sent from a power source through the melt, into the bottom of the capillary, through the interface, out of the top of the capillary, and back to the power source. As the melting interface moves, the materials changes from solid to liquid. These different phases have different resistivity values, and therefore the phase change will affect the global resistance of the circuit, and with precise knowledge of the material properties, the resistance signal can be converted into the interface position. This technique has been used in many studies in the past to monitor the interface position during solidification and melting of metals and alloys, e.g. during the microgravity experiments for MEPHISTO [34]. It can be shown that for a sample with a fixed cross-section area A_{sample} , the change in the resistance of a sample ΔR can be related to the displacement of the interface Δz as [35].

$$\Delta z = \frac{A_{sample}}{[\rho_S(T_S) - \rho_L(T_L)]} \Delta R. \quad (D-5)$$

In (D-5), ρ is resistivity, and is expressed as a function of temperature, not multiplied with temperature. Of course, when using this technique, the current running through the sample may affect its behavior. Resistive heating, Peltier heating/cooling, electro-transport of solute, and thermal noise voltage must be considered. Information on these topics for the Sn/Sn-Bi system can be found on the topics of resistivity [36], the Peltier effect [37], electro-transport [38, 39], and thermal noise voltage [35]. Although there are other issues to be dealt with, this technique shows promise as a possible technique for further study of interface kinetics.

Another possibility for *in-situ* measurements would be the use of a transparent material for the ingot/alloy material. The present system could be modified such that the interface could be monitored optically to track the interface migration rate. The succinonitrile-water system would be a candidate for these kinds of experiments. This material has been used as a binary alloy analogue for solidification experiments in the past [40]. This *in-situ* approach has the advantage that the only disturbance at the interface would be light rays which probably have little to no effect on the kinetics. Also, for the succinonitrile-water system, the melting experiments could be carried out at lower and more easily managed temperatures.

These approaches would be more effective than the present system and would facilitate a better understanding of the kinetics of melting.

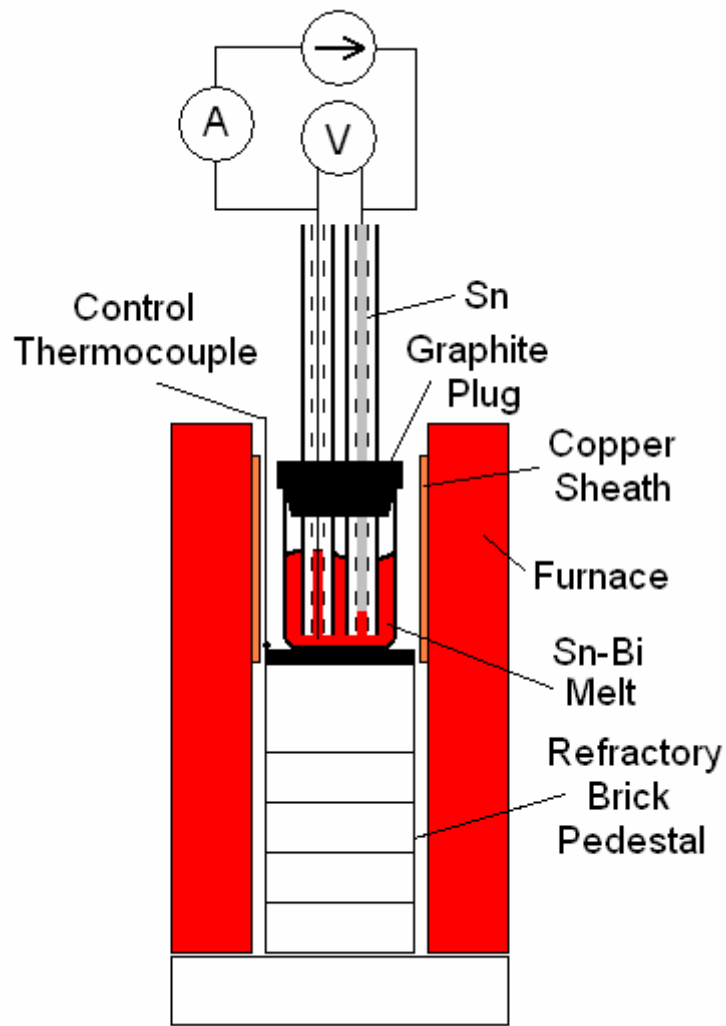


Figure 69 Schematic of an experimental setup that uses resistance signals to monitor the location of the melting interface. The setup resembles the one used in this study (Figure 31) with the exception that a current is sent through the sample. The change in resistance as the interface moves can be used to monitor the location and velocity of the interface.

CHAPTER 6 CONCLUSIONS

An apparatus has been designed to study the nature of solutal melting of metals. The setup provides an easy way to study the kinetics of melting with good accuracy. The setup is advantageous over previously published methods due to its simplicity, excellent stability of experimental conditions such as temperature and composition, and suppression of convection within the capillaries. The disadvantages are the fact that the approach is *ex-situ* and the extra time needed to run and polish many samples. However, it may be possible that a modified version of the apparatus can be used for *in-situ* monitoring of the samples in future experiments.

For the conditions studied, the melting position and velocity appeared to have a dependence on nearly the square root of time. This is that solute driven melting may be a diffusion controlled process. These results echo those of others who have studied this process. The activation energy, Q , calculated in this study was larger than those calculated for diffusion in the system. However, it was shown that factors such as convection outside the capillary, loss of equilibrium at the melting interface, and the gradient of the diffusion constant within the capillary may have affected the value of Q even if the process is diffusion controlled.

Although the data gathered here is not precise enough to estimate the values of the interface concentrations during melting, they can offer some qualitative results. For none of the conditions observed in this study was there evidence of a significant departure from equilibrium. The interface migration profiles found in this study, however, may prove to be useful if they are to be compared to future results that can decouple the effects of convection and loss of equilibrium at the interface.

The dependence of the parameter A on driving force (supersaturation) and temperature was quantified. The resulting equation was

$$A = (3.445 \times 10^5 \Delta C^{0.2411}) \exp\left(-\frac{7,400.3}{T}\right).$$

where ΔC is in mole fraction, T is in K, and A is in $\text{mm}\cdot\text{s}^{-1/2}$. However, due to lack of precise data for interface concentrations during melting, further kinetic analysis for the decoupled effects of K_M and K_T could not be calculated. Further investigation could yield more precise determinations of the mechanisms of the melting process.

REFERENCES

- [1] A. Hellawell, S. Liu, S. Z. Lu, JOM **49**, 18 (1997).
- [2] J. P. Gu, C. Beckermann, A. F. Giamei, Metall. Mater. Trans. A **28A**, 1533 (1997).
- [3] E. E. Emley, Int. Metall. Rev. **21**, 75 (1976).
- [4] A. W. Woods, J. Fluid Mech. **239**, 429 (1992).
- [5] H. E. Huppert, R. S. Sparks, J. Fluid Mech. **188**, 107 (1988).
- [6] M. Hillert, M. Rettenmayr, Acta Mater. **51**, 2803 (2003).
- [7] M. Hillert, J. Årgen, Scripta Mater. **46**, 455 (2002).
- [8] M. Rettenmayr, Scripta Mater. **48**, 315-319 (2003).
- [9] B. Dutta, M. Rettenmayr, Metall. Mater. Trans. A **31A**, 2713 (2000).
- [10] X. Wan, Q. Han, J. D. Hunt, Metall. Mater. Trans. A **29A**, 751 (1998).
- [11] J. F. Van Der Veen, H. Reichert, MRS Bulletin 958 (Dec., 2004).
- [12] J. M. Howe, H. Saka, MRS Bulletin, 951 (Dec., 2004).
- [13] J. J. Hoyt, M. Asta, T. Haxhimali, A. Karma, R. E. Napolitano, R. Triverdi, B. B. Laird, J. R. Morris, MRS Bulletin, 935 (Dec., 2004).
- [14] K. F. Kelton, A. L. Greer, D. M. Herlach, D. Holland-Moritz, MRS Bulletin, 940 (Dec., 2004).
- [15] S. K. Kang, Metall. Trans. B **12B**, 620 (1981).
- [16] C. H. Buell, F. O. Shuck, Metall. Trans. **(1)**, 1875 (1970).
- [17] J. D. Verhoeven, E. D. Gibson, J. Cryst. Growth **11**, 39 (1971).
- [18] D. A. Porter, K. E. Easterling, *Phase Transformations in Metals and Alloys*, Chapman & Hall, New York (1992).
- [19] M. Rettenmayr, O. Warkentin, H. E. Exner, Z. Metallkd. **88**, 617 (1997).
- [20] M. Rettenmayr, O. Warkentin, M. Rappaz, H. E. Exner, Acta Mater. **49**, 2499 (2001).
- [21] M. J. Aziz, Materials Science and Engineering **98**, 369 (1988).

- [22] M. Hillert, *Acta Mater.* **47(18)**, 4481 (1999).
- [23] M. C. Flemings, *Solidification Processing*; McGraw-Hill, New York (1974).
- [24] W. C. Johnson, *Metall. Mater. Trans. A* **29A**, 2021 (1998).
- [25] H. Okamoto; ASM Handbooks Online, <http://products.asminternational.org/hbk/index.jsp> (May, 2006).
- [26] B. J. Lee, C. S. Oh, J. H. Shim, *J. Electronic Materials* **25(6)**, 983 (1996).
- [27] H. Ohtani, K. Ishida, *J. Electronic Materials* **23(8)**, 747 (1994).
- [28] N. A. Asryan, A. Mikula, *Inorganic Materials* **40(4)**, 386 (2004).
- [29] O. Kubaschewski, P. Brizgys, O. Huchler, R. Jauch, K. Reinartz, *Z. Electrochem.* **54** 275 (1950).
- [30] P. G. Harrison, *Chemistry of Tin*, Blackie, Glasgow and London, Chapman and Hall, New York, (1989).
- [31] S.C. Carapella, Jr., ASARCO Inc. ASM Handbooks Online, <http://products.asminternational.org/hbk/index.jsp> (May, 2006).
- [32] S. Sharafat and N. Ghoniem, *Summary of Thermo-Physical Properties of Sn, And Compounds of Sn-H, Sn-O, Sn-C, Sn-Li, and Sn-Si And Comparison of Properties of Sn, Sn-Li, Li, and Pb-Li: UCLA-UCMEP-00-31 Report*, APEX, Los Angeles (2000).
- [33] DuPont® Teflon® Technical information, http://www2.dupont.com/Teflon_Industrial/en_US/tech_info/techlit.html (July, 2006).
- [34] M. Bruncko, I. Anzel, A. Krizman, *Materials Characterization* **51**, 185 (2003).
- [35] C. Salvi, J. P. Garandet, *Review of Scientific Instruments* **72(1)**, 255 (2001).
- [36] J. D. Verhoeven, F. Y. Lieu, *Acta Metall.* (**13**), 927 (1965).
- [37] Remi Tougas, *Memoires Scientifiques Rev. Metallurg.* **62(2)**, 142 (1965).
- [38] J. C. Warner, J. D. Verhoeven, *Metall. Trans.* **4** 1255 (1973).
- [39] L. N. Brush, S. R. Coriell, and G. B. McFadden, *J. Cryst. Growth* **102**, 725 (1990).
- [40] W. Huang, X. Geng, Xingguo, Y. Zhou, *J. Cryst. Growth* **134(1-2)**, 105-15 (1993).

BIOGRAPHICAL SKETCH

David Charles Yasensky was born on December 8, 1981, in Dunedin, FL. He graduated from Countryside High School in Clearwater in 2000. He then attended the University of Florida and earned a B.S. in materials science and engineering with a specialty in electronic materials and with a minor in physics in 2004. In June of 2004 he was accepted to the University of Florida Graduate School's Department of Materials Science and Engineering. He pursued a Master of Science while working in Dr. Reza Abbaschian's metallurgy group. He successfully defended his master's thesis on June 19, 2006.